

Infrared Spectroscopic Measurement of Titanium Dioxide Nanoparticle Shallow Trap State Energies

Steven P. Burrows

Thesis submitted to the faculty of the Virginia Polytechnic Institute and State University in partial fulfillment of the requirements for the degree of

MASTER OF SCIENCE

in

Chemistry

John R. Morris, Chair

Karen J. Brewer

Gary L. Long

February 10, 2010

Blacksburg, Virginia

Keywords: nanoparticles, semiconductor, titanium dioxide, conduction band electrons, catalysis, infrared spectroscopy, shallow trap state

Infrared Spectroscopic Measurement of Titanium Dioxide Nanoparticle Shallow Trap State Energies

Steven P. Burrows

ABSTRACT

Within the ‘forbidden’ range of electron energies between the valence and conduction bands of titanium dioxide, crystal lattice irregularities lead to the formation of electron trapping sites. These sites are known as shallow trap states, where ‘shallow’ refers to the close energy proximity of those features to the bottom of the semiconductor conduction band. For wide bandgap semiconductors like titanium dioxide, shallow electron traps are the principle route for thermal excitation of electrons into the conduction band.

The studies described here employ a novel infrared spectroscopic approach to determine the energy of shallow electron traps in titanium dioxide nanoparticles. Mobile electrons within the conduction band of semiconductors are known to absorb infrared radiation. As those electrons absorb the infrared photons, transitions within the continuum of the conduction band produce a broad spectral signal across the entire mid-infrared range. A Mathematical expression based upon Fermi – Dirac statistics was derived to correlate the temperature of the particles to the population of charge carriers, as measured through the infrared absorbance. The primary variable of interest in the Fermi – Dirac expression is the energy difference between the shallow trap states and the conduction band. Fitting data sets consisting of titanium dioxide nanoparticle temperatures and their associated infrared spectra, over a defined frequency range, to the Fermi – Dirac expression is used to determine the shallow electron trap state energy.

ACKNOWLEDGEMENTS

I would like to thank my advisor, Dr. John R. Morris for the opportunity to participate in this work, within his research group. I hope that we can continue this work as part of my pursuit of a Ph. D. at Virginia Tech.

There are many persons within the Chemistry faculty that have assisted, advised, and encouraged me over the years, both during my work on this degree and in the years preceding my start as a graduate student. I would like to thank Professor Brian Tissue for allowing me the use of his laser vaporization apparatus and the training for its correct operation. I also would like to extend thanks to Professor Gary L. Long and Professor Karen Brewer for agreeing to be part of my degree committee.

I would like to thank Ms. Kathy Lowe at the Morphology Lab of the Virginia – Maryland Regional College of Veterinary Medicine for her enormous help with obtaining transmission electron microscopy images of my nanoparticle preparations. Similar recognition is in order for Mr. John McIntosh of the Institute for Critical Technology and Applied Science for his assistance with high resolution transmission electron microscopy and electron diffraction characterization. I would also like to thank Dr. Carla Slebodnick of the Virginia Tech Crystallography Lab for her help with obtaining powder x-ray diffraction patterns of my nanoparticle preparations.

I would like to also thank past and present members of the Morris Group for many useful discussions and advice that has helped me navigate some of the more subtle and undocumented intricacies of graduate school. Particularly, I would like to thank Dr. Dimitar Panayotov (a.k.a. Mitko) for much patience and instruction in nanoparticle catalysis, and for the use of his apparatus, materials, and data.

Finally, I would like to thank my wife, Becky, for her unwavering support and encouragement, which have continued since the very beginning of the crazy idea that I should attempt to go through graduate school as a ‘non-traditional’ (i.e. old) student.

TABLE OF CONTENTS

<u>Chapter 1: Titanium Dioxide Nanoparticles and Electrons in the Solid State</u>	1
1.1 Introduction.....	1
1.2 Electrons in the Crystalline Solid State.....	3
1.2.1 Probability Distributions for Particle Energies	3
1.2.2 Classical Free Electron Models	10
1.2.3 Quantized Free Electron Model.....	14
1.2.4 The Band Theory Model.....	17
1.2.5 Band Structure Classification of Solid Phase Matter	24
1.3 Titanium Dioxide.....	28
1.3.1 General Properties	28
1.3.2 Semiconductor Doping and Trap States	33
1.3.3 The Titanium Dioxide Crystal Surface.....	37
1.3.4 Titanium Dioxide Nanoparticles and Shallow Electron Trap States.....	40
1.4 Titanium Dioxide Nanoparticle Preparation.....	41
1.4.1 Liquid Preparation Techniques	41
1.4.2 Vapor Pyrolysis	45
1.4.3 Laser Techniques.....	47
1.5 Infrared Spectroscopy of Electrons.....	50
1.5.1 Evidence for the Infrared Detection of Conduction Band Electrons.....	50
1.5.2 Characteristics of the TiO ₂ IR Baseline.....	52
1.5.3 Electron Density Measurement from Infrared Absorption	57
<u>Chapter 2: Nanoparticle Preparation, Characterization, and Spectroscopy</u>	62
2.1 Introduction.....	62
2.2 Nanoparticle Preparation by Laser Vaporization	62
2.2.1 Description of Apparatus	62
2.2.2 Nanoparticle Synthesis.....	66
2.3 Transmission Electron Microscopy.....	68
2.3.1 Image Resolution.....	68
2.3.2 Electron Microscope Operation Modes	70
2.3.3 Nanoparticle Preparation for Electron Microscopy	72
2.4 X-ray Diffraction.....	73
2.4.1 The Bragg Condition	73
2.4.2 Production of X-rays.....	74
2.4.3 Powder Diffraction	75
2.4.4 Sample Preparation and Diffraction Pattern Collection.....	76
2.5 Infrared Observation of Electron Transitions	77
2.5.1 Fourier Transform IR Spectroscopy	77

2.5.2 The Vacuum FTIR Cell	81
2.5.3 Sample Preparation and Conditioning	85
2.5.4 Temperature Ramp Infrared Spectra Collection.....	88
<u>Chapter 3: Data Analysis</u>	90
3.1 Electron Microscopy Particle Diameter Measurements	90
3.2 Powder X-ray Diffraction	94
3.3 FTIR Data Processing and Shallow Trap Energy Calculation	98
<u>Chapter 4: Discussion of Results and Conclusions</u>	103
4.1 Review of Research Objectives	103
4.2 Nanoparticle Sizes and Size Distributions.....	103
4.3 Shallow Trap State Energy Measurements	105
4.4 Estimation of Electron Shallow Traps Population.....	107
4.5 FTIR Surface Chemistry Observation and Electron Monitoring.....	110
4.6 Future Work.....	111
Appendix A: Density of States Derivation.....	114
Appendix B: Fermi-Dirac Distribution Derivation.....	119
Appendix C: FORTRAN Program WaveShave.f	122
Appendix D: FORTRAN Program Trapint2.f.....	124
Appendix E: Nanoparticle Size Measurement Data Summary	127
Appendix F: SPB018 Transmission Electron Micrograph	128
Appendix G: SPB020 Transmission Electron Micrograph	129
Appendix H: SPB018 High Resolution Transmission Electron Micrograph.....	130
Appendix I: Conduction Band Electron Population Calculation.....	131
References.....	133

LIST OF FIGURES

Figure 1: Semiconductor band structure and trap states within a nanoparticle.	3
Figure 2: The Maxwell distribution of nitrogen at T = 298K and T = 1298K.	9
Figure 3: The Thomson cathode ray deflection experiment.	11
Figure 4: Filling of electron states at the Fermi energy (E_F).	15
Figure 5: A hypothetical one-dimensional lattice.	19
Figure 6: The Kronig – Penny model.	20
Figure 7: Alternating Kronig – Penny model forbidden and allowed electron energy states.	22
Figure 8: Electron band structure for the Kronig – Penny model for a value of P = 2.	23
Figure 9: Classification of solid-phase materials from band structure.	25
Figure 10: Semiconductor band structure for the electron energy as a function of the \vec{k} electron momentum vector.	26
Figure 11: Direct (a) and indirect (b) semiconductor excitations.	27
Figure 12: Unit cell structures for rutile and anatase polymorphs of titanium dioxide.	30
Figure 13: Phosphorus n-doping of a germanium semiconductor.	33
Figure 14: Boron p-doping of a germanium semiconductor.	34
Figure 15: Titanium dioxide surface trapping of electrons.	35
Figure 16: Surface irregularities on a crystal lattice.	38
Figure 17: Aspects of the rutile TiO ₂ surface.	39
Figure 18: Titanium dioxide tube furnace pyrolysis reactor.	46
Figure 19: Flame pyrolysis nanoparticle generation.	46
Figure 20: A typical setup for synthesis of nanoparticles with laser heating.	49

Figure 21: Vibrational wave propagation in crystal lattices.....	52
Figure 22: Phonon coupling to free carrier absorbance in titanium dioxide.....	53
Figure 23: Superposition of interfacial WO ₃ infrared spectrum (a) with TiO ₂ sample spectrum (b) to produce composite infrared spectrum (c).	56
Figure 24: Development of conduction band electron density expression.	58
Figure 25: Schematic of laser evaporation chamber used for nanoparticle synthesis (end view).	63
Figure 26: Vaporization chamber laser optics (top view).	64
Figure 27: Details of hemispherical collector dome placement.	66
Figure 28: Electron diffraction in a transmission electron microscope.	71
Figure 29: Diagram for electron optics of a transmission electron microscope operated in (a) magnification, and (b) electron diffraction modes.	72
Figure 30: Bragg refraction from a crystal lattice.....	74
Figure 31: Electron transitions associated with some x-ray radiation sources.....	75
Figure 32: Powder x-ray diffraction.....	76
Figure 33: Gemini x-ray diffractometer powder sample tube preparation steps.	77
Figure 34: The Michelson interferometer.	79
Figure 35: FTIR high vacuum cell.....	82
Figure 36: Vacuum cell installed onto Mattson RS-10000 FTIR spectrometer.	83
Figure 37: Tungsten mesh nanoparticle stage assembly.	84
Figure 38: Nanoparticle press mold assembly.....	87
Figure 39: Nanoparticle mean diameter as a function of laser vaporization chamber O ₂ pressure.	93
Figure 40: X-ray diffraction pattern for an empty, 0.3 mm sample capillary.	95
Figure 41: Degussa P25 titanium dioxide nanoparticle XRD pattern with Sonneveld – Visser baseline correction.	96

Figure 42: X-ray diffraction nanoparticle characterization.....	97
Figure 43: Nonlinear regression curve-fit spreadsheet for the Fermi-Dirac relationship.	100
Figure 44: Integrated area vs. temperature plots for 4 nm (circle symbols) and 30 nm (triangle symbols) TiO ₂	102
Figure 45: Transmission electron micrographs for SPB014 and SPB015 titanium dioxide nanoparticle batches.....	104
Figure 46: The shallow trap state energy difference of titanium dioxide relative to the band structure.....	107
Figure 47: Nanoparticle FTIR flow cell.....	112
Figure 48: \vec{k} vector space for an electron.....	115
Figure 49: Acceptable wave function positions in the x-y plane.....	116
Figure 50: TEM micrograph for SPB018 4.0 ± 0.6 nm titanium dioxide nanoparticles.....	128
Figure 51: TEM micrograph for SPB020 30 ± 10 nm titanium dioxide nanoparticles.	129
Figure 52: High resolution micrograph of SPB018 titanium dioxide nanoparticles.	130

LIST OF EQUATIONS

(1) Maxwell's distribution.....	5
(2) Maxwell's distribution (rearranged, with Boltzmann constant)	6
(3) Maxwell's distribution (probability distribution)	6
(4) Maxwell's distribution (probability function form)	6
(5) Mean speed.....	7
(6) Root mean speed.....	7
(7) Most probable speed	7
(8) Relative mean speed (equal mass particles).....	7
(9) Relative mean speed (unequal mass particles).....	7
(10) Reduced mass	8
(11) Particle collision frequency.....	8
(12) Collision cross section	8
(13) Mean free path.....	8
(14) Maxwell – Boltzmann distribution.....	9
(15) Electron gas total kinetic energy (classical).....	12
(16) Electron gas heat capacity (classical)	12
(17) Drude electric conductivity	12
(18) Lorenz electric conductivity.....	13
(19) Lorenz electric conductivity (within magnetic field)	13
(20) Hall coefficient (Lorenz theory derived)	13

(21) Fermi – Dirac probability.....	14
(22) Sommerfeld specific heat of a metal	15
(23) Sommerfeld magnetic susceptibility.....	16
(24) Pauli magnetic susceptibility.....	16
(25) Sommerfeld electric conductivity.....	16
(26) Time-independent Schrödinger wave equation.....	17
(27) Schrödinger potential energy function.....	18
(28) Bloch lattice electron wavefunction	18
(29) Wave vector \vec{k} definition.....	18
(30) Block lattice electron wavefunction (Euler form).....	19
(31) Kronig – Penny electron energy (thin barrier walls, dispersion)	21
(32) Kronig – Penny electron energy (thick barrier walls)	21
(33) Kronig – Penny electron wave vector – energy relation.....	21
(34) Kronig – Penny α definition.....	21
(35) Kronig – Penny electron tunneling resistance.....	21
(36) Electron kinetic energy.	25
(37) Electromagnetic absorption as a function of energy.....	26
(38) Definition of electromagnetic absorption coefficient α	26
(39) Direct transition semiconductor absorbance.	27
(40) Indirect transition semiconductor absorbance.....	28
(41) Exciton energy levels.....	31

(42) Exciton reduced mass	31
(43) Bohr radii for electrons	31
(44) Bohr radii for electron holes.....	32
(45) Exciton lowest energy transition (at Bohr radius).....	32
(46) Exciton lowest energy transition (non-degenerate Z_3)	32
(47) Semiconductor electron confinement band gap energy	32
(48) Alkoxide hydrolysis.....	43
(49) Condensation reaction (water elimination).....	43
(50) Condensation reaction (alcohol elimination)	43
(51) Free charge carrier infrared absorbance (wavelength form).....	54
(52) Free charge carrier infrared absorbance (frequency form)	54
(53) Fermi probability (reiteration of equation 21).....	57
(54) Crystal lattice density of states.....	58
(55) Electron density differential.....	58
(56) Electron density differential (substituted).....	59
(57) Fermi probability exponential approximation.....	59
(58) Electron density differential (with Fermi exponential approximation)	59
(59) Conduction band electron density (integral form).....	59
(60) Conduction band electron density (exponential form)	59
(61) Conduction band electron density (E_{STATE} substitution).....	60
(62) Beer-Lambert Law.....	60

(63) Integrated IR baseline proportionality to conduction band electron density	61
(64) Fermi – Dirac IR baseline area relation	61
(65) E_{STATE} equation	61
(66) E_{STATE} equation (rearranged)	61
(67) Optical microscopy resolution.....	68
(68) de Broglie electron wavelength.....	69
(69) Electron kinetic energy within an electric field.....	69
(70) Electron velocity within an electric field	69
(71) Bragg’s law	74
(72) Spatial domain interferogram general equation	80
(73) Frequency domain infrared spectrum (Fourier transform of spatial domain).....	80
(74) Scherrer x-ray diffraction equation.....	94
(75) Trapezoidal numerical integration approximation	99
(76) First-order derivative of Fermi-Dirac electron density expression.	109
(77) First-order derivative of Fermi-Dirac electron density expression: first term.	109
(78) First-order derivative of Fermi-Dirac electron density expression: third term.	109
(79) First-order derivative of Fermi-Dirac electron density expression: second term.....	109
(80) First-order derivative of Fermi-Dirac electron density expression: second term solution.....	109
(81) de Broglie electron wavelength.....	114
(82) Electron wave vector \vec{k} definition	114
(83) Electron wave vector momentum components	115

(84) Electron kinetic energy	115
(85) Time-independent Schrödinger wave equation.....	115
(86) Schrödinger wave function solution.....	115
(87) Electron wave vector components.....	116
(88) Heisenberg uncertainty expressions for momentum and wave vector magnitude	116
(89) Number of electron states in k radius sphere	117
(90) Number of electron states differential	117
(91) Change in electron states density	117
(92) Change in electron states density (electron spin state compensated)	117
(93) Density of states differential	117
(94) Wave vector k magnitude.....	117
(95) k Differential	117
(96) Density of states differential (substituted)	118
(97) Density of states function.....	118
(98) Density of states function (rearranged).....	118
(99) Number of distinguishable distributions.....	119
(100) Total number of distinguishable distributions.....	119
(101) Electron state transition precondition 1	119
(102) Electron state transition precondition 2	119
(103) Thermal equilibrium distribution of electrons within states	120
(104) Stirling's factorial approximation.....	120

(105) Total distinguishable distributions (Stirling approximation)	120
(106) Electron state transition precondition 1 (rearranged)	120
(107) Electron state transition precondition 2 (rearranged)	120
(108) Lagrange expression for $\ln w$ maximum.....	120
(109) Derivative of Lagrange expression first term.....	120
(110) Derivative of Lagrange expression second term	121
(111) Derivative of Lagrange expression third term.....	121
(112) Lagrange expression for $\ln w$ maximum (substituted and rearranged).....	121
(113) Lagrange expression for $\ln w$ maximum (rearranged).....	121
(114) Fermi probability (Lagrange undetermined multipliers)	121
(115) Fermi probability (Fermi energy defined).....	121

LIST OF TABLES

Table 1: Titanium dioxide single crystal and nanoparticle band gap energies.....	30
Table 2: Comparison of accelerating voltage, electron wavelength, And resolving power for a transmission electron microscope.	70
Table 3: Fermi – Dirac regression results for SPB018 (4.0 ± 0.6 nm) TiO ₂ nanoparticles.....	101
Table 4: Fermi – Dirac regression results for SPB020 (30 ± 10 nm) TiO ₂ nanoparticles.	101
Table 5: Survey of reported values for titanium dioxide shallow trap state energy gap, relative to bottom edge of conduction band.	106
Table 6: TiO ₂ nanoparticle size measurement data.....	127

Chapter 1: Titanium Dioxide Nanoparticles and Electrons in the Solid State

1.1 Introduction

The properties of nanoparticles, aggregates of material at dimensions less than 100 nm (1×10^{-7} m), have been of much recent interest. The reduction in particle size to the nanometer scale has been observed to significantly change the properties of some substances. This shift in chemistry as a function of size, challenges the idea of a material's chemical reactivity as an intensive, i.e. size independent, property.

Gold presents an example of a size-mediated shift in chemical reactivity. The chemical inertness of gold is one of the properties that contributed to its high valuation, in addition to its aesthetic appeal. For most of human history, gold has been perceived as eternal and unchanging. Although it is not completely inert, gold in bulk form does not easily enter into chemical reactions. Hammer and Nørskov described gold as the “noblest of all metals”, and explained that this low reactivity is the result of the stability of gold's electronic structure.¹ Gold atoms have filled d-orbitals and relatively high ionization potentials. When compared to the other coinage metals, silver and copper, gold's first valence electron is more difficult to remove in a chemical reaction (9.22 eV vs. 7.58 and 7.73 eV respectively).² Gold does not oxidize under ordinary environmental conditions. When this resistance to forming oxide coatings is considered with gold's relatively low electrical resistivity ($2.255 \times 10^{-8} \Omega \cdot \text{m}$ at 298 K),³ the utility of gold for protective coatings in electrical contact surface applications is obvious.

Because of its low chemical reactivity, bulk gold was regarded as a poor catalyst. Bond described bulk gold as “the least catalytically useful”.⁴ In his review of the history of gold catalyst research, Haruta observed that bulk gold was regarded as almost catalytically inactive.⁵ This behavior changes significantly when gold enters reactions in particle sizes of approximately 5 nm (5×10^{-9} m) diameter. On this size scale, gold becomes very catalytically active. Gold nanoparticles placed upon titanium dioxide supports have been observed to dissociate molecular

hydrogen at 300 K⁶ and catalyze the reduction of carbon monoxide⁷. The application of catalyst systems comprised of gold and metal oxide support nanoparticles to the detection and decomposition of chemical warfare agents (CWAs) and similar materials remains an active area of research.⁸⁻¹⁴

Although titanium dioxide nanoparticles first found use as a support for the dispersal of smaller particles of noble metals such as gold and platinum, the titanium dioxide itself also exhibits unique catalytic properties apart from the supported metal particles. The application of titania nanoparticles to catalysis is appealing due to its relatively low material cost and the numerous routes to titanium dioxide nanoparticle synthesis.

Several novel applications use titanium dioxide nanoparticles where the cost of equally effective metal catalysts would be prohibitive. With alternative approaches to supplying the world's growing energy needs, titania catalysts combined with photoactive dyes have attracted attention for use in photovoltaic cell applications.¹⁵⁻²¹ Photolysis of water for the production of hydrogen fuel is another energy application for titanium dioxide nanoparticles.²²⁻²⁷ In addition to decomposition of chemical warfare agents, titania nanocatalysis is being investigated for treatment of environmental pollutants.²⁸⁻³³ Titanium dioxide nanoparticle catalysts are already commercially produced and sold under the brand name Aeroxide[®] P-25 for industrial application by the Degussa subsidiary of Evonik Industries A.G.

Titanium dioxide nanoparticle catalysis is dependent upon the movement of electrons to and from the particle surface, where adsorption occurs. The factors affecting this transport of electrons within the nanoparticle derive from its electrical properties and the extent that titanium dioxide can use the thermal and electromagnetic energy of its surroundings to cause electric charge separation. The most easily separated electrons within titanium dioxide nanoparticles are located in structural features known as shallow trap states. These sites are primarily located at defects in the crystal lattice of the nanoparticle. Within this thesis, I will describe an experimental approach that applies infrared spectroscopy to the measurement of the energy

required to make shallow trap state electrons available for oxidation-reduction chemistry with adsorbates at the nanoparticle surface. That energy is the shallow trap state energy.

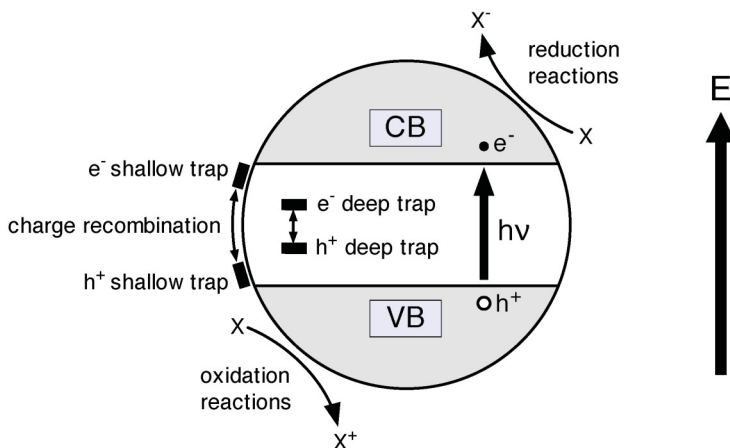


Figure 1: Semiconductor band structure and trap states within a nanoparticle. Electrons are represented by e^- and electron holes by h^+ . Adapted from Beydoun et al.³⁴

1.2 Electrons in the Crystalline Solid State

1.2.1 Probability Distributions for Particle Energies

My approach to calculating the energy of shallow trap states in crystalline titanium dioxide nanoparticles requires the use of the Fermi-Dirac probability distribution for electrons. Because early models for the movement of electrons within solid – phase matter were based on energy probability distributions derived from classical Newtonian mechanics, I will review the development of the most successful classical model, the Maxwell – Boltzmann distribution.

The development of an accurate quantitative description of the interaction of energy and matter has been a principle goal of physical science. The early efforts preceded knowledge of quantum mechanics, during the nineteenth century. Investigators directed their work at a mathematical model that could calculate the energy of every particle comprising a closed system. This effort began with an assumption that Newtonian mechanics were sufficient to derive a comprehensive model. Because of the large number (approximately 10^{20}) of particles in even a

miniscule sample of solid or liquid matter, it was logical to first examine the least dense state: gases.

Over the course of the nineteenth century, acceptance of the atomic theory of matter was far from universal. The idea that matter was comprised of irreducible particles that defined its properties is known to have existed since ancient Greece and is usually attributed to Democritus (460 – 370 B.C.).³⁵ The nature of atoms themselves remained a mystery until the early twentieth century and in the absence of more evidence many physicists were skeptical as to their very existence. As late as 1897, Ernst Mach openly declared his disbelief in the existence of atoms during a presentation before the Viennese Academy of Sciences.³⁶ Physicists used the term ‘particle’ in reference to atoms and/or molecules. This substitution was motivated by their reluctance to fully accept atomic theory and avoidance of tedious repetition of the phrase ‘atoms and/or molecules’ in settings where either might be applicable. I continue the usage of ‘particles’ in this section for the latter reason.

The starting point for consideration of the behavior of gaseous matter is the kinetic theory of gases. This model is comprised of several axioms. Included are that gases are comprised of particles whose sizes are greatly smaller than their volume of confinement. The disparity between particle size and sample size is great enough to render the sizes of the particles insignificant and their influences to those of point entities. Another aspect of kinetic theory is that confined gas ‘particles’ travel at high rates of speed and make collisions with other particles and the walls of their container. The result of these collisions is that kinetic energy exchanges between the colliding entities. If two particles collide, they leave the collision with different velocities. If a particle collides with a container wall, the result is a miniscule movement of the wall. Gas pressure is the collective result of numerous instances of particle-wall collision.

Another assumption of the kinetic theory of gases is that for a sample of gas in thermal equilibrium, the gas particles will exist with a non-uniform distribution of speeds. This statement is equivalent to saying that the particles will exist in thermal equilibrium with an unequal distribution of kinetic energies. This partitioning of kinetic energies in gases is evident

in the Earth's atmosphere, and is described in an example given by Gilbert Castellan in his text *Physical Chemistry*.³⁷ The argument is that if all atmospheric gas particles possessed the same upward component of velocity, then at ground level all particles would be limited to a maximum altitude which they could reach under the influence of gravity. This situation would lead to the Earth's atmosphere possessing a sharply defined boundary, beyond which no gas molecules could travel. In addition, the density of the atmosphere would increase with altitude as particles near the end of their upward travel would slow down and accumulate at high altitude. Neither of these two conditions are observed in the Earth's atmosphere. Atmospheric density decreases with altitude and this property is directly observable during an ascent up a mountain. Another consideration is that the atmosphere does not have a well-defined boundary, as is demonstrated by the existence of significant atmospheric drag effects upon orbiting spacecraft.^{38, 39} The conclusion is that thermally equilibrated gas particles exist with an unequal distribution of kinetic energies.

Several researchers had addressed the question of how confined gas particles distribute a fixed quantity of energy. Between 1738 and 1845, Daniel Bernoulli, John James Waterston, and John Herapath each proposed models for gas behavior that anticipated parts of the kinetic theory of gases, although their efforts were either forgotten or ignored by the scientific establishment of the nineteenth century.³⁶

The Scottish physicist James Clerk Maxwell published a theory for the distribution of kinetic energy within a sample of confined gas in 1860 and followed this paper with another in 1867 where he offered more justifications for his approach.³⁶ The derivation of the Maxwell distribution is based upon Newtonian descriptions of the component velocities of a particle in each of the Cartesian axes of space. Maxwell's equation for the distribution of number n_c of gas particles with speed between c and $c + dc$ is given by the equation:

$$dn_c = 4\pi N \left(\frac{mN_A}{2\pi RT} \right)^{3/2} c^2 \text{Exp} \left(-\frac{mc^2 N_A}{2RT} \right) dc \quad (1)$$

where N is the total number of particles, m is the particle mass, N_A is Avogadro's number (6.022×10^{23} particles \cdot mol $^{-1}$), R is the gas constant (8.313 J \cdot mol $^{-1}$ \cdot K) and T is the thermodynamic temperature of the confined gas system. Recognition that the ratio R/N_A is equivalent to Boltzmann's constant k_B (1.381×10^{-23} J \cdot K $^{-1}$) and that $E_{kinetic} = \frac{1}{2}mc^2$ allows Equation (1) to be rewritten as:

$$dn_c = 4\pi N \left(\frac{m}{2\pi k_B T} \right)^{3/2} c^2 \text{Exp} \left(-\frac{E_{kinetic}}{k_B T} \right) dc \quad (2)$$

The Maxwell distribution is frequently rearranged for convenience to the probability distribution:

$$\frac{1}{N} \frac{dn_c}{dc} = 4\pi \left(\frac{m}{2\pi k_B T} \right)^{3/2} c^2 \text{Exp} \left(-\frac{E_{kinetic}}{k_B T} \right) \quad (3)$$

The terms on the left side of the equation represent a probability that a particle of mass m will have speed c when thermally equilibrated to temperature T . This probability function has the units of sec \cdot m $^{-1}$ and is represented by the function $f(c)$:

$$f(c) = 4\pi \left(\frac{m}{2\pi k_B T} \right)^{3/2} c^2 \text{Exp} \left(-\frac{E_{kinetic}}{k_B T} \right) \quad (4)$$

The use of the term 'distribution' in the Maxwell distribution is a reference to classification of particles into categories or intervals. In this case, the intervals are particle speeds and the width of those categories is taken to be the infinitesimal increment dc . While it may be implicit that an expression for particle velocities based upon Newtonian mechanics could be used to calculate the velocity and kinetic energy for every constituent particle of a system, such comprehensive characterizations of a system are impractical. As an alternative, statistical characteristics for a gas particle system are derived from the Maxwell distribution.

The mean speed, c_{avg} , for a system can be derived from Equation (4) and is given by the expression:

$$c_{avg} = \sqrt{\frac{8RT}{\pi M}} \quad (5)$$

where M is the molar mass of the particle. Another useful statistic that can be derived from Equation (4) is the root mean square speed, c_{rms} :

$$c_{rms} = \sqrt{\frac{3RT}{M}} \quad (6)$$

The most probable speed, c^* , is derived from Equation (4) by evaluating the first derivative of $f(v)$ with respect to c , and finding the speed at which the derivative is zero (excepting the cases $c = 0$ and $c = \infty$). The resulting expression for c^* is:

$$c^* = \sqrt{\frac{2RT}{M}} \quad (7)$$

The relative mean speed, c_{rel} , is the speed at which two particles approach each other. This speed is derived from the mean speed (Equation (5)) and for two particles of equal mass it is given by:

$$c_{rel} = \sqrt{2} c_{avg} \quad (8)$$

For two particles of unequal mass the c_{rel} is given by:

$$c_{rel} = \sqrt{\frac{8k_B T}{\pi \mu}} \quad (9)$$

where k and T have their previously describe values and the term μ is the reduced mass of the two particles, given by the equation:

$$\mu = \frac{m_a m_b}{m_a + m_b} \quad (10)$$

The terms m_a and m_b are the respective masses of the two particles being described. The frequency of particle collisions, z , is given by the equation:

$$z = \frac{\sigma c_{rel} N}{V} \quad (11)$$

where N is the number of particles and V is the volume of their confinement. The term σ is the collision cross section of the particle, given by:

$$\sigma = \pi d^2 \quad (12)$$

where d is the particle diameter. All of these derivations from Equation (4) lead to an expression for the average distance traveled by a particle between collisions, the mean free path λ :

$$\lambda = \frac{c_{avg}}{z} \quad (13)$$

Mean free path descriptions will become important in the development of models for conduction of electrons in metals. An example of the Maxwell speed distribution for nitrogen gas at $T = 298$ K and $T=1298$ K, with c^* , c_{avg} , and c_{rms} identified at each temperature is given in Figure 2.

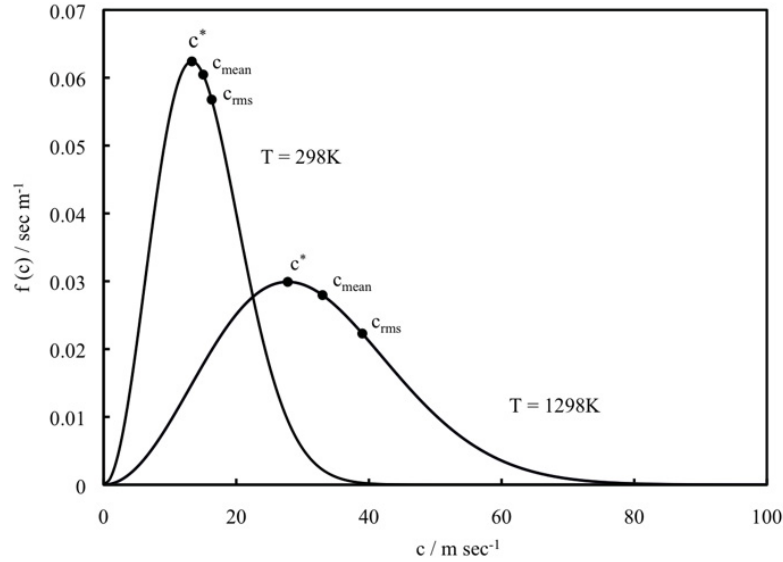


Figure 2: The Maxwell distribution for nitrogen at T = 298 K and T=1298 K.

Ludwig Boltzmann published a paper in 1868 that provided additional justifications for the Maxwell distribution and extended it to include not just kinetic energy but other forms as well (e.g. potential energy). Because of Boltzmann’s work in validating Maxwell’s previous work and his extension of the theory, the energy partition probability is referred to as the Maxwell – Boltzmann distribution and it is given by the equation:

$$f(c) = 4\pi \left(\frac{m}{2\pi k_B T} \right)^{3/2} c^2 \text{Exp} \left(-\frac{E_{kinetic} + E_{potential}}{k_B T} \right) \quad (14)$$

The terms of the Equation (14) have their previously described meanings and values. Potential energy is described as the energy of configuration for the particles.⁴⁰ An example of potential energy is given by considering the upward trajectory of a particle in a gravity field. At the start of the particle motion at ground level, all of the particle energy is kinetic. During the upward travel of the particle, the energy is kinetic and potential. At the maximum height of travel, when the particle upward motion stops and speed is equal to zero, all of the particle energy is potential.

During downward travel the particle again possesses a combination of kinetic and potential energies, and at impact upon the ground all energy is once again kinetic.

1.2.2 Classical Free Electron Models

Researchers anticipated the existence of a fundamental charge carrier for electric current for centuries. The ability of objects to accumulate static electric charges implied that something was present on their surfaces which carried the electric charge and that entity could be transferred off the charged object upon discharge. With the discovery of the electron in 1897, John Joseph Thomson established the particle nature of electric charge.⁴¹

Thomson's experiments leading to the discovery of the electron were based upon the deflection of cathode rays by electric and magnetic fields. Cathode rays are actually a stream of electrons. One means of imparting enough energy to the electrons of a sample of metal is to heat it. In the presence of a reactive gas such as oxygen, the metal is oxidized by the loss of electrons and the reacting gas is reduced through the gain of those departing electrons. In a vacuum, when the heated metal has an electric potential applied to it with respect to an anode, an electric current flows from the cathode to the anode. A schematic of the Thomson cathode ray deflection experiment is given in Figure 3. This effect is the basis for operation of thermionic vacuum tubes and cathode ray tube displays that were the basis for most modern electronic devices during the twentieth century.

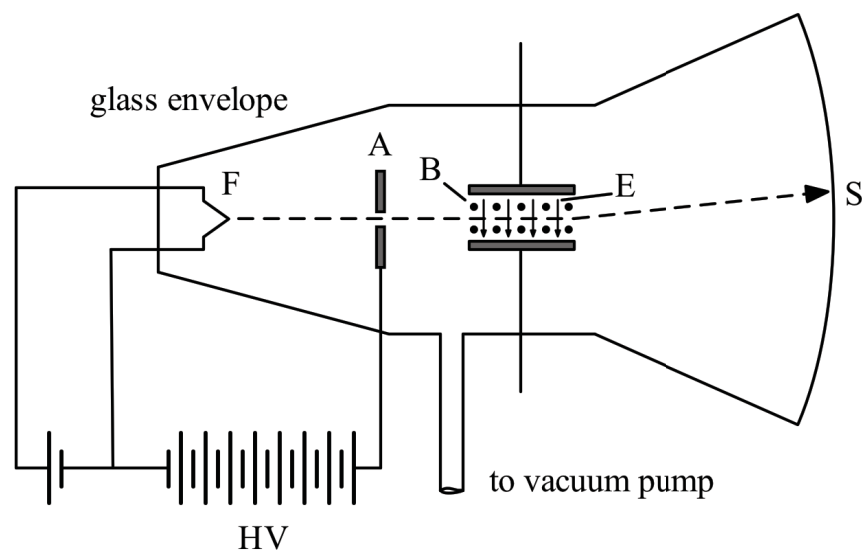


Figure 3: The Thomson cathode ray deflection experiment. The cathode is the heated filament F and the anode is A . E indicates lines of electric force and B indicates lines of magnetic force, perpendicular to the page. HV is a high voltage power supply and S is a phosphorescent screen.⁴⁰

In the course of his experiments leading to the discovery of the electron, Thomson noted that the ability to emit electrons was not particular to any specific metal provided sufficient energy was supplied. In 1900, Paul Drude, A contemporary of Thomson, proposed that electrons might be a component of the metal atoms themselves rather than being solely supplied by the circuit providing electric potential to the cathode ray experiment.

Drude proposed a model for the structure of metals at the atomic scale that accounted for some observed behaviors.⁴² The Drude model for metals was based upon several assumptions that include:

- Metals possess a population of delocalized, mobile electrons that behave like a sample of confined gas molecules.
- The population of mobile electrons is formed by the donation on one electron by each metal atom, leaving behind a stationary, positively charged atom core.
- The delocalized, mobile electrons are responsible for the metal's ability to conduct an electric current.

- The delocalized conduction electrons move with a Maxwell – Boltzmann root mean square speed (Equation (6)).

Drude’s assumption that mobile electrons in a metal behave like a gas conforming to Maxwell – Boltzmann probability distribution requires that the energies of the electrons are totally kinetic and the electron gas as a whole has a total energy E , given by:

$$E = \frac{3}{2}nk_B T \quad (15)$$

where n is the number of conduction electrons present in the bulk sample of metal. The classical mechanics derived heat capacity of the electron gas, C_{cl} would be given by the expression:

$$C_{cl} = \frac{3}{2}nk_B \quad (16)$$

One implication of Equation (16) is that metals should have a heat capacity almost double of what is actually observed. Another fallacy of Equation (16) is that the heat capacity of the conduction electron ‘gas’ is independent of temperature, where the observed trend is that the specific heat is linearly dependent upon temperature.

The Drude model results in a derived thermal electrical conductivity σ for metals given by the equation:

$$\sigma = \frac{ne^2 \lambda}{\sqrt{3m_e k_B T}} \quad (17)$$

where e is the elementary charge (1.6022×10^{-19} C), λ is the electron mean free path (Equation (13)), and m_e is the rest mass of the electron (9.1094×10^{-31} kg). Equation (17) requires that metal electrical conductivity vary inversely with $T^{1/2}$, which is contradictory to the observed T^{-1} dependency of electrical conductivity. Drude argued unsuccessfully that the mean free path λ for conduction electron-positive atom core collisions must have a $T^{-1/2}$ dependency.

In 1905 H. A. Lorentz suggested a modified form of the Drude free electron model.⁴³ Lorentz considered that the Maxwell distribution of the conduction electrons would have its symmetry disturbed by the effects of either an applied electric field or a thermal gradient. The Lorentz model led to a derived electric conductivity σ for metals of:

$$\sigma = \frac{4ne^2\lambda}{3\sqrt{2\pi m_e k_B T}} \quad (18)$$

The Lorentz conductivity leads to a result that is 0.92 of the Drude conductivity. By considering the perturbation of conduction electron scattering by an external field, the Lorentz model predicts an expression metal conductivity in a magnetic field of:

$$\sigma_B = \frac{J^2 \sigma}{J^2 + (\sigma R_H)^2 |\vec{J} \times \vec{B}|^2} \quad (19)$$

where J is the magnitude of the conduction electron path vector \vec{J} and \vec{B} is the magnetic field vector. The term R_H is the Hall coefficient, which represents the magnitude of the transverse electric field in a conductor that is subjected to a magnetic field. The Lorentz model leads to a Hall coefficient of:

$$R_H = -\frac{3\pi}{8ne} \quad (20)$$

The Drude model predicted that all electrons would have the same thermal velocity and this assumption would result in no magnetoresistive effect. The Lorentz model predicted a disturbance of Maxwell – Boltzmann distribution symmetry that would result in electrons being subjected to forces that cause their departure from straight conduction paths under the influence of a magnetic field. This prediction of magnetoresistance in metals was an improvement over the Drude model.

The inability of free electron conduction models for metals to accurately predict electrical conductivity or specific heat led to continuing efforts to improve them. One large failing of both the Drude and Lorenz models was their neglect to address the magnetic susceptibility of metals. Pauli exclusion spin pairing of electrons was unknown when Drude and Lorenz proposed their metal conductivity models. One would expect that the large population of mobile charge carriers that free electron models assume to be present would lead to strong magnetic susceptibilities in all metals. That conclusion is not consistent with the actual observed properties of metals, which vary considerably in magnetic susceptibilities.

1.2.3 Quantized Free Electron Model

Working independently in the early twentieth century, Enrico Fermi and Paul Adrien Maurice Dirac (P.A.M. Dirac) derived an expression for the probability that an electron will occupy an energy state within a substance. That probability $p(E)$ is given by the equation:

$$p(E) = \frac{1}{1 + \text{Exp}\left(\frac{E - E_F}{k_B T}\right)} \quad (21)$$

The term E is the energy of the electron. The term E_F is the Fermi energy of the material under consideration. The Fermi energy is defined as the energy of the highest occupied state for a material at absolute zero temperature ($T = 0$ K). Figure 4 shows the energy increase with the increasing number of available electron states, $n_S(E)$ for a system at $T = 0$ K. By definition, no states above the Fermi Energy E_F can be filled at $T = 0$ K.

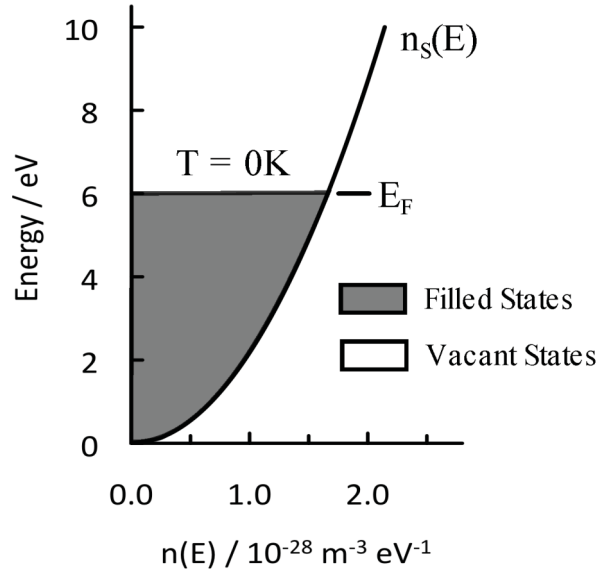


Figure 4: Filling of electron states at the Fermi energy (E_F).⁴⁰

In 1927, Arnold Sommerfeld applied the Fermi-Dirac probability function to the free electron model for metals.⁴² The Sommerfeld quantized free electron model is based on the observation that only the electrons in a metal that are energetically close to the Fermi energy have sufficient freedom to be scattered to other energy levels. Electrons occupying states at energies significantly lower than the Fermi energy are effectively immobilized due to the absence of available empty states in their vicinity. The effect of this modification on the Drude and Lorenz free electron models was to greatly reduce the number of electrons available to participate in the ‘electron gas’ that is a key component of free electron models.

With fewer electrons contributing to the bulk properties of the metal, the Sommerfeld model was able to more accurately estimate the electronic component of a metal’s specific heat:

$$C_e = \frac{n\pi^2 k_B^2}{eE_F} T \quad (22)$$

The Sommerfeld model predicted a magnetic susceptibility χ for a non-degenerate electron gas given by the equation:

$$\chi = \frac{n\mu_B^2}{3k_B} \frac{1}{T} \quad (23)$$

The term μ_B is the Bohr magnetron ($9.727 \times 10^{-24} \text{ J T}^{-1}$). The most notable feature of Equation (23) is its inverse dependence upon temperature and the absence of a magnetic field dependency. This type of behavior is not observed for metals. Wolfgang Pauli derived an expression for the total magnetic susceptibility χ_{total} that removed the temperature dependency and was successful in predicting the behavior of some alkali metals:

$$\chi_{\text{total}} = \frac{n\mu_B^2}{E_F} \quad (24)$$

Sommerfeld's model resulted in an expression for electrical conductivity given by:

$$\sigma = \frac{ne^2\lambda(E_F)}{ms(E_F)} \quad (25)$$

where $\lambda(E_F)$ is the mean free path length of electrons at the Fermi energy and $s(E_F)$ is the speed of electrons at the Fermi energy. Equation (25) has no temperature dependency, which contradicts the observed temperature dependent conductivity behavior of metals.

The Sommerfeld free electron model for the behavior of metals was able to predict the heat capacities and magnetic susceptibilities with some limited accuracy. The application of Fermi-Dirac statistics to limit the number of electrons participating in the 'electron gas' of a metal was anticipatory of the presently accepted model for solid-state electrical behavior, band theory. However, the inability of the Sommerfeld model to account for the observed temperature dependence of electrical conductivity in metals cast doubt upon whether it was an accurate depiction for electron transport processes in metals.

1.2.4 The Band Theory Model

By the late 1920's, Felix Bloch, a graduate student of Werner Heisenberg, began work on the shortcomings of the Lorentz free electron gas model as the topic of his thesis. While the Sommerfeld model for electron behavior in metals had introduced quantum mechanics rather than the classically derived Boltzmann probability distribution, Sommerfeld clung to the idea that electrons in metals moved freely as do gas molecules in a container. Bloch was skeptical of this point of the Sommerfeld model.⁴⁴

The Bloch model for behavior of electrons in metals shortly followed the publication of Erwin Schrödinger's wave equation for the wave-particle duality of matter. The time-independent form of the wave equation is:

$$\left[-\frac{\hbar^2}{2m} \nabla^2 + \mathcal{V}(\vec{r}) \right] \psi = \mathcal{E} \psi \quad (26)$$

The term \hbar is Planck's constant divided by 2π (1.055×10^{-34} J • s), m is the particle mass, and $\mathcal{V}(\vec{r})$ is the particle potential energy function. The term ψ is the wavefunction for the particle described by the equation, and ∇^2 is the second order differential operator. The significance of the wavefunction ψ is that the square of the wavefunction (or its square modulus, if ψ is complex) is proportional to the probability of locating the electron at position \vec{r} . Generally, the process of solving a Schrödinger wave equation is one of determining the correct functions for ψ and $\mathcal{V}(\vec{r})$. The first and leftmost set of terms in the brackets of Equation (26) represent the kinetic energy of the particle under consideration and \mathcal{E} represents its total energy. The vector \vec{r} describes the Cartesian coordinate position of the electron within the crystal lattice.

Bloch sought to apply the Schrödinger equation to the description of electrons within metals. The Bloch model for metals as described by Blakemore⁴³ was based upon several assumptions:

- The Schrödinger wave function ψ is calculated for a perfect periodic lattice, with no vibrations or defects.

- The Bloch model is a description for a single electron. This electron ‘sees’ an effective potential of $v(\vec{r})$ for everything else in the lattice. This effective potential is not identical to the Schrödinger potential energy $\mathcal{V}(\vec{r})$.
- The electron is described by a one-electron Schrödinger equation (previously given as Equation (26)).

Bloch reasoned that the potential $v(\vec{r})$ experienced by the electron was the sum of two components.

The first part of $v(\vec{r})$ is the electrostatic potential of the positive ion cores that remain fixed in the crystal lattice following loss of an electron to the delocalized population of electrons. This potential is periodic, repeating with the frequency of the unit cells in the metal crystal lattice structure. The second part of $v(\vec{r})$ is the electrostatic potential of all other outer shell electrons. Like the positive ion core potential, this force is also presumed to repeat with the periodicity of the unit cells of the lattice. The total potential $v(\vec{r})$ is related to the Schrödinger potential energy function $\mathcal{V}(\vec{r})$ by the equation:

$$\mathcal{V}(\vec{r}) = -ev(\vec{r}) \quad (27)$$

where e is the elementary charge (1.6022×10^{-19} C). The Bloch solution for the lattice electron wavefunction ψ is:

$$\psi_k(\vec{r}) = U_k(\vec{r}) \exp(i\vec{k} \cdot \vec{r}) \quad (28)$$

The term \vec{k} is a wave vector that describes the direction and periodicity of the wave associated with the electron. The wave vector \vec{k} is related to electron momentum described by the equation

$$\vec{k} = \frac{\vec{p}}{\hbar} \quad (29)$$

where \vec{p} is the momentum vector for the electron. The Cartesian scalar components of \vec{k} are k_x , k_y , and k_z . These scalar components comprise a spatial system known as k-space. The term i in

Equation (28) is imaginary root of negative one. Lastly, the function $U_k(\vec{r})$ is a function with the periodicity of the crystal lattice, whose form is dependent upon the value of \vec{r} .

The solution of the Bloch wavefunction given in Equation (28) describes a partition of the electrons within a bulk solid into zones that are referred to as bands. Imaginary values of the wave vector \vec{k} lead to real values for the exponential term of Equation (28) and the equation diverges. This circumstance describes a forbidden zone for electrons. The converse, when \vec{k} is real, leads to an imaginary value for the exponential term. Under this circumstance, Euler's formula is applicable and Equation (28) becomes:

$$\psi_k(\vec{r}) = U_k(\vec{r}) \left[\cos(\vec{k} \cdot \vec{r}) + i \sin(\vec{k} \cdot \vec{r}) \right] \quad (30)$$

Equation (30) describes a wave that is capable of infinite propagation in a perfect crystal lattice. This equation describes an allowed band for the electron.

The partitioning of electrons in a metal can be demonstrated by examination of a one-dimensional lattice. A one dimensional lattice model would consist of a large number of ions, spaced periodically and arranged in a line as shown in Figure 5:

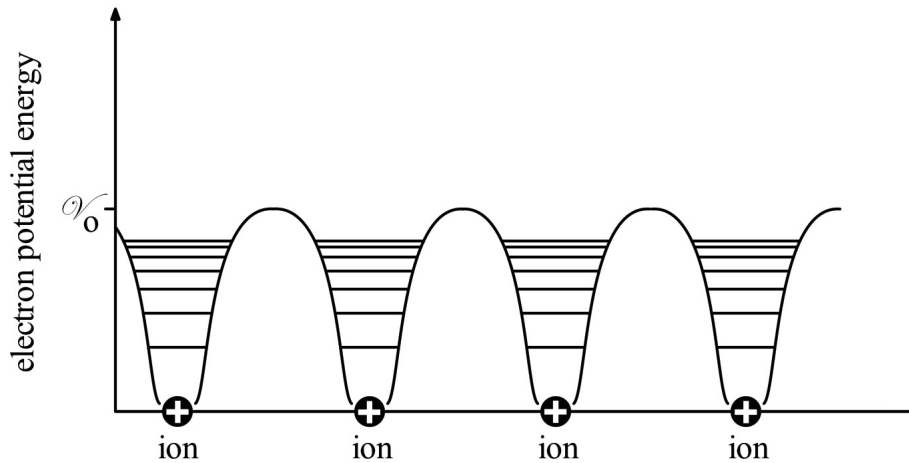


Figure 5: A hypothetical one-dimensional lattice.

The ion elements of the one-dimensional lattice acquired a positive charge through donation of an outer shell electron to the delocalized conduction electron population

From the perspective of a conduction electron, each ion is the center of an electrostatic potential field. In order for an electron to ‘escape’ from an ion potential well, either it must acquire energy greater than \mathcal{V}_0 or it must pass through the energy barrier separating it from an adjacent ion by a quantum tunneling mechanism.

The calculation of a wavefunction for a one-dimensional lattice such as Figure 5 can be greatly simplified by assuming the wells are rectangular. Kronig and Penny described Bloch wavefunction calculations for a series of rectangular potential energy wells in 1931.^{43, 45, 46} While the Kronig–Penny model surely is an oversimplification, it does demonstrate the evolution of band and band gap structures for delocalized electrons in crystal lattice structures. While the example that follows is limited to a one-dimensional array, these techniques can be extended to three dimensions for the description of electron behavior in solids.

The Kronig–Penny model consists of rectangular wells of width a , separated by rectangular barriers of width b and potential energy height \mathcal{V}_0 . The arrangement of wells and barriers is periodic and while Figure 6 only shows four wells and barriers, a larger number is assumed to comprise the one-dimensional array.

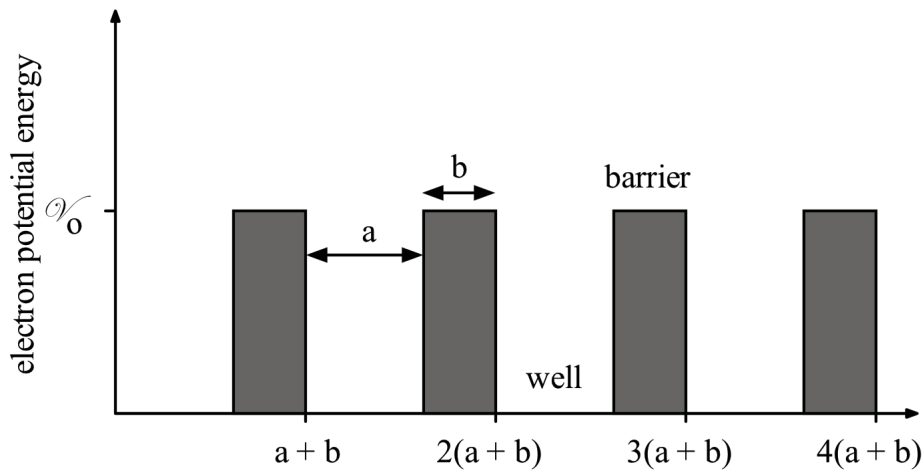


Figure 6: The Kronig-Penny model.

Like the ion lattice of Figure 5, the available pathways for an electron to leave a well in Figure 6 are either to exceed the well potential energy \mathcal{V}_0 or to tunnel through a barrier.

If the barriers in the Kronig-Penny model are thin enough to allow unimpeded passage of electrons between wells, the energy E of an electron is given by the dispersion relationship:

$$E = \frac{\hbar^2 k^2}{2m_e} \quad (31)$$

The terms \hbar and m_e have their previously described values and the term k is the magnitude of the electron wave vector \vec{k} . At the other extreme, when the barriers of Figure 6 are too thick to permit any quantum mechanical tunneling, the energy of an electron trapped in a well is given by:

$$E_n = \frac{n\pi^2 \hbar^2}{2ma^2} \quad \text{where } n = 1, 2, 3, \dots \quad (32)$$

For the intermediate case, where barriers allow only some tunneling, the electron wave vector \vec{k} and electron energy are related by the equation:

$$\cos(ka) = \cos(\alpha a) + P \left[\frac{\sin(\alpha a)}{\alpha a} \right] \quad (33)$$

The term α is related to electron energy by:

$$\alpha = \left[\frac{2m_e E}{\hbar^2} \right]^{1/2} \quad (34)$$

The term P in Equation (33) is a descriptor for the resistance of the Figure 6 barriers to electron tunneling:

$$P = \frac{abm_e V_0}{\hbar^2} \quad (35)$$

If the term P in Equation (33) is set at a finite value, the equation will alternate between real and imaginary values of the wave vector magnitude k . Values for $\cos(k\alpha)$ greater than 1 or less than -1 correspond to imaginary k values, and the wave vector \vec{k} describes a forbidden energy state for the electron. Alternately, when the magnitude of $\cos(k\alpha)$ is less than or equal to 1, k is real and the corresponding wave vector \vec{k} is associated with an allowed energy state for the electron. The regions of allowed energy states for the electron are analogous to electron bands, and the forbidden zones are the band gaps:

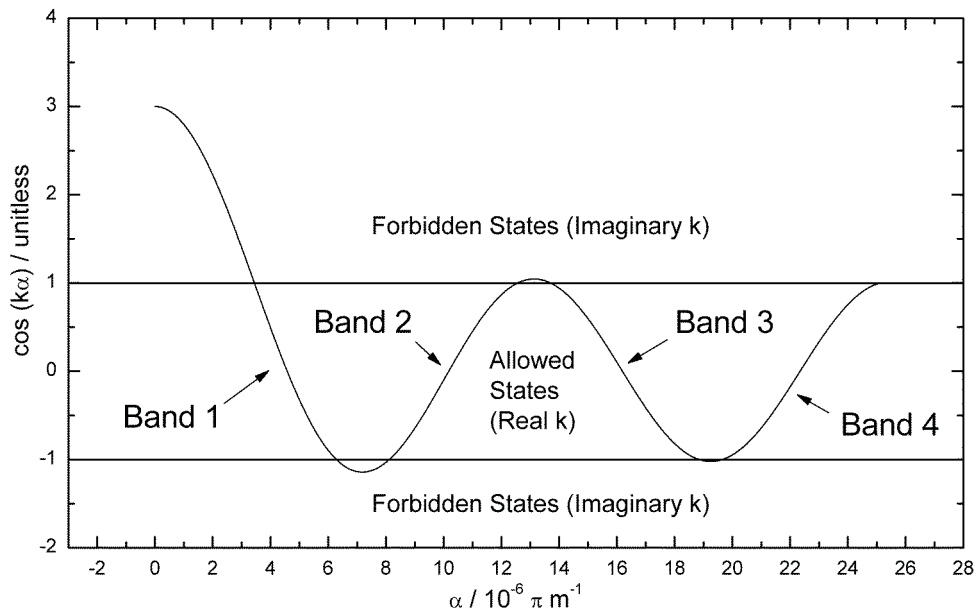


Figure 7: Alternating Kronig-Penney model forbidden and allowed electron energy states.⁴³

If the values of $\cos(k\alpha)$ in Figure 7 that fall between 1 and -1 are solved for k and plotted against their corresponding energy values from α , the band structure for the Kronig-Penney model becomes apparent. A plot for an unrestricted electron ($P = 0$) is indicated by a broken line for comparison:

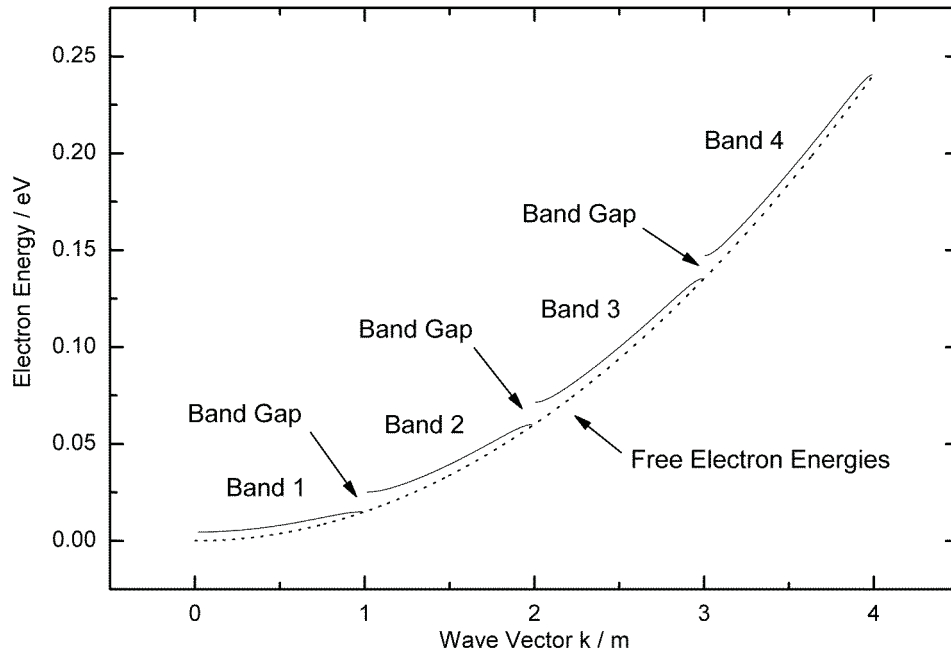


Figure 8: Electron band structure for the Kronig-Penny model for a value of $P = 2$. The broken line represents electron energies for a free, unrestricted electron ($P = 0$).

An alternate description of the formation of band structure arises from consideration of atomic and molecular orbitals in the solid state. The tight-binding approximation used in solid-state physics begins with the assumption that a macroscopic sample of solid phase material behaves as a single macromolecule. The overlap of atomic orbitals within heteronuclear solid-state materials leads to the formation of discrete molecular orbitals. As the number of atoms in a bulk solid phase sample increases ($> 10^4$ atoms)⁴⁷, atomic and molecular orbitals become confined within a physical space comparable to the spatial dimensions of their associated wavefunctions. The result is that the orbitals overlap and discrete orbital structure merges into delocalized band structure for the whole solid.⁴⁸ Just as no two electrons within an atom may have the same set of quantum numbers, no two electrons existing within the band structures for the bulk crystalline sample may have exactly the same energy state. This energy state exclusivity within the band structures for electrons in crystal lattices causes a Boltzmann-like distribution of energy states within the bands.

1.2.5 Band Structure Classification of Solid Phase Matter

Solid phase matter can be classified based on its electrical conductivity. A material whose electric conductivity varies inversely with temperature is a conductor. Solid phase conductors are characterized by partially filled valence bands that allow electron mobility, as shown in Figure 9a. As the temperature of a conductor is increased, lattice vibrations cause an increase of collisions between charge carriers and the lattice ion cores. The result of this increasing frequency of carrier-ion collision is that the charge carriers are scattered from their paths under the influence of an externally applied field and conductivity decreases.

A semiconductor is a material characterized by a directly proportional increase in electric conductivity with increasing temperature. Semiconductors are materials whose valence bands are completely filled, with conduction bands sufficiently close for excitation of electrons to the conduction band to be feasible. Figure 9b and c give the corresponding diagrams for a semiconductor before and after electron excitation to the conduction band, respectively. Following excitation, two modes of electric current conduction become available. The electron excited to the sparsely populated conduction band has freedom of movement, and the vacancy created by the departed electron in the valence band provides a 'hole' for adjacent electrons to move to. The overall effect for the excited semiconductor in Figure 9c is that electric current is carried by both the valence and the conduction band. Because thermal excitation of electrons into the conduction band is a possibility for some narrow band gap semiconductors, the conductivity of semiconductors as a class of materials is described as increasing directly proportional with temperature.

A third possibility for solid phase matter is shown in Figure 9c. Here, the valence band is filled as was the case with a semiconductor, but the band gap is too large for significant excitation of electrons to the conduction band to occur. These materials are referred to as electric insulators, although they are actually large bandgap semiconductors. Crystalline sodium chloride is an example of an insulator, with a band gap of approximately 7 eV.⁴⁹

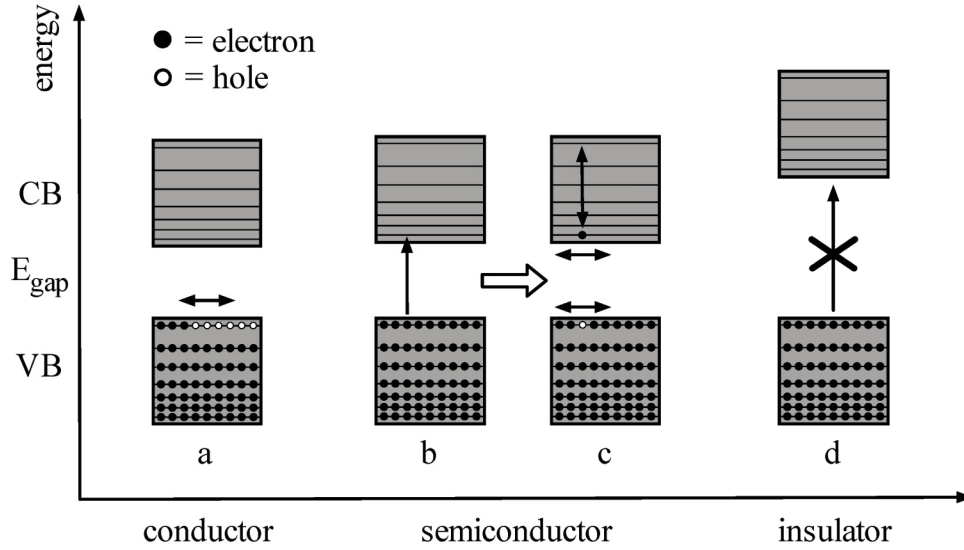


Figure 9: Classification of solid phase materials from band structure. VB is valence band and CB is conduction band.

The diagrams of solid-state band structure shown in Figure 9 are simplifications. A more accurate diagram of solid-state band structure is the plot of electron energy versus electron wave vector (i.e. \vec{k}). The proportionality of \vec{k} to electron momentum was previously shown in the wave vector definition given as Equation (29). Because of this proportionality, \vec{k} vector space is alternately referred to as \vec{k} momentum space. An example of semiconductor band structure in \vec{k} momentum space is shown in Figure 10. The parabolic shape of both the valence and conduction bands is a result of the expression for electron kinetic energy:

$$E = \frac{\rho^2}{2m_e} \quad (36)$$

where ρ is the electron momentum and m_e is the electron mass. The downward concavity of the valence band parabola symbolizes the decrease in energy an electron experiences when it is accelerated from maximum energy at $\vec{k} = 0$ in a partially filled valence band.

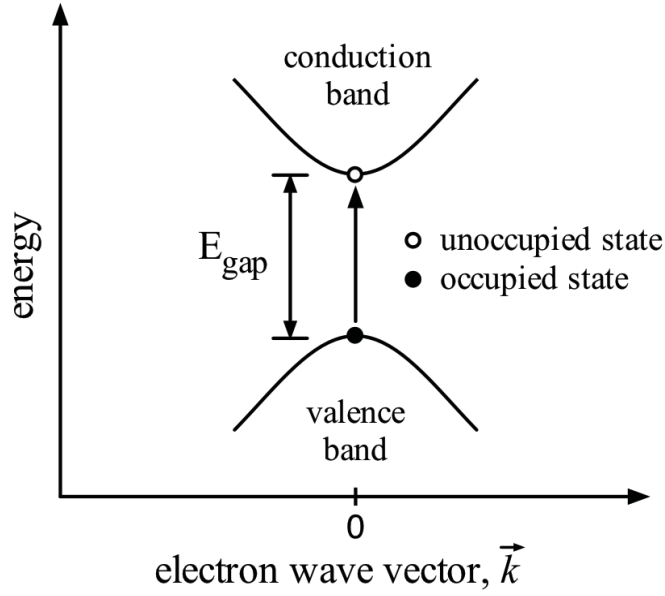


Figure 10: Semiconductor band structure for the electron energy as a function of the \vec{k} electron momentum vector.

Photon absorption processes (i.e. inter-band or intra-band electron excitation) should conserve the momentum of the electron.⁵⁰ When absorption of electromagnetic radiation occurs in a material, the absorption can be expressed as a function of the radiation energy:

$$A = \alpha(h\nu) \quad (37)$$

The absorption coefficient α is the rate of change for radiation energy as a function of path length, L along the axis of radiation propagation x :

$$\alpha = \frac{1}{L(h\nu)} \frac{d[L(h\nu)]}{dx} \quad (38)$$

The equation of the absorption coefficient expression defines the type of inter-band electron transition possible for a semiconductor.

Both the valence and conduction bands exist as a continuum of energy levels. For the valence band there will exist a highest energy occupied electron state and there will be a

corresponding lowest energy unoccupied state in the conduction band. The transition path between this highest occupied valence state and lowest unoccupied conduction band state can be described as either direct or indirect, depending upon whether the electron momentum \vec{k} changes during the transition.

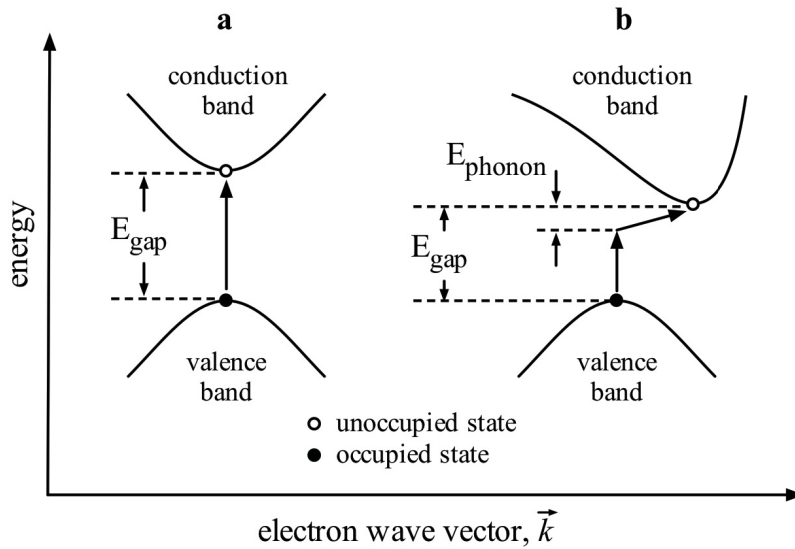


Figure 11: Direct (a) and indirect (b) semiconductor excitations. Adapted from Blakemore.⁴³

When the valence band maximum and conduction band minimum energies occur at the same momentum as shown in Figure 11a, the band gap transition is direct. For direct transition semiconductors the spectral absorbance is given by the expression:

$$\alpha(h\nu) = A^* (h\nu - E_{gap})^{1/2} \quad (39)$$

where A^* is a constant and E_{gap} is the semiconductor band gap energy difference. Examples of direct excitation semiconductors are cadmium sulfide (CdS) and gallium arsenide (GaAs).⁴³

When the valence and conduction band extrema occur at different momenta, as shown in Figure 11b, the transition is indirect. Indirect semiconductor spectral absorbance is given by the expression:

$$\alpha(h\nu) = B^* (h\nu - E_{gap})^{3/2} \quad (40)$$

where B^* is also a constant. Electron momentum is conserved during indirect transitions by coupling of the electron excitation absorbance to either the emission or absorption of a lattice phonon vibration. Examples of indirect excitation semiconductors include the elements silicon and germanium.⁴³

1.3 Titanium Dioxide

1.3.1 General Properties

The element titanium is the 9th most abundant in the Earth's crust.⁵¹ The Rev. William Gregor first noted titanium compounds in 1791 and in 1795 the element itself was recognized and formally named by Martin Klaproth.⁵² Titanium metal and its alloys possess a high strength-to-weight ratio and resistance to corrosion which have led to their widespread use for the fabrication of aircraft, missile, and submarine parts. These mechanical properties and titanium's biocompatibility make it useful for fabrication of medical implant devices such as those used for orthopedic repair and dental reconstruction.^{53, 54}

Titanium dioxide (or titania) has been observed extra terrestrially in the spectra of M-type red stars and in the composition of lunar soil samples returned during the Apollo missions.⁵¹ Titanium dioxide is a widely used industrial commodity. Until 2004 the U.S. Department of Commerce prepared an annual report of domestic titanium dioxide production and stockpiles and in 2003 the total annual U.S. production was reported as approximately 1.6 million tons.⁵⁵ While titanium dioxide is found in a wide variety of consumer products ranging from cosmetics to sunscreen formulations⁵⁶, its dominant application presently is in the production of paint. While macroscopic crystals of titanium dioxide are transparent, particles sized below the wavelength range of visible light (approximately 300 to 700 nanometers) disperse light to an extent that those particles appear to be white. This optical property of sub-micron titanium dioxide particles and their perceived low toxicity made this material an attractive alternative to lead based pigments that were banned in the United States in 1978 owing to the neurotoxicity of lead.^{57, 58}

While titanium dioxide is not known to possess the neurological risks associated with lead compounds, there is an accumulating body of research that indicates that nanoparticulate titania may hold other risks. Chronic inhalation of nanoparticulate titanium dioxide has been linked with pulmonary disease.⁵⁹⁻⁶⁷

The shift from lead-based white paint pigments to titanium dioxide inadvertently led to the discovery of the photocatalytic properties of titanium dioxide. The organic binder compounds in early titanium dioxide pigmented paints were observed to decompose following exposure to sunlight, resulting in ‘chalking’ of the paint surface.⁶⁸ Carl Renz published several papers in the early 1920’s from studies where he observed that titanium dioxide particles suspended in glycerine would change color from white to blue-gray or black following exposure to sunlight.⁶⁹ The titania color change noted by Renz was an indication that the titanium cations had undergone a photoinitiated reduction from Ti^{4+} to Ti^{3+} accompanied by extraction of titanium dioxide lattice oxygen to oxidize the glycerine suspension agent.

Titanium dioxide has been a popular subject of photocatalysis research for decades. Henrich and Cox described titania as “almost the prototypical transition-metal oxide in surface studies...”⁷⁰ in 1994, and the quantity of titanium dioxide research since that publication has not diminished. The popularity of this oxide is likely caused by its low cost, ease of preparation and handling, and wide range of intriguing physical properties.

Titanium dioxide is commonly found in nature as one of three crystalline polymorphs: anatase, rutile, and brookite. Under high pressure (4~10 GPa) titanium dioxide has been reported to undergo transformation to columbite, baddeleyite, and fluorite forms, but these polymorphs are not known to play a role in nanoparticle photo catalysis.⁷¹⁻⁷⁵ The polymorphs encountered in nanoparticle photocatalyst research are almost exclusively anatase and rutile. When examined in bulk form at ambient temperatures and pressures, rutile is the most thermodynamically stable form of titanium dioxide, although anatase is thought to be the most photo catalytically active polymorph.^{71, 76-78} Both anatase and brookite will convert to rutile upon heating, although the conditions for this conversion are thought to be dependent upon

particle size^{79, 80} with the thermodynamically favored polymorph shifting from rutile to anatase at particle sizes below 14 nm (1.4×10^{-8} m).⁸¹⁻⁸³ The unit cells for anatase and rutile are given in Figure 12.

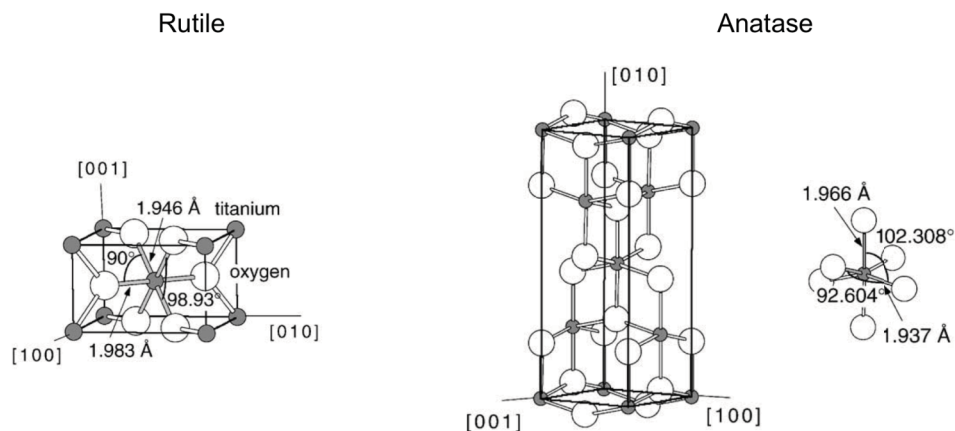


Figure 12: Unit cell structures for the rutile and anatase polymorphs of titanium dioxide. Reprinted from *Surface Science Reports*, 87, Ulrike Diebold, The surface science of titanium dioxide, 53-229, 2003, with permission from Elsevier.⁸⁴

Titanium dioxide is an n-type semiconductor. Both the rutile and anatase polymorphic forms of titanium dioxide are indirect band gap semiconductors.⁸⁵ The band gap energies for the three natural polymorphs have been determined by several investigators through spectroscopic measurements of single crystal or nanoparticle samples. Selections of these observations of band gap energy are presented in Table 1:

<i>TiO₂ Band Gap Energy, E_g / eV</i>			
<i>Investigator(-s)</i>	<i>Anatase</i>	<i>Rutile</i>	<i>Brookite</i>
Kim, et al. ⁸⁶	3.22		
Shibata, et al. ⁸⁷	3.20		3.26
Koelsch, et al. ⁸⁸	3.34, 3.39		3.40
Kavan, et al. ⁸⁵	3.2	3.0	
Tang, et al. ⁸⁹	3.2		

Table 1: Titanium dioxide single crystal and nanoparticle band gap energies.

Although it is possible to estimate the band gap energy for a sample of nanoparticles from diffuse reflectance spectroscopic measurements, particle size itself can influence this parameter through quantum confinement effects.

Upon excitation, an electron (e^-) and an electron hole (h^+) can become bound in a hydrogen like entity called an exciton. Excitons have quantized energy levels given by the equation:⁴⁸

$$E_{ex,n} = \frac{M_r}{m\epsilon_r^2 n^2} E_H \quad (41)$$

where m is the electron rest mass (9.109×10^{-31} kg)⁹⁰, ϵ_r is the dielectric constant of the semiconductor material, and n is an integer. M_r is the reduced mass of the exciton, given by the equation:

$$\frac{1}{M_r} = \frac{1}{m_e^*} + \frac{1}{m_h^*} \quad (42)$$

where m_e^* is the effective electron mass and m_h^* is the effective hole mass. Effective mass is the apparent mass of an entity exhibited during transport in a crystal lattice. Excitons can be weakly bound (large distance of separation between electron and hole), or strongly bound (small distance of separation between electron and hole). The energy necessary to create an exciton need not be equivalent to the band gap energy for the semiconductor.⁴⁸

Roduner described the considerations that determine whether strong or weak quantum confinement of electrons occur within a nanoparticle.⁹¹ The Bohr radii for an electron, a_e , and a hole, a_h , are given by the equations:

$$a_e = \frac{h^2 \epsilon_0 \epsilon_2}{4\pi m_e^* e^2} \quad (43)$$

$$a_h = \frac{h^2 \epsilon_0 \epsilon_2}{4\pi m_h^* e^2} \quad (44)$$

where h is Planck's constant ($6.626 \times 10^{-34} \text{ J} \cdot \text{s}$), ϵ_0 is the vacuum permittivity constant ($8.854 \times 10^{-12} \text{ J}^{-1} \cdot \text{C}^2 \cdot \text{m}^{-1}$), and e is the elementary charge ($1.602 \times 10^{-19} \text{ C}$). When the radius of a semiconductor particle approaches a_e , the bandgap energy for the particle increases. The lowest energy transition is given by:

$$\Delta E \approx \frac{h^2}{8Mr^2} \quad (45)$$

where r is the particle radius. The term M is either μ , the reduced exciton mass for cases where $r \ll a_e$ and $r \ll a_h$ (strong confinement), or M is the effective electron mass m_e for cases where $r \ll a_e$ and $r \gg a_h$ (electron confinement). The energy change for the lowest non-degenerate transition Z_3 can be written as:

$$\Delta E(Z_3) = E_g - E_b + \frac{0.67h^2}{8Mr^2} \quad (46)$$

where E_b is the exciton binding energy in bulk ($r \rightarrow \infty$) and E_g is the band gap energy. For either the case of strong confinement or electron confinement where $r \ll a_e$, the non-degenerate energy transition can be approximated by Equation (45) and Equation (46) can be rewritten as:

$$E_g = \frac{0.33h^2}{8Mr^2} + E_b \quad (47)$$

If E_b is taken to be constant, clearly as the particle radius r decreases the band gap energy E_g increases. The converse of this statement, band gap energy decreases (corresponding to a UV-Vis absorbance maxima shifted to longer wavelength) with increasing particle size, is observed experimentally. Kormann⁹² demonstrated an absorbance red-shift (i.e. absorbance shift to larger wavelength) for titanium dioxide during preparation of colloidal nanoparticles over thirty

minutes of particle growth. Other quantum confinement induced absorbance maxima shifts include those demonstrated by Wang and Herron for CdS nanoparticles⁹³, Lockwood for dissolving Si particles^{94, 95}, and King et al. for titanium dioxide films over the course of multiple annealing cycles.⁹⁶

1.3.2 Semiconductor Doping and Trap States

A semiconductor that relies solely upon the magnitude of its band gap energy for excitation of electrons to the conduction band is an intrinsic semiconductor. Often the band gap energy for a semiconductor is too large to permit adequate population of the conduction band to occur from room temperature thermal excitation alone. One approach to enhancement of valence band to conduction band electron excitation is to deliberately introduce a trace level contaminant, known as a dopant, to the lattice structure. Dopant materials are selected for their abilities to either contribute electrons to the conduction band or accept electrons from the valence band at energies significantly lower than the intrinsic band gap energy. Semiconductors that rely upon dopants to increase their electrical conductivity are known as extrinsic semiconductors.

Dopant atoms replace atoms within the crystal lattice structure, but their Bloch equation solutions are different from those of the semiconductor lattice in which they reside. Because the semiconductor dopants have different Bloch wavefunctions, dopants are able to reside within the forbidden band gap zone of the semiconductor. Dopant electron states that reside near the conduction band are electron donors, and the doping that occurs is n-type, where ‘n’ represents negative charge carriers (i.e. electrons).

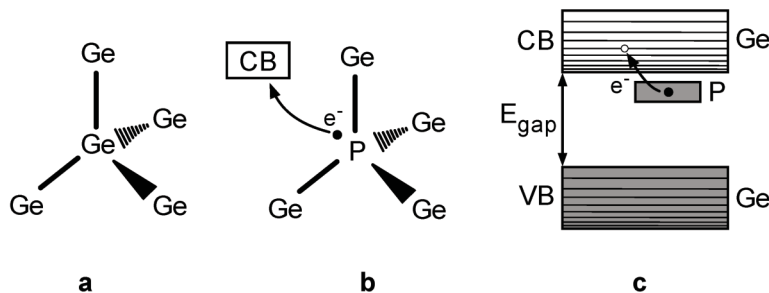


Figure 13: Phosphorus n-doping of a germanium semiconductor.⁹⁷

Figure 13 is an example of n-doping of a germanium semiconductor crystal by the addition of phosphorus. Like the carbon in a diamond, germanium atoms crystallize with a tetrahedral bonding geometry (Figure 13a). While germanium itself is an intrinsic semiconductor, the addition of trace amounts (less than one part in 100,000)⁹⁷ of phosphorus to the molten germanium during crystallization leads to the incorporation of the dopant phosphorus into the germanium lattice (Figure 13b). As a group V element, phosphorus is pentavalent and once incorporated into the germanium lattice it has an unused bonding electron. With a binding energy of 0.0046 eV to the P⁺ cation, this ‘extra’ electron is easily excited into the germanium conduction band at room temperature (298K), where the thermal excitation kT is only 0.025 eV (Figure 13c).⁹⁷ The phosphorus dopant electron states are not bound by the Bloch equations for germanium, and these phosphorus donor states lie just below the conduction band.

Dopants can also enhance semiconductor conductivity through acceptance of electrons from the valence band. Figure 14 describes positive charge carrier, p-doping of germanium. In this example the tetrahedral germanium bonding geometry (Figure 14a) incorporates a boron atom into its lattice structure during crystallization. As a group III element, boron is trivalent and there is a disruption in the germanium tetrahedral bonding network, indicated by a broken line in Figure 14b. The boron dopant atoms are able to accept valence band electrons from adjacent lattice germanium atoms. Once germanium atoms lose a valence electron, a positive charge carrier entity, or a ‘hole’, is created in the valence band and electron conduction is facilitated.

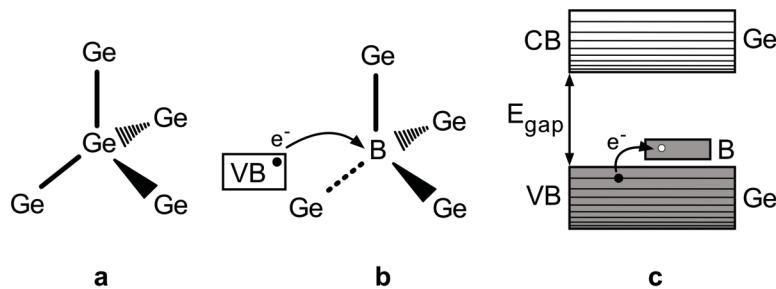


Figure 14: Boron p-doping of a germanium semiconductor.

Semiconductor doping is relevant to the electron trapping states of titanium dioxide nanoparticles. While the examples of semiconductor doping given in Figure 13 and Figure 14 were accomplished through introduction of trace-level foreign materials to the germanium crystal lattice, doping effects can also be accomplished through chemical reduction of a small fraction of the semiconductor. Titanium dioxide can be made non-stoichiometric through heating induced loss of oxygen from its crystal lattice. Figure 15 shows a schematic for the process by which electrons are trapped at surface states.

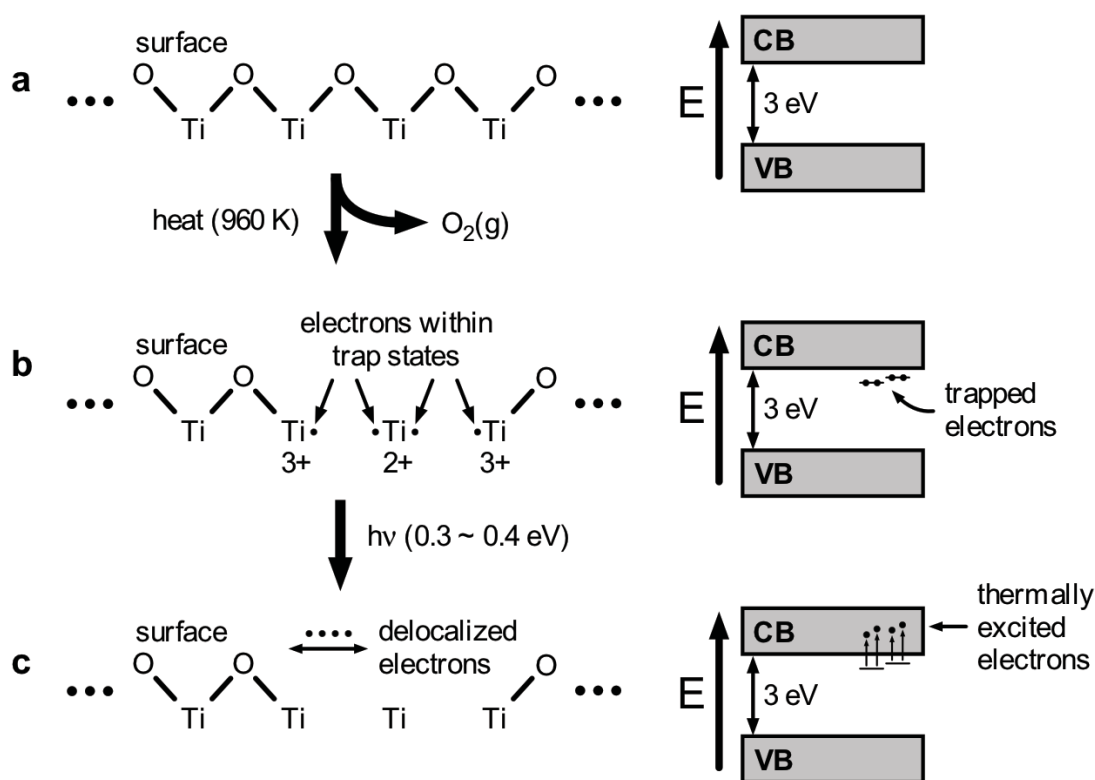


Figure 15: Titanium dioxide surface trapping of electrons.

Heating of the titanium dioxide in Figure 15a leads to the loss of oxygen from the titania crystal lattice. The oxygen departing the lattice leaves behind electrons which populate the Ti^{4+} 3d orbitals to form Ti^{3+} or Ti^{2+} as shown in Figure 15b. Because the Ti^{3+} and Ti^{2+} ions are not part of the Bloch equation solution that defines the TiO_2 band structure, these ions can energetically

exist within the band gap as sites of trapped electrons. Göpel et al. have shown with electron spectroscopy techniques that the titanium 3d orbital is energetically close to the titanium dioxide conduction band.⁹⁸ This evidence strongly indicates that reduced Ti^{3+} and Ti^{2+} cations are the sites of shallow trapped electrons. Ghosh et al. identified eight electron trapping Ti^{3+} defect states within the band gap of single crystal titanium dioxide from thermoluminescence and thermally stimulated current measurements.⁹⁹ Because of the large surface-to-area ratio of nanoparticles, the physical location of these trap sites is assumed to be on the particle surface.¹⁰⁰ Following their formation, the shallow trapped electrons are available for thermal excitation to the conduction band, as shown in Figure 15c. The formation of Ti^{3+} and Ti^{2+} defect states in the titania band gap is itself a type of intrinsic doping. Within semiconductor nanoparticles the number of trapped charges may greatly exceed the free electron population.¹⁰¹

While the repository of trapped electrons within the band gap of undoped titanium dioxide is likely the titanium cation itself, removal of oxygen is not the sole means of trapping electrons. The surface of nanoparticles feature step edges and corners, shown in Figure 16 on page 38, and the coordinate unsaturated titanium cations that exist at these surface features are susceptible to reductive electron trapping. Other sources of the electrons trapped at titanium ion lattice defects include electrochemical reduction¹⁰²⁻¹⁰⁴ and surface adsorbates¹⁰⁵. Injection of electrons into titanium dioxide nanoparticles from organic dyes is the mechanism through which titania nanoparticles have been incorporated into photovoltaic cells.^{18, 19, 100, 106, 107}

In addition to study of intrinsic Ti^{3+} trapped electron defects, the addition of dopants such as nitrogen¹⁰⁸⁻¹¹⁴, sulfur¹¹⁵⁻¹¹⁹, fluorine¹²⁰⁻¹²⁴ to titanium dioxide nanoparticles is an active area of research. Research reported in the literature indicates that the addition of these dopants either reduces the titanium dioxide band gap to energies that can be spanned by visible light, or these dopants form trap states in the band gap from which visible light or thermal excitation can promote electrons to the conduction band.

1.3.3 The Titanium Dioxide Crystal Surface

The unit cell of a perfect crystal lattice extends to infinity in all directions. Within a perfect lattice, an electron excited into a conduction band state will propagate infinitely with its associated Bloch wave function. This perfect crystal lattice is a construct useful for the derivation of theory but it does not describe a real crystal or a crystalline nanoparticle.

In contrast to the ideal cases, real crystals are bounded by surfaces. The surfaces of a crystal constitute a potential energy barrier that confines mobile charge carriers within the lattice. Electrons that have acquired sufficient energy within the lattice are able to overcome the potential energy barrier at the surfaces and escape the lattice. Thermionic electron emission from metals is a manifestation of electrons overcoming the lattice potential energy barrier.

Another aspect of crystalline surface asymmetry is reconstruction. The atoms or ions present on the surface of a crystal will rearrange so as to minimize the energy of the surface. This shifting of bond lengths and geometric positions for the surface layer will, in turn, alter the geometry of the lattice plane immediately adjacent to the surface layer. The truncation of a crystal lattice at the surface can leave atoms or ions incompletely coordinated, effectively able to bond to other species. Insufficiently coordinated surface ions can result in a reactive crystal surface. Quite often these terminal surface ions will minimize energy by reacting with atmospheric water to form hydroxylated surface species. A surface covered with highly polar hydroxy groups then becomes hydrophilic, i.e. wettable. Prevention or removal of surface coverage with atmospheric components represents perhaps the greatest challenge facing surface science researchers, necessitating the use of ultra-high vacuum approaches.

Another feature of the crystal surface is lack of uniformity. If the surface of a crystal was formed by removal of the atom or ion flux that lead to the crystal's growth, any irregularities that were present in the interior of the lattice structure will be represented on the surface, much like imperfections on a painted surface that result from underlying irregularities. If the crystal lattice was formed by cleavage of a larger crystal on a lattice plane, it is unlikely that the newly formed surfaces will be equivalent. Mechanical or thermal events may partially remove lattice ions from

the surface. Partial loss of lattice atoms en masse can either lead to the formation of terraces or islands on the surface. Discrete lattice component losses from the surface of a lattice can lead to isolated vacancies that interrupt the regularity of the surface pattern. Bombardment of the crystal surface by gas molecules can lead to 'foreign' adatom features on the surface. The final result of material transport to and from a crystal surface is an irregular terrain possessing many potential sites for surface reactivity and/or electron trapping. A very generic example of some of these surface irregularities is given in Figure 16.

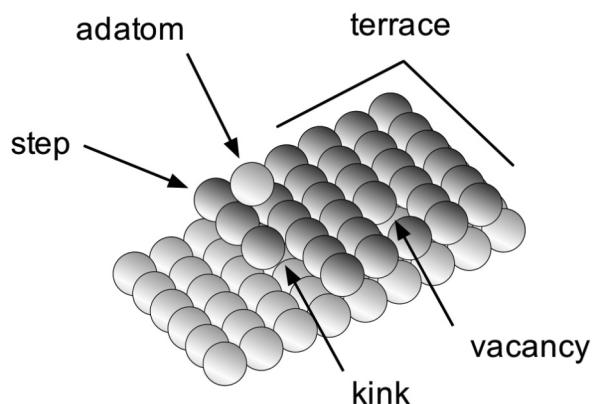


Figure 16: Surface irregularities on a crystal lattice.¹²⁵

The surface of titanium dioxide possesses several possibilities for charge trapping that are apparent on one of the surface reconstructions of the rutile polymorph. Electron trapping that is less than 1 eV below the conduction band edge is defined as shallow, while trap states that exceed 1.5 eV beneath the conduction band edge are defined as deep.¹²⁶

Figure 17 illustrates the (110) surface of the rutile titanium dioxide polymorph. Other possible surface configurations for rutile exist, but as a low energy configuration the (110) surface represents the most likely surface orientation to be encountered. This surface geometry possesses two structural features that play a role in electron trapping.

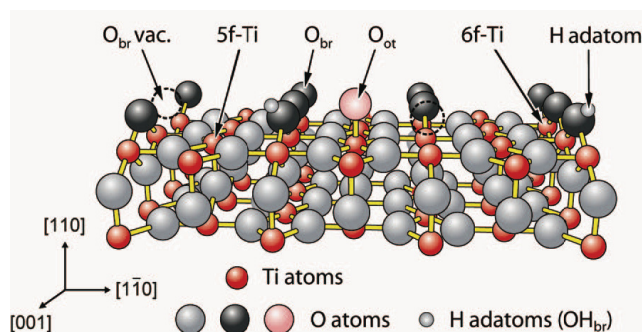


Figure 17: Aspects of the rutile TiO_2 surface. Reprinted with permission from Matthiesen, et al., Observation of All the Intermediate Steps of a Chemical Reaction on an Oxide Surface by Scanning Tunneling Microscopy. *ACS Nano* 2009, A-J. Copyright 2009 American Chemical Society.¹²⁷

Titanium cations within a titanium dioxide lattice are coordinated in a distorted octahedral geometry with oxygen anions. The rutile lattice is formed by a repeating orthogonal arrangement of these octahedral complexes. At the rutile surface, some of the complexes are truncated leading to the formation of coordinate unsaturated Ti^{4+} cations, indicated by ‘5f-Ti’ in Figure 17. These exposed, unsaturated Ti^{4+} sites are Lewis acid sites, capable of receiving electron density at their exposed face. In addition to forming bonds with reacting species on the surface of the nanoparticle, these sites are also susceptible to reduction, i.e. they can function as electron traps. Thompson has referred to the Ti^{3+} species within titanium dioxide nanoparticles as an electron trapped in the band gap region.^{126, 127}

Other octahedral complexes are oriented with their central axes normal to the lattice surface, leading to the formation of parallel rows of oxygen ions that bridge the Ti^{4+} cations immediately below. These rows of bridge bonded oxygen cations on the face of the lattice can be thermally excited to the point of leaving the lattice. Titanium cations left behind by thermal oxygen loss from the crystal surface acquire an electron and are reduced from the Ti^{4+} to Ti^{3+} state. These reduced titanium cations constitute surface sites of trapped electrons. Examples of bridge oxygen vacancies are indicated in Figure 17 by broken line sites where oxygen ions formerly resided. One such site on the far left side of the diagram is labeled ‘ $\text{O}_{\text{br}} \text{ vac.}$ ’. In addition to the possibility of being thermally driven off of the lattice entirely, the bridge oxygen ions in Figure 17 can function as Lewis bases and accept protonation. A protonated bridge

oxygen is indicated on the far right side of the Figure 17 by the ‘H adatom’ label. Hydroxyl groups located on the surfaces of titanium dioxide nanoparticles can function as hydrogen bonding sites, capable of promoting surface adsorption of complementary species. Szczepankiewicz has also identified surface hydroxyls as a site for delocalized shallow electron trapping.¹²⁸

Diagrams such as Figure 17 can lead to a mistaken conclusion that a crystal lattice, even a flawed one, is a static and passive terrain. The reality is that the surface of crystalline titanium dioxide is a highly dynamic and reactive locale. It is even possible to follow the movements of oxygen atoms and adsorbates from external sources in real time by electron tunneling microscopy, as has been recently demonstrated by Matthiesen.¹²⁷

1.3.4 Titanium Dioxide Nanoparticles and Shallow Electron Trap States

Nanoparticles have attracted intense research interest in part due to their phenomenally high surface areas which can reach hundreds of square meters per gram of material. This high ratio of area to mass produces an unusually large stage upon which chemical reactions can be orchestrated. The increased surface area of nanoparticles magnifies the contribution of crystal lattice defects to the particles’ chemical reactivity. A large surface area for nanoparticles translates into a large number of surface electron trapping states. Some researchers have noted that, on the surface of semiconductor nanoparticles, the density of trap states may greatly outnumber the population of mobile electrons.¹⁰¹

Ghosh identified six definite and two likely shallow trap states ranging from 0.27 to 0.87 eV below the conduction band edge in single crystal titanium dioxide from thermoluminescence and thermally stimulated current observations, and speculated that these trap states were likely Ti^{3+} reduced from Ti^{4+} in the crystal lattice.^{99, 129} The low energy gap between these states and the conduction band makes electrons residing in these traps thermally available for transport to the conduction band and participation in chemical reaction. Because shallow trap states are the result of either unsaturated Ti^{4+} or bound hydroxyl species attached to the titanium dioxide nanoparticle, these electron traps are a surface phenomenon. The trap states can function as

intermediate repositories for electron storage that permit surface catalysis to proceed at energies far below those required for direct valence to conduction band excitation.

1.4 Titanium Dioxide Nanoparticle Preparation

1.4.1 Liquid Preparation Techniques

Preparation of metal oxides from liquid reagent precursors is one of the simplest approaches to forming nanoparticles. Synthesis of particles in a liquid environment affords possibly the greatest level of control over the chemical environment under which the particles are formed. These procedures are performed with common laboratory equipment, simple techniques, and relatively inexpensive reagents. Because of this simplicity the majority of titanium dioxide nanoparticle research is conducted with materials prepared from liquid synthesis techniques.

To produce a nanoparticle is to grow a crystal. The challenge and principle difficulty is to control the size, size distribution, and geometry of the nanoparticles produced. Monodisperse particle growth, or the formation of discrete particles of identical size and shape, is the objective of most nanoparticle syntheses. Two approaches to nanoparticle synthesis have evolved: forced hydrolysis and colloidal particle, i.e. sol-gel techniques. Matijević and Sapieszko described the general conditions necessary to monodisperse nanoparticle growth from solutions by forced hydrolysis.¹³⁰

The first stage of nanoparticle growth within a solution is the formation of clusters from solvated ions. Following cluster formation, the formation of nanoparticle nuclei from the clusters must be accomplished. If the conditions under which these initial stages occur are not optimal, uncontrolled coagulation occurs.

Nanoparticle growth relies upon minimization of the electrostatic repulsion between the precursors in solution. This requirement is generally accomplished by control of the reaction solution pH to adjust the solvent environment to a point isoelectric with the surface precursor charge. Another approach is to increase the solution ion strength to a level where the precursor surface charges are screened from one another. Typical approaches to ion strength adjustment include addition of chlorides and sulfates.

Reactant concentration and time for particle growth also play important roles in the quality of monodisperse particle growth.. If precursor concentration is too high, uncontrolled agglomeration of crystallites will occur with rapid precipitation. Once optimal reactant concentrations have been determined, excessive prolongation of crystal growth will lead to an increase of variation in crystal size.

Matijević et al. are believed to have reported the first instance of monodisperse titanium dioxide particle synthesis from a titanium tetrachloride precursor with sulfate ion strength adjustment.¹³¹ This work was a continuation of earlier studies on metal oxide particle formation from hydrous sols.¹³² The Matijević titania particles ranged from 1 to 4 μm (1 to 4×10^{-6} m) which exceeds most definitions of a nanoparticle, but his techniques for particle growth were used in more recent work.

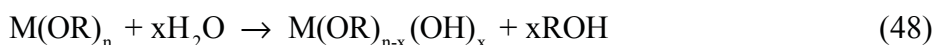
Kim et al. reported upon the preparation of a stable TiOCl_2 aqueous solution from which nanoparticles were latter prepared.¹³³ Their procedure began with slow addition of water to titanium tetrachloride cooled to 0 °C followed by dilution in distilled water. The resulting precursor reagent was reported stable for up to one year when stored at room temperature. Nanoparticle formation was accomplished simply by heating the TiOCl_2 solution to 100 °C. The particles produced were the anatase titania polymorph, exhibiting moderate crystallinity without further treatment. By altering the rate of solution heating, rutile nanoparticles were also prepared from the same TiOCl_2 starting material. The resulting nanoparticles were reported to be spherical with a mean diameter of 200 nm (2.00×10^{-7} m).

Other researchers¹³⁴⁻¹⁴² have continued forced hydrolysis of titanium tetrachloride with variations on the Matijević techniques. Addition of acid catalysts, use of nonaqueous solvents, changes in precursor concentrations, different crystal growth temperature regimes, and variation in nanoparticle growth time have all been applied to custom nanoparticle synthesis. The results of these studies have been nanoparticles with sizes from 10 to 50 nm that exhibit high photoactivity. In all of the cited works, the nanoparticles that were produced were agglomerated into fused growths of nanoparticles. The causes were likely particle collisions while growing in

solution and/or post synthesis heat treatments intended to increase crystallinity and alter the polymorph composition of the nanoparticles.

Sol gelation techniques for nanoparticle synthesis have become common in the literature. A sol is a suspension of solvated colloidal particles which do not precipitate. If these particles are allowed to grow until their structures merge, a gel is formed where solvent is captured within void spaces of the gel network. The structure remaining after removal of the solvent is a high surface area solid.

The sol-gel approach to nanoparticle synthesis is based upon synthesis of the colloidal particles followed by cessation of particle growth before a macromolecular gel network is formed. The precursor reagent is an organometallic compound, usually an alkoxide, that is easily hydrolyzed to form a hydroxide and an alcohol¹⁴³:



Formation of the particles proceeds by a condensation reaction where either water or alcohol is eliminated with the addition of each metal hydroxide unit:



Typically these reactions are conducted with the metal alkoxide and the water reactant dispersed into anhydrous organic solvents, with alcohols being the most frequently encountered solvent system in use. The reagent concentrations and molar ratio must be optimized to promote homogeneous sol growth rather than uncontrolled precipitation. Ogihara¹⁴³ identified the optimal range of alkoxide precursor concentration as 0.01 ~ 0.2 mol/dm³ with a corresponding water reactant concentration range of 0.05 ~ 0.5 mol/dm³ for monodisperse titanium dioxide nanoparticle preparation. The reactants must be completely mixed before the onset of particle

nucleation. Insoluble impurities must be removed from the reactant solutions prior to use, as extraneous particulates serve as unintentional nucleation sites. Finally, the stability of the colloid suspension must be maintained either through the use of steric or electrostatic repulsion.

Like forced hydrolysis, much work has been done to find optimal sol-gel reaction conditions for control of particle size, geometry, and composition. The alkoxide precursors used have generally been titanium tetraethoxide (TTE)¹⁴⁴, titanium tetra-n-butoxide (TTB)¹⁴⁵⁻¹⁵⁰, or titanium tetraisopropoxide (TTIP)^{148, 151-157}. The alkoxide is usually prepared in alcohol and added slowly to either concentrated acid catalyst (hydrochloric, acetic, or nitric acids) or combined with water dissolved in alcohol solution. Salt additives are sometimes used to direct the phase composition of the nanoparticles. The sol formed following the initial mixing of reactants is allowed to ‘age’ to promote nanoparticle growth for intervals ranging from hours to weeks. Deshpande et al.¹⁴⁹ even examined the effects of particle growth over one year.

The product of many sol-gel preparations are amorphous anatase nanoparticles. Crystallization of the nanoparticles and partial conversion to the more thermodynamically stable rutile polymorph is usually accomplished through heat treatment, referred to as calcining. The dried amorphous particles are heated to temperatures ranging from 100 to 900 °C for several hours, with samples of the particles taken at regular intervals for x-ray diffraction analysis of crystallinity and composition.

One negative outcome of calcination is that at higher temperatures, smaller nanoparticle coalesce into larger particles with a loss of surface area. Many researchers have attempted to avoid this alteration of nanoparticle size by inducing crystallinity with milder thermal treatment of the nanoparticles while they are still in solution.^{150, 153, 156}

Solvent based nanoparticle synthesis presents a relatively simple approach to production of particles of high purity and controlled composition. Unfortunately, preparation of monodisperse (i.e. uniform sized) non-aggregated nanoparticles through this technique remains difficult.

1.4.2 Vapor Pyrolysis

The commercially prepared titanium dioxide nanoparticle catalyst frequently used as a reference for comparison is Degussa (now Evonik A.G.) P25. This nanoparticle preparation has a mean particle size of 25 nm (2.5×10^{-8} m) and is estimated to be 80% anatase and 20% rutile. P25 titanium dioxide is prepared by flame hydrolysis of titanium tetrachloride. Flame hydrolysis operates by injection of a precursor reagent or reagents into a flame. Oxidation of the precursors takes place within the flame and particles of oxide accrete, sinter, and are ejected. Similar processes are used industrially for titanium dioxide paint pigment manufacture¹⁵⁸ and fabrication of telecommunications optical fiber.^{159, 160} The two methods frequently utilized by researchers for pyrolytic synthesis of titanium dioxide nanoparticles are the tube furnace reactor method and the laminar diffusion flame torch.

The tube furnace reactor¹⁵⁸ operates by accepting vaporized titanium precursor (typically titanium tetraisopropoxide) from a bubbler-nebulizer apparatus into a quartz tube that passes through an electric furnace. Within the furnace heated zone, the vaporized precursor reacts with oxygen and titanium dioxide particles are formed. During their passage through the furnace, the oxide particles grow and sinter. The nanoparticles exiting the tube furnace are captured in an electrostatic dust precipitator that uses a high voltage electric field to force the electrically charged nanoparticles to stick to an electrode. A schematic of the tube furnace reactor is shown in Figure 18. A similar process for continuous generation of titanium dioxide nanoparticles from a plasma induced reaction of titanium tetraisopropoxide and water within a tube reactor was recently described by Chen et al.¹⁶¹

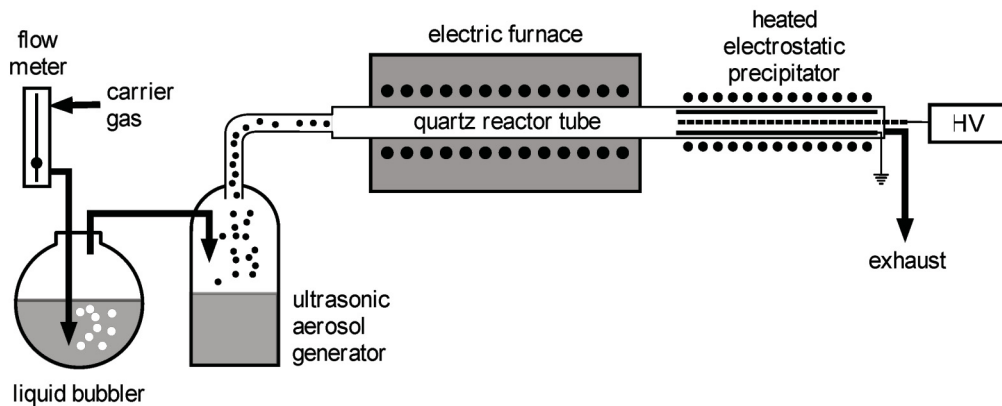


Figure 18: Titanium dioxide tube furnace pyrolysis reactor.¹⁵⁸

Pyrolysis of titania precursor within a torch flame, followed by nanoparticle collection in an exhaust hood or upon a water-cooled metal plate, is a more commonly found approach. Pratim Biswas¹⁶²⁻¹⁷⁶ has extensively researched the operational parameters of laminar flow torches used to hydrolyze titanium dioxide alkoxide precursors (usually titanium tetraisopropoxide). An example schematic of Biswas' titanium dioxide pyrolysis apparatus is given in Figure 19:

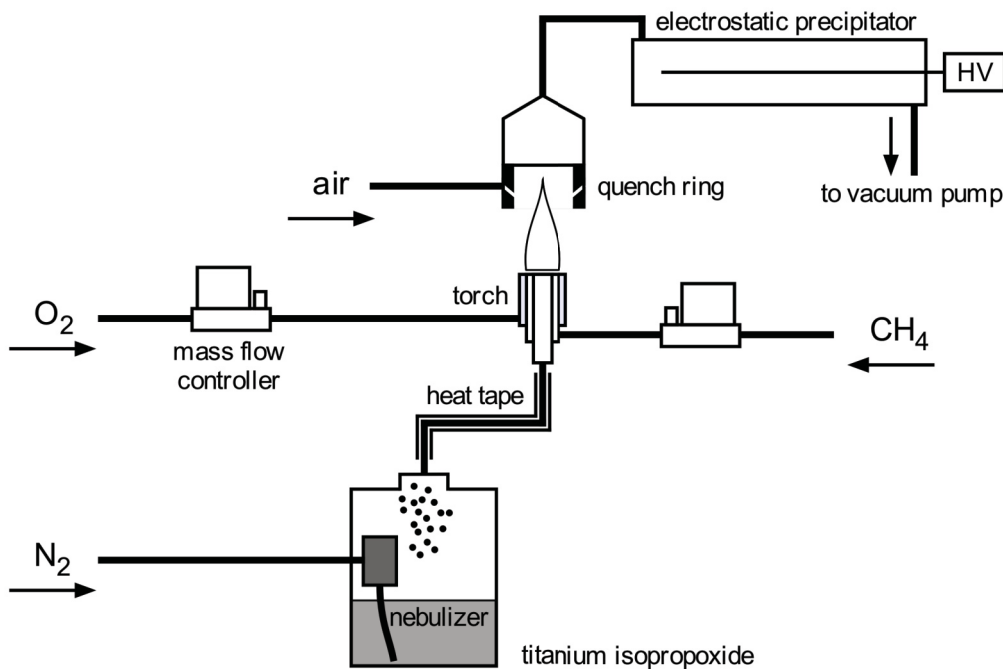


Figure 19: Flame pyrolysis nanoparticle generation.¹⁶⁸

The laminar flow torch used for vapor pyrolysis consists of concentric quartz tubes, into which individual gaseous components of the hydrolysis reaction are introduced. Mixing of fuel, oxidizer, and precursor vapor occur immediately above the torch head. One innovation of the Biswas apparatus is the air-cooled quench ring. This feature is used to direct jets of air onto the hydrolysis flame for the purpose of reducing nanoparticle aggregation through sintering. Particle collection from the flame is accomplished by drawing air into a conical metal hood affixed to the top of the quench ring and passing the air/nanoparticle stream through an electrostatic particle precipitator. In addition to the precipitator, instrumentation for characterizing nanoparticle morphology through light scattering behavior can also be attached to the downstream particle collection train. An alternative to the particle quench ring / collection hood assembly is a water cooled metal plate. The metal collection plate is attached to glass or silicon plates and this apparatus is used to study nanoparticle films, such as would be used for electrodes in photovoltaic cell fabrication.

The high temperatures associated with flame pyrolysis have several consequences. The high temperature environment in which nanoparticles are formed within the flame leads to greater crystallinity with less need for post synthesis calcination. Particle geometry from flame synthesis is almost exclusively spherical. The distribution of temperatures that exist within the torch flame can cause a polydisperse nanoparticle size distribution and cause extensive particle sintering into agglomerates. Sintering and agglomeration can be somewhat mitigated through alteration of operating parameters for the pyrolysis apparatus. While removal of particle size dispersion cannot be eliminated completely, the continuous operation mode of flame pyrolysis nanoparticle generation lends itself to application of particle size selection apparatus such as the multiple-stage differential mobility analyzer described by Chen et al.¹⁷⁷ and applied to flame pyrolysis by Jiang, Chen, and Biswas.¹⁶⁸

1.4.3 Laser Techniques

Synthesis of nanoparticles with laser induced vaporization carries several advantages over vapor pyrolysis conducted at or near atmospheric pressure.¹⁷⁸ Unlike a torch flame, a laser

beam does not require or generate near-atmospheric gas pressures. A laser can be set up outside of a closed chamber and its energy output can be directed by optics into that chamber to heat a sample contained under vacuum conditions or some non-atmospheric gas regime. This ability to remove the source of material heating from the experiment locale reduces the likelihood of contamination of both the precursor materials and the final nanoparticle product by making greater control of the experimental conditions possible.

Lasers are capable of generating greater temperatures than conventional flames. Direct vaporization of refractory metal oxides and high melting point metals becomes possible with laser heating. Laser heating of nanoparticle precursor materials in an enclosed chamber opens the possibility of reactive synthesis by simply introducing small quantities of gas. A pure metal sample can be vaporized to form nanoparticles and either during the vaporization or immediately afterwards, a small quantity of oxygen can be introduced to form metal oxide nanoparticles. Changing the gas to nitrogen can produce the corresponding metal nitride. Altering the pressure of a gas or gases admitted to the experiment chamber for reactive synthesis can influence the stoichiometry of the resulting compounds and profoundly change their characteristics.

The configuration of a chamber for synthesis of nanoparticles is not complex. A generic system is diagrammed in Figure 20. A pellet or rod of the precursor material is mounted in the synthesis chamber on an apparatus that allows for rotation positioning during operation of the chamber. Unless the chamber is designed in a manner to place the enclosed precursor target on the laser beam axis, front-surface mirrors are used to direct the beam into the chamber through a window selected for its transparency to the laser operating wavelength. The nanoparticles that condense from the laser heated vapor can be collected on a stationary surface inside the chamber (Figure 20a) or can be withdrawn outside the chamber through a sampling port (Figure 20b) operated at a lower pressure than the interior of the chamber. Chamber pressure is controlled by an attached vacuum system and the controlled introduction of reagent gases.

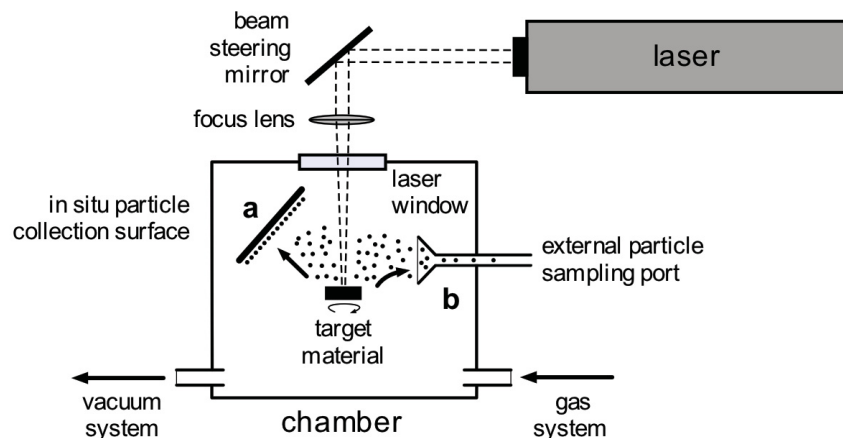


Figure 20: A typical setup for synthesis of nanoparticles with laser heating. Nanoparticles are captured on a stationary collector surface (a) or are removed from the chamber during synthesis (b).

Nd – YAG (neodymium - yttrium- aluminum - garnet) solid-state lasers are a common choice for nanoparticle synthesis.¹⁷⁸⁻¹⁸² Although these lasers operate on a fundamental wavelength of 1.06 μm , generating higher order harmonics can be used to create wavelengths of 0.213, 0.265, 0.355, and 0.530 μm .¹⁸³ Nd-YAG lasers can be operated in continuous wave mode, although greater power output is achieved through pulsed operation.

Another laser used for nanoparticle synthesis is the carbon dioxide gas laser. These lasers operate on a fixed wavelength 10.6 μm in the infrared region of the electromagnetic spectrum. Carbon dioxide lasers are capable of higher power output than their Nd-YAG solid-state counterparts, with power levels of 1000 watts possible with continuous mode operation.¹⁸⁴ This high power capability makes CO₂ lasers a frequent choice for industrial applications where cutting or melting of material is required.

There are two approaches to laser operation for nanoparticle synthesis. Ablation is the result of pulsed laser operation. In this mode, a portion of the target material is rapidly heated, liquefied, and vaporized during the ‘on’ portion of the laser pulse cycle. With the short duration of a laser pulse, usually between $10^{-6} \sim 10^{-9}$ seconds, the removal of material from the target surface occurs almost explosively. With each pulse, the vaporized material that departs the target imparts momentum onto the bulk material it leaves behind. During the ‘off’ portion of the

laser pulse cycle, the target material has some time to dissipate energy from the immediately preceding pulse burst.

Continuous operation of a laser directed onto a target leads to vaporization operation. In this mode, the precursor target material remains molten in the region where the laser is focused, and the molten material vaporizes continuously. With no interruption in material vaporization, the environment of the synthesis chamber achieves saturation more rapidly and maintains conditions for continuous condensation of nanoparticles.

The dynamics of particle condensation for laser synthesis of nanoparticles can be complex. It is not unusual for solid fragments of the target material to be ejected during heating and become intermixed with the nanoparticles that condense from the gas phase. The wavelength of the laser beam will determine the nature of the gas environment. For titanium dioxide, Matsubara¹⁸⁵ and Kawasaki¹⁸⁶ note that if the wavelength of the laser is too great to impart energy greater than the precursor target band gap (i.e. the titanium dioxide 3.0 eV band gap), then the vapor environment that forms the nanoparticles will be molecular species such as TiO₂ and Ti₂O₃. A Nd-YAG laser operated at 266 nm wavelength will have a photon energy 4.66 eV, which exceeds the titania precursor target's band gap and makes possible complete dissociation of the TiO₂ solid into gaseous atoms and ions.

Laser nanoparticle synthesis does have some disadvantages. The cost of the equipment is high compared to liquid reagent nanoparticle synthesis or vapor pyrolysis. The nanoparticle yields are generally smaller, and particle aggregation still occurs.

1.5 Infrared Spectroscopy of Electrons

1.5.1 Evidence for the Infrared Detection of Conduction Band Electrons

The elements silicon and germanium are semiconductors, with band gap energies of 1.12 and 0.67 eV, respectively.¹⁸⁷ The transparency of silicon and opacity of germanium to infrared radiation were utilized by Becker and Fan¹⁸⁸ to demonstrate the absorption of infrared radiation by mobile charge carriers (i.e. delocalized electrons) in solid state matter. Their technique used photographic plates that were narrowly sensitized to radiation in the infrared region at 1.3 μm

(1.3×10^{-6} m) wavelength. The infrared sensitized plates were either covered with thin sheets (0.3 mm thickness) of elemental silicon or germanium and exposed. The silicon covered plate showed an image from its exposure whereas the germanium covered plate did not. The infrared transmittance of bulk germanium begins at 1.6 μm wavelength and above, so the cutoff at 1.3 μm is expected. The smaller bandgap of elemental germanium makes it more likely to absorb energy, either electromagnetic or thermal, with the result being valence to conduction band electron transitions. The larger band gap energy of silicon requires more energetic (shorter wavelength) radiation to initiate electron transitions and, as a result, the absorbance cutoff for silicon is lower at wavelengths of 1.0 μm and below.

Becker and Fan recorded infrared spectra for the thin sheet of silicon over the wavelengths of 0.8 to 2.3 μm (12500 to 4350 cm^{-1}) at temperatures from 77 K to 663 K. As the temperature of the silicon was increased, the baseline of its infrared spectrum shifted upward as a result of greater infrared absorbance.

This infrared absorbance trend as a function of temperature for bulk silicon can be explained by thermal excitation of its valence band electrons to the conduction band. At higher temperatures, the silicon became more infrared opaque as a result of more abundant thermal energy to initiate electron transitions. The infrared absorbance of silicon was shown to be directly proportional to the population of mobile electrons. The mobile electron population can only be increased by energy inputs sufficient to initiate valence band to conduction band transitions. This absorbance trend is analogous to the increasing spectral absorbance of a compound as a function of its concentration.

Shortly after Becker and Fan's work, Harrick¹⁸⁹ conducted a series of observations that confirmed infrared absorbance by mobile electrons. His experiments were conducted by noting the infrared absorbance of a germanium bar with one end heavily p-doped. The bar was inserted into a simple electric circuit, and infrared absorbance was recorded for varying populations of injected 'holes', which increase the mobility of valence band electrons. Harrick found that increasing the valence band electron mobility through hole injection registers a corresponding

increase in infrared absorptivity, and conversely an extraction of positive charge carrier holes diminishes electron mobility and reduces infrared absorbance.

1.5.2 Characteristics of the TiO₂ IR Baseline

The behavior of a titanium dioxide nanoparticle infrared spectrum baseline is the result of several interacting processes. The foremost contributor to the spectrum is the absorbance exerted by free charge carriers, i.e. the conduction band electrons. Secondary effects on the infrared spectrum result from lattice vibrations coupled to the conduction band electron absorbances.

The atoms or ions that constitute a crystal lattice are not static entities. Each atom or ion is capable of limited movement and this freedom results in lattice element oscillations about fixed positions. When an atom or ion displacement propagates through the lattice, the result is a quantized displacement wave known as a phonon.

Two types of distinct vibrational wave motion are possible within a crystal lattice. Longitudinal waves occur when the motions of atoms or ions are parallel or antiparallel to the direction of wave propagation. A transverse wave occurs when the direction of atom or ion displacement is orthogonal to the direction of wave propagation. Figure 21 shows examples of both kinds of wave displacement.

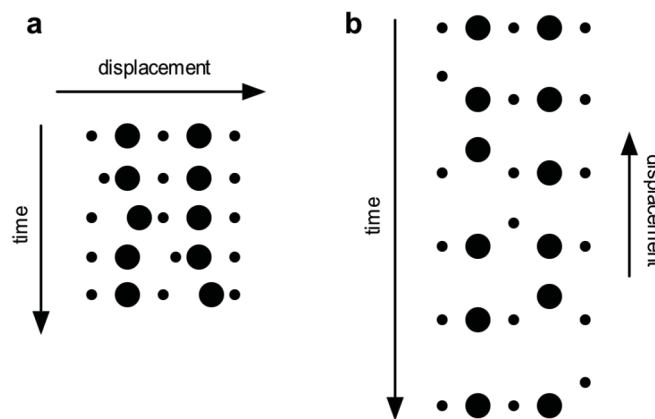


Figure 21: Vibrational wave propagation in crystal lattices. A longitudinal or compression wave is shown in (a) and a transverse wave is shown in (b).

Lattice phonons are classified on the basis of whether neighboring atoms or ions are moving in phase (concerted motion in the same direction) or out-of-phase (motion in opposing directions). When adjacent atom vibrations are in phase, the phonon is classified as acoustic, and when the vibrations are out-of-phase the phonon is classified as optical. Acoustic phonon motion couples to conduction band electron infrared absorbance and contributes to the titanium dioxide infrared absorbance spectrum behavior.

The solid line in Figure 22 is an absorbance spectrum recorded from titanium dioxide nanoparticles. This spectrum is representative of the baseline absorbance trends for titania nanoparticles commonly observed. The monotonic increase in the baseline absorbance from 3500 to 1200 cm^{-1} is caused by conduction band electron absorbance of infrared radiation. The conduction band is comprised of a continuum of states. Excitation of electrons into the band and transitions of electrons within the conduction band energy states leads to a Boltzmann-like electron energy distribution, as is illustrated in the Figure 22 inset.

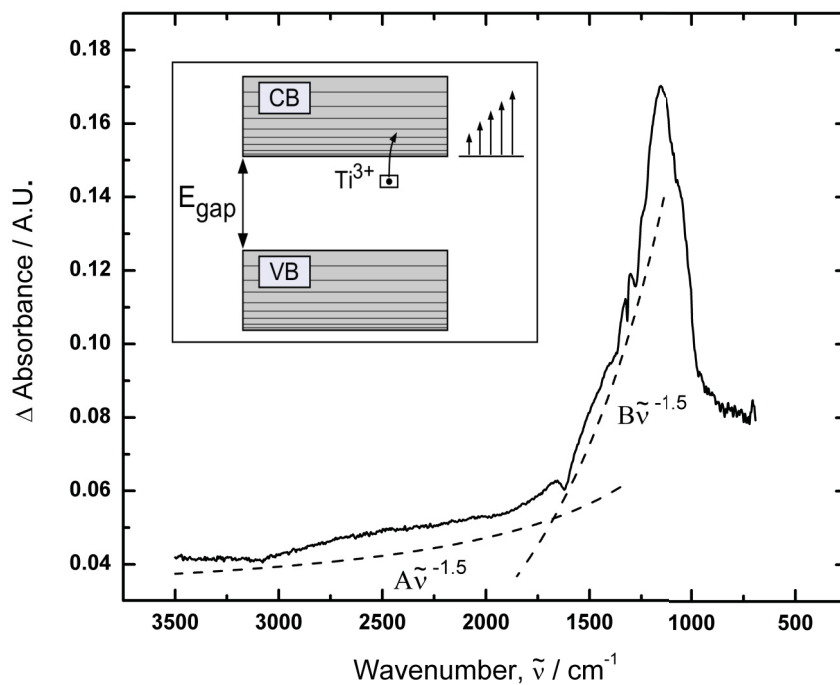


Figure 22: Phonon coupling to free carrier absorbance in titanium dioxide. The inset diagram¹⁹⁰ shows the origin of the conduction band (CB) electron energy states distribution from thermal excitation out of shallow trap state Ti^{3+} ion.

The large peak at 1200 cm^{-1} is due to phonon absorbance. At the low energies associated with radiation from 750 to 1200 cm^{-1} , the titanium dioxide lattice absorbance blocks infrared radiation from the spectrometer radiation source. From 1200 cm^{-1} to higher frequencies, two trends shape the baseline absorbance.

The infrared absorbance of free charge carriers (i.e. conduction band electrons) is described by the polynomial equation:

$$\alpha_f = A\lambda^{1.5} + B\lambda^{2.5} + C\lambda^{3.5} \quad (51)$$

where α_f is the free charge carrier absorbance.⁵⁰ The radiation wavelength is given by λ , and the variables A , B , and C are constants. When the expression is converted from wavelength to frequency, ν , the equation becomes:

$$\alpha_f = A'\nu^{-1.5} + B'\nu^{-2.5} + C'\nu^{-3.5} \quad (52)$$

A' , B' , and C' are also constants. The first term in Equation (51) with the 1.5 exponential gives the infrared absorbance of electrons coupled to lattice acoustic phonons. The second term with the 2.5 exponential is the conduction band electron optical phonon coupling absorbance. The last term with the 3.5 exponential is the absorbance for phonon coupling to ionized impurities in the crystal lattice. These term definitions for Equation (51) carry over to Equation (52) where the exponentials are inverted from the wavelength-to-frequency conversion. Between approximately 3500 to 1600 cm^{-1} and 1600 to 1200 cm^{-1} in the Figure 22 spectrum, acoustic phonon coupling to the conduction band electrons dominates the absorbance as is indicated by the slightly offset $A\tilde{\nu}^{-1.5}$ and $B\tilde{\nu}^{-1.5}$ trend lines shown for comparison. The change in phonon coupling trends at 1650 cm^{-1} might be attributed to superposition of two absorbance spectra. The additional spectral trend may originate from a thin layer of tungsten oxide (WO_3) formed on the surface of the tungsten mesh support at the tungsten-titanium dioxide interface.

The experimental apparatus used to obtain the spectrum shown in Figure 22 uses an electrochemically etched tungsten mesh for both mechanical support and resistive heating of the titanium dioxide nanoparticle samples. Details of this apparatus and sample preparation are presented in section 2.5.2 . The titanium dioxide nanoparticles that are observed with an infrared spectrometer are pressed into the openings of the tungsten support mesh, covering a circular region of approximately one centimeter diameter. The nanoparticle-mesh assembly is then oriented normal to the infrared spectrometer source beam within the sample compartment. This geometry causes infrared radiation from the instrument to enter numerous pores in the mesh where nanoparticles are packed. Oxidation of the tungsten support might occur either from gaseous oxygen introduced into the system during oxidative sample cleaning procedures, or from abstraction of lattice oxygen directly from the crystalline titanium dioxide at the nanoparticle-tungsten interface within the mesh openings as shown in Figure 23. Tungsten trioxide is an indirect semiconductor¹⁹¹ with a band gap energy similar to titanium dioxide (3.10 eV)¹⁹². The tungsten trioxide present as a thin coating on the support mesh within the sample orifices might contribute a weak absorbance signal as shown in Figure 23a. This additional signal, combined with the titanium dioxide absorbance spectrum in Figure 23b could produce a composite spectrum as shown in Figure 23b. This combined spectrum would have two acoustic phonon couplings, and thus two separate $\tilde{\nu}^{-1.5}$ absorbance trends.

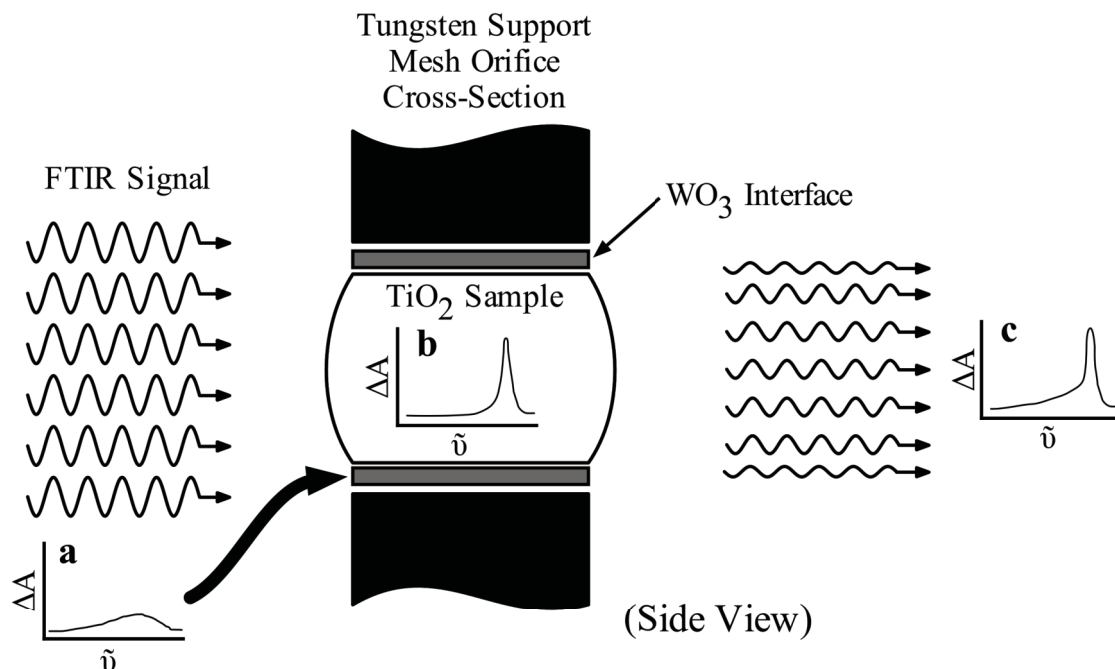


Figure 23: Superposition of interfacial WO₃ infrared spectrum (a) with TiO₂ sample spectrum (b) to produce observed composite infrared spectrum (c).

Perturbation of the infrared spectral baseline signal of titanium dioxide nanoparticles presents a sensitive measure of the electron density within that material's conduction band. The extent of thermal excitation of electrons to the titania conduction band for a given sample temperature can be a relative indication of the lattice defect density on the nanoparticles where electron trapping occurs. Electron trapping sites at the edge of the conduction band energy on the nanoparticles are the means for thermal catalysis of adsorbate reactions. Although multiple methods are available to characterize the energy difference between these shallow electron traps and the conduction band, infrared spectroscopy offers possibly the simplest approach. My goal is to demonstrate a method for accurately characterizing that electron shallow trap state energy difference for titanium dioxide nanoparticles from infrared spectroscopic data recorded over multiple sample temperatures.

1.5.3 Electron Density Measurement from Infrared Absorption

Electrons belong to the class of particles known as fermions. This class of particles is characterized by half-integral ‘spin’ (i.e. spin = $\pm 1/2, \pm 3/2, \pm 5/2, \dots$) and includes electrons, protons, ^1H nuclei, and ^{13}C nuclei. Particles that have integral spin (i.e. spin = $\pm 1, \pm 2, \pm 3, \dots$) are bosons, and include photons, ^2H nuclei, and ^{12}C nuclei. Use of the word ‘spin’ should not be taken as literal, rotational motion of the electron. The angular momentum characteristic of the electron, discovered by Goudsmidt and Uhlenbeck¹⁹³ is a parameter introduced by Dirac in his modification of the Schrödinger equation for an electron to account for the relativistic effects of electron motion.⁴⁰

As a fermion, the probability of electron occupancy of an energy state is described by the Fermi probability, $F(E)$:

$$F(E) = \frac{1}{1 + \text{Exp}\left(\frac{E - E_{Fermi}}{k_B T}\right)} \quad (53)$$

where k_B is Boltzmann’s constant ($1.381 \times 10^{-23} \text{ J} \bullet \text{K}^{-1}$), T is the thermodynamic temperature, and E_{Fermi} is the Fermi energy for that material.¹⁹⁴ A derivation of the Fermi probability expression is given in Appendix 1. Figure 24a shows the Fermi probability for a semiconductor at a nonzero temperature. The top of the valence band in Figure 24 is set as the zero energy, and the bottom edge of the conduction band is separated from the valence band by band gap energy, E_{gap} . Note from the Figure 24a magnified inset, that at $T > 0 \text{ K}$ the Fermi probability of electron occupancy of the conduction band is not zero.

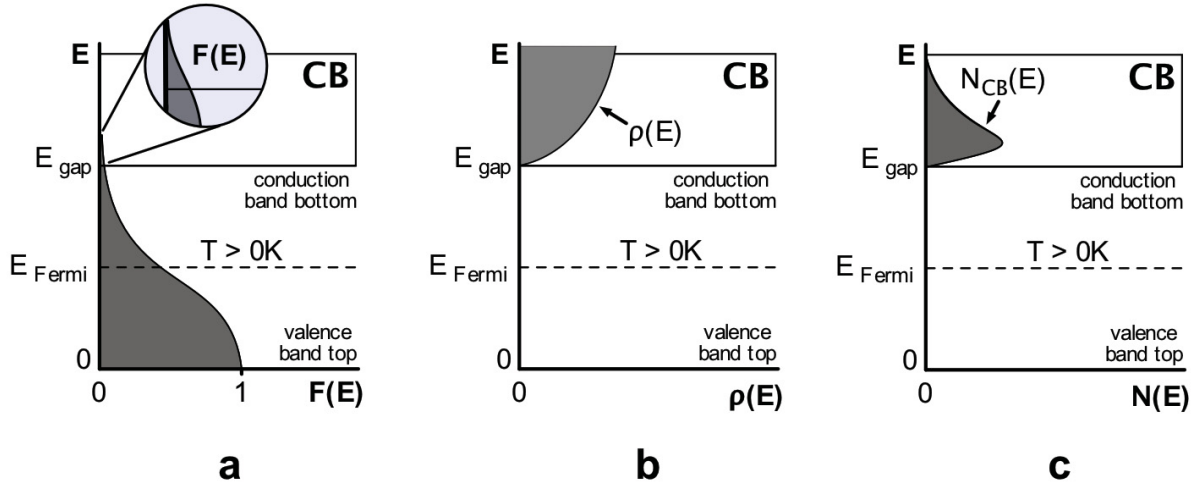


Figure 24: Development of conduction band electron density expression. The dark shaded regions are integrated areas.¹⁹⁴

The conduction band of a semiconductor crystal lattice is composed of a continuum of discrete energy states. The number of states with energy E that can be occupied within a crystal lattice is given by the density of states, $\rho(E)$:

$$\rho(E) = \frac{2^{7/2} m_e^{3/2}}{h^3} (E - E_{gap})^{1/2} \quad (54)$$

where m_e is the electron rest mass (9.1094×10^{-31} kg) and h is Planck's constant (6.626×10^{-34} J • s).¹⁹⁴ A derivation for the density of states expression is given in Appendix 2. Figure 24b shows the number of available conduction band energy states as a dark shaded region.

The density of electrons $N(E)$ between an energy state E and $E + dE$ in a crystal lattice is the product of the density $\rho(E)$ of those energy states in the lattice and the Fermi probability that those states will be occupied:

$$N(E)dE = \rho(E)F(E)dE \quad (55)$$

where dE is an infinitesimal increment of energy E . Substituting for $\rho(E)$ and $N(E)$:

$$N(E)dE = \frac{2^{7/2} m_e^{3/2}}{h^3} (E - E_{gap})^{1/2} \frac{1}{1 + \text{Exp}\left(\frac{E - E_{Fermi}}{k_B T}\right)} dE \quad (56)$$

The thermal energy available at a temperature T is given by $k_B T$. For the studies presented here the nanoparticle annealing experiments were run from an ambient temperature of 298 K to a final temperature of 675 K. The energy available at 675 K is approximately 0.058 eV. With E at the bottom of the conduction band for titanium dioxide, $E_{gap} - E_{Fermi}$ is approximately 1.5 eV, which is 30 times greater than $k_B T$. At the lower temperatures, this energy disparity is even greater, so an approximation can be made for the Fermi probability:

$$\text{Exp}\left(\frac{E - E_F}{k_B T}\right) + 1 \cong \text{Exp}\left(\frac{E - E_F}{k_B T}\right) \quad (57)$$

$$N(E)dE = \frac{2^{7/2} m_e^{3/2}}{h^3} (E - E_{gap})^{1/2} \text{Exp}\left(-\frac{E - E_{Fermi}}{k_B T}\right) dE \quad (58)$$

The density of electrons contained within the conduction band can be determined through integration of Equation (58) from bottom energy of the conduction band (E_{gap}) to top of the conduction band. The top of the band can be taken as $E = \infty$. The density of conduction band electrons, N_{CB} , is calculated from:

$$N_{CB}(E) = \int_{E_{Gap}}^{\infty} \rho(E) F(E) dE \quad (59)$$

$$N_{CB}(E) = AT^{3/2} \text{Exp}\left(\frac{-E_{Gap}}{2k_B T}\right) \quad \text{where} \quad A = \frac{2^{5/2} (m_e \pi k_B)}{h^3} \quad (60)$$

The dark shaded region in Figure 24c is proportional to the density of conduction band electrons at temperature T .

The focus of my thesis is to determine the energy of transition from a shallow trap state, just below the conduction band, into the conduction band. The thermal excitation is from E_{state} to the conduction band, and not across E_{Gap} . An appropriate substitution is:

$$N_{CB}(E) = BT^{3/2} \text{Exp}\left(\frac{-CE_{State}}{T}\right) \quad \text{where} \quad B = \frac{2^{5/2}(m_e \pi k_B)}{h^3} \quad \text{and} \quad C = \frac{1}{2k_B} \quad (61)$$

The infrared baseline absorbance for titanium dioxide nanoparticles at temperature T is proportional to the number of mobile electrons populating the conduction band. The relationship between the spectral absorbance and concentration of an absorbing species is given by the Beer-Lambert Law:

$$A = \epsilon bc \quad (62)$$

where A is the absorbance, ϵ is the molar absorptivity, b is the absorbing media path length, and c is the absorbing species concentration. The molar absorptivity term of the Beer-Lambert Law is a constant that is wavelength and material specific. The absorption path length for a solid sample can also be considered constant. Integration of the absorbances over a range of wavelengths (or wavenumber frequencies) for a given concentration of absorbing species will give an area that is proportional to the concentration of those absorbing species. The proportionality constant for this area-concentration relation is the integrated trend of the absorptivity constants as they vary with wavelength.

The population of electrons in the conduction band of a semiconductor absorbs infrared radiation over a broad range of wavelengths through intra-band electron transitions.¹⁹⁰ Once excited into the conduction band, a population of electrons will energy partition across the range of available energies (0.45 eV for the 4000 to 400 cm^{-1} infrared spectrum) in a Boltzmann-like distribution. It is this intra-band transition over the continuum of available electron states in the

conduction band that produces the characteristic baseline absorbance profile for the semiconductor. As more electrons enter the conduction band from increased thermal excitation, more electrons are present to absorb available energy and the baseline absorbance increases. The population of electrons observed under constant conditions within a fixed quantity of semiconductor material is an electron concentration. It follows from the Beer-Lambert Law that an integrated area Z under an infrared spectrum baseline is also proportional to the conduction band electron population:

$$Z \propto BT^{3/2} \text{Exp}\left(\frac{-CE_{State}}{T}\right) \quad \text{where} \quad B = \frac{2^{5/2}(m_e \pi k_B)}{h^3} \quad \text{and} \quad C = \frac{1}{2k_B} \quad (63)$$

If a proportionality constant D is introduced to Equation (63) a new equation is created that can be solved for the semiconductor shallow trap state energy, E_{state} :

$$Z = DBT^{3/2} \text{Exp}\left(\frac{-CE_{State}}{T}\right) \quad (64)$$

$$E_{State} = -\frac{T}{C} \ln\left(\frac{Z}{DBT^{3/2}}\right) \quad (65)$$

$$E_{State} = \frac{T}{C} \ln\left(\frac{DBT^{3/2}}{Z}\right) \quad (66)$$

A set of transmission infrared spectra can be recorded for a sample of titanium dioxide nanoparticles held at varying constant temperature setpoints. For each spectrum, a part of the baseline is integrated. The baseline area vs. nanoparticle temperature data set are fit to Equation (64) using nonlinear regression techniques where D and E_{state} are parameters of the regression. In this manner, the shallow trap state energy E_{state} can be experimentally measured with infrared spectroscopy.

Chapter 2: Nanoparticle Preparation, Characterization, and Spectroscopy

2.1 Introduction

My work with titanium dioxide nanoparticles began with synthesis of nanoparticles by laser evaporation techniques. This method of producing nanoparticles was chosen on the basis of an existing body of experience by previous researchers in our group, the greater likelihood of synthesizing nanoparticles free of contamination, and the simplicity of the preparation technique. Laser evaporation produces lower yields of titanium dioxide nanoparticles than solution based or flame pyrolysis techniques, but the resulting particles require no post synthesis calcination to induce crystallinity

Characterization of the nanoparticles principally consisted of examination by transmission electron microscopy. X-ray diffraction studies and high-resolution transmission electron microscopy was performed on a limited set of samples to confirm crystallinity and to determine which polymorphs (rutile and anatase) were present within the nanoparticles.

Nanoparticle samples were pressed onto a tungsten mesh and mounted for infrared spectroscopic examination under high vacuum conditions. Spectra were acquired under temperature controlled conditions, where annealing was accomplished by resistive heating of the tungsten support mesh. The resulting spectra were saved as text files, which were latter processed with custom FORTRAN 77 programs and Microsoft Excel[®] spreadsheets.

2.2 Nanoparticle Preparation by Laser Vaporization

2.2.1 Description of Apparatus

Nanoparticle preparation by laser vaporization was accomplished by use of the apparatus designed and constructed by Professor Brian Tissue^{195, 196} and later used by Dr. Wesley Gordon.¹⁹⁷⁻¹⁹⁹ The chamber itself is cylindrical, externally measuring approximately 54 cm in length and 20 cm in diameter, and constructed from stainless steel. The gas pressure within the chamber is controlled by pumping with an Alcatel 10 liter rotary vane pump and pressurization

from a regulated, ultra-high purity grade oxygen cylinder. Both vacuum and gas ingress to the chamber are controlled by user adjustable valves located at the chamber. The pressure within the chamber was monitored with a Granville-Phillips Model 275 Convecatron vacuum pressure sensor. The chamber pressure signal from the Convecatron sensor was read on an MKS Instruments Baratron type 107A analog display. The oxygen pressure within the chamber was estimated from calibration data supplied with the Convecatron sensor. Figure 25 shows a schematic of the vaporization chamber. The vaporization laser beam was focused with a zinc selenide lens external and adjacent to the chamber. The chamber side entry window for the vaporization beam was also formed from zinc selenide for infrared radiation transparency.

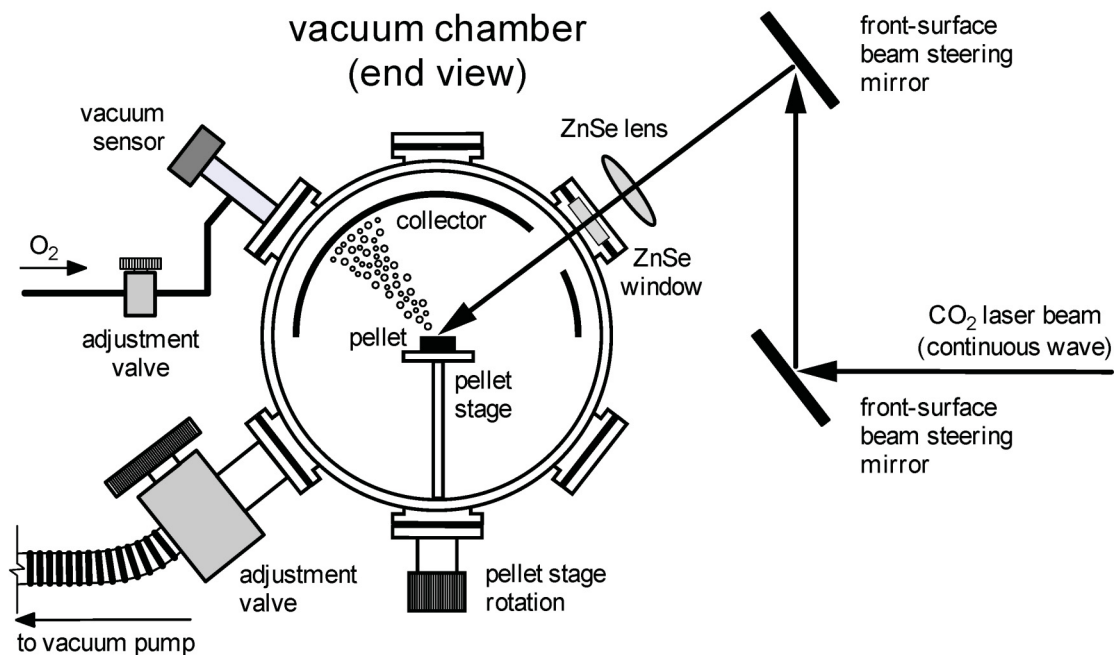


Figure 25: Schematic of laser evaporation chamber used for nanoparticle synthesis (end view). Adapted from Tissue.¹⁹⁵

The laser used for vaporization was a Syn Rad, Model 648-5-28W-1344 carbon dioxide laser. The maximum power rating of the laser was 100 Watts. Control of the laser was through a Syn Rad UC-1000 module, which featured pulsed and continuous operating modes and a

continuously variable power adjustment. The laser was water cooled with a recirculating water chiller. The laser beam was directed to the entrance optics of the vaporization chamber by an optical system diagrammed in Figure 26. The carbon dioxide laser beam passed through a 1:100 ratio beam splitter with the 1% reflected beam directed to a Melles Griot optical power sensor head, rated at 30 Watts maximum power. The digital readout display that accompanied the sensor head was set to read units of Watts. The effective vaporization laser power level was estimated by multiplication of the displayed power reading by a factor of 100X. Vaporization experiments were typically run at 100% power settings, which resulted in approximately 60 Watts laser power.

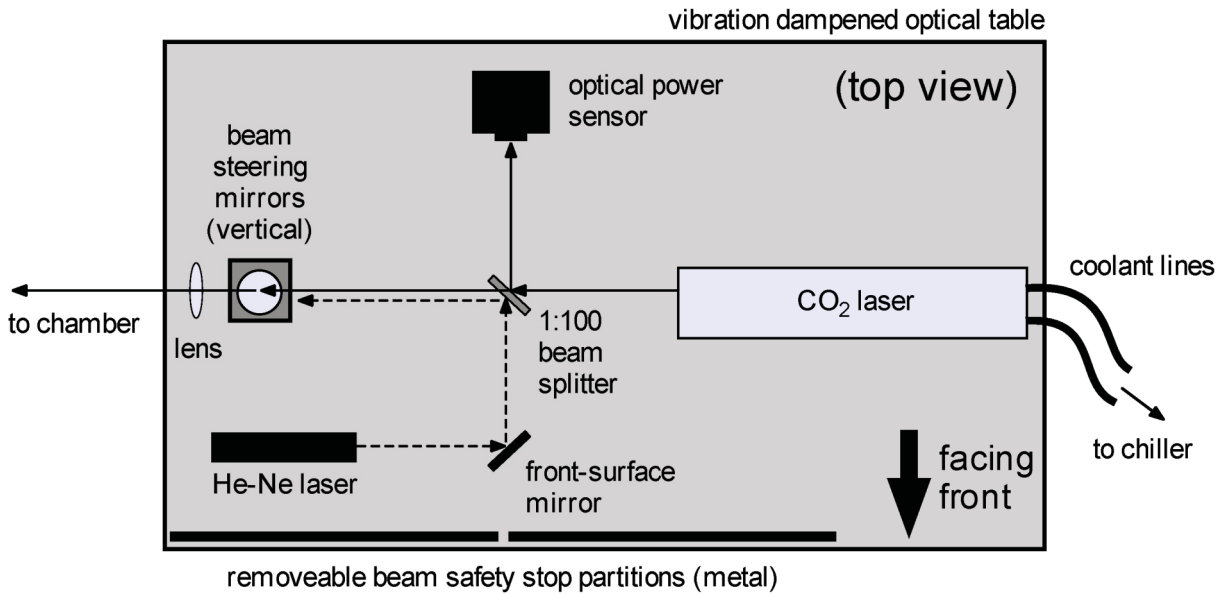


Figure 26: Vaporization chamber laser optics (top view).

Working in the presence of a 60 Watt laser beam, capable of heating ceramics to incandescence, makes heightened observance of safety precautions necessary. During operation of the vaporization laser, access to areas of the optical bench where the beam passes are blocked by two aluminum stop plates mounted on the front of the laser optical table. Prior to any operation of the carbon dioxide laser, a secondary low-power helium-neon laser, aligned coaxial

to the primary vaporization beam, is used to check the laser optics alignment. The greatest likelihood of beam misalignment is at the vertical beam steering mirror assembly adjacent to the vaporization chamber. Here, adjustment of the mirrors during laser operation to move the vaporization locale on the target pellet can lead to stray reflections from the mirrors, zinc selenide focusing lens, and/or the zinc selenide entrance window of the chamber. Prior to operation of the primary vaporization laser, checks are made in the vicinity of the chamber entrance port for unexpected He-Ne reflections from the optics system and alignment adjustments are made as needed to ensure that all laser beams are coaxial and directed only into the vaporization chamber.

A secondary purpose for the helium-neon laser is to check the path of the vaporization laser beam inside of the chamber. Prior to sealing and evacuating the chamber, the beam placement onto the appropriate region of the starting material pellet must be verified. The uninterrupted passage of the laser beam through the entrance orifice cut into the nanoparticle collector target surface also must be confirmed. Any irregularities in laser beam or collector surface alignment are corrected before operation of the vaporization laser.

Nanoparticle condensates are collected within the vacuum chamber on a stainless steel surface. The preferred collector geometry was a hemispherical dome arranged symmetrically above the starting material target pellet. Both the interior surfaces of the chamber and the collector hemisphere assembly were cleaned prior to use with 95% ethyl alcohol and laboratory wipe tissues. The collector hemisphere was supported upon an adjustable metal bracket and placed so that its lower edge was even with the top of the target pellet surface. Proper alignment of the collector dome allowed observation of the target pellet surface from a forward view port and unencumbered passage of the vaporization laser beam through another port, 90 degrees from the view port. Details of the hemisphere placement are given in Figure 27.

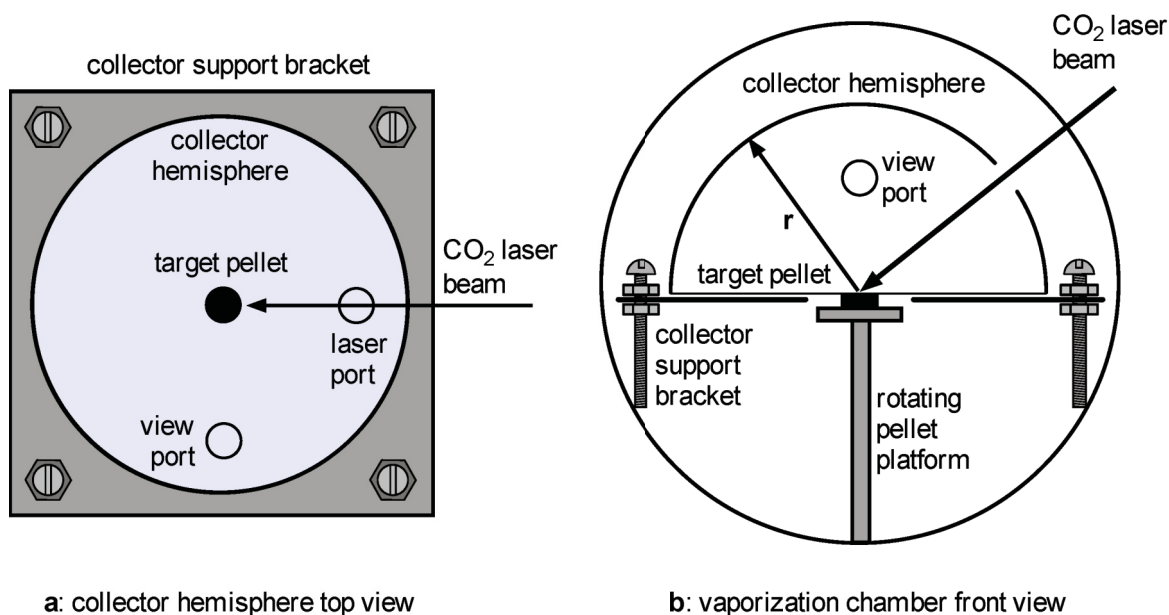


Figure 27: Details of hemispherical collector dome placement.

2.2.2 Nanoparticle Synthesis

The starting material for all nanoparticle syntheses experiments was a partially reduced titanium dioxide pellet, part number T-2051 purchased from CERAC, Inc. These pellets were assayed at 99.9% titanium oxide, rutile form. The partially reduced form of the titania (non-stoichiometric TiO_x , $x < 2$) imparted a dark blue-black coloration on the pellet surfaces. Before and after each vaporization synthesis, the target pellets were weighed to estimate the amount of material lost from the pellet during vaporization.

Following setup of the vaporization chamber and satisfactory laser optics alignment, the vaporization chamber was sealed and evacuated with the rotary vane pump to a pressure of approximately 10 Torr on the Convectron gauge. The vacuum valve was closed and the chamber was backfilled with ultra high purity (UHP) oxygen to a pressure of approximately 100 Torr. The chamber was then re-evacuated and backfilled an additional two times to remove residues of air from the apparatus. Following the third UHP oxygen flush, the chamber was evacuated and backfilled with oxygen to the required operating pressure for the nanoparticle synthesis experiment. Upon stabilization of the vaporization chamber to its operating pressure, the

vaporization laser was switched on and set to a power of approximately 30%. The target pellet was slowly rotated with the 30% beam impinging its surface for approximately two minutes to gradually anneal the surface of the pellet. Following the annealing operation, the laser power was increased to 100% and the start time for the vaporization run, in addition to the chamber pressure and laser power, were recorded.

During the laser vaporization interval, the chamber pressure was maintained by manual adjustment with introduction of additional oxygen and evacuation through the appropriate gas inlet and vacuum outlet control valves. The target pellet was manually rotated to ensure that no single region of its surface was over eroded by the laser beam. When all regions for a particular radius of the target pellet were eroded, the vaporization beam was relocated to an uneroded radius by adjustment of the laser beam steering mirrors external to the chamber.

Vaporization synthesis of titanium dioxide nanoparticles typically was conducted for one hour to ninety minutes of laser operation, dependant on the condition of the target pellet as the vaporization progressed. At the end of target vaporization, the carbon dioxide laser power was gradually reduced to zero percent and the laser was shut down. The oxygen input to the chamber for pressure maintenance was shut off and the vacuum metering valve was opened full to evacuate the chamber of any residual titanium dioxide vapor or suspended particles. Following approximately five minutes of evacuation, the vacuum metering valve was closed and the pump system powered down. The UHP oxygen was then opened to increase the chamber pressure to atmospheric so that the chamber front access door could be opened.

Following a sufficient time to allow the collector hemisphere dome to cool, the vaporization chamber front access door was fully opened and the collector removed to a clean work surface. The nanoparticle film was scraped from the interior surface of the collector dome with a plastic laboratory spatula and transferred to a tared shell vial. The masses of the vial + particles, in addition to the post vaporization mass of the target pellet were measured on a laboratory balance and recorded. Post synthesis tasks included cleanup of the vaporization

chamber with ethanol and laboratory tissue wipes, shutdown of the UHP oxygen supply cylinder, and replacement of protective covers over the vaporization laser optics.

An initial concern of the nanoparticle laser syntheses was effective control of mean particle diameter and the range of particle diameters produced for a set of operating conditions. Two approaches to affecting particle size control that were investigated. One technique was variation of the target-to-pellet distance r , (see Figure 27b) by using collector hemispheres of varying radii. The second and more successful approach investigated was nanoparticle synthesis at different oxygen pressures. The results of this work are summarized in the next chapter.

2.3 Transmission Electron Microscopy

2.3.1 Image Resolution

In 1873 Ernest Abbe described the limit of optical microscopy image resolution as approximately 200 nm (2×10^{-7} m).²⁰⁰ Two structures that are physically apart by greater than approximately one half of the lower wavelength of visible light, 400 nm, cannot be distinguished with conventional optical microscopy. The resolving power g is defined as:

$$g = 0.61 \frac{\lambda}{n \sin \alpha} \quad (67)$$

where λ is the wavelength of the light, n is the refractive index of the medium ($n=1$ for vacuum), and α is the lens acceptance half angle.²⁰¹ The 0.61 factor originates from the observation that only part of the first diffraction maximum is necessary to form a resolved image.²⁰²

Magnification that exceeds the Abbe theoretical limit became possible with the discovery of the electron and its wave-particle duality. Davisson and Germer had observed Bragg diffraction of an electron beam by a crystal of nickel in 1927 which strongly suggested that electrons could be dealt with as electromagnetic radiation.^{203, 204} Over 1925 to 1927 Hans Busch discovered that a magnetic field could be used as an electron lens in a similar manner to the function of glass lenses for light. By the close of the 1930's the light based optical microscopy resolution limit had been exceeded by researchers conducting magnification with electrons

directed in either magnetic or electrostatic electron ‘optics’.²⁰² Electron microscopy had become a viable research tool.

The de Broglie wavelength λ for an electron is calculated from the equation:

$$\lambda = \frac{h}{\rho} = \frac{h}{m_e v} \quad (68)$$

where h is the Planck constant, ρ is the electron momentum, m_e is the electron rest mass, and v is the electron velocity.⁹⁰ The velocity of an electron is determined from a classical mechanics treatment of its acceleration within an electric field. At the instant of an electron’s departure from a cathode in a vacuum, all of the particle’s energy is potential. This potential energy is the direct result of the electron’s repulsion from the negatively charged cathode and its attraction to the opposing positively charged anode. As the electron travels to the anode, it trades potential energy for kinetic energy. By the time that the electron reaches the anode its energy is completely kinetic and given by:

$$Ue = \frac{1}{2} m_e v^2 \quad (69)$$

where U is the electric field potential in volts and e is the elementary charge, previously given. Equation (69) can be rearranged to give the velocity of an electron as a function of the voltage potential through which it was accelerated:

$$v = \sqrt{\frac{2Ue}{m_e}} \quad (70)$$

Substitution of Equation (70) into Equation (68) makes the calculation of electron wavelength as a function of acceleration field voltage possible. Examples of accelerating voltages, their resulting electron wavelengths, and the corresponding image resolutions for a typical transmission electron microscope are given in Table 2:

<i>Voltage (kV)</i>	<i>Wavelength (nm)</i>	<i>Resolution (nm)</i>
20	0.0087	0.44
40	0.0061	0.31
60	0.0050	0.25
80	0.0043	0.21
100	0.0039	0.19
1000	0.00087	0.10

Table 2: Comparison of accelerating voltage, electron wavelength, and resolving power for a transmission electron microscope.²⁰¹

2.3.2 Electron Microscope Operation Modes

Conventional transmission electron microscopes can operate in two basic modes. If the electrons impinge upon the lattice planes of the specimen meet the Bragg criteria, diffraction occurs. Alternately, the electrons can pass through the sample undeflected from their original paths. Through selection of apertures and magnetic lens settings, either the transmitted electrons can be focused to form a magnified image (bright field mode) or the diffracted electrons can be focused to form a projected diffraction pattern (dark field mode).²⁰⁵ The diffraction pattern of the specimen forms at the back focal plane of the microscope objective lens and is intrinsic to the operation of the instrument, whether the application accesses the diffraction information or the bright field magnified image. The ray-trace diagrams of both modes are shown in Figure 28 for a single objective lens and schematic representations of the electron optics for a transmission electron microscope operating in both image magnification and electron diffraction modes are given in Figure 29.

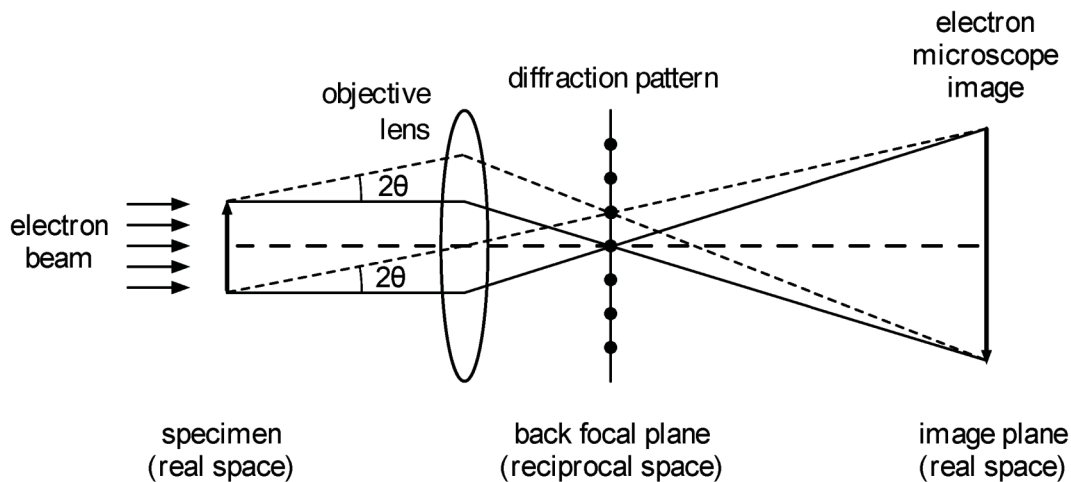


Figure 28: Electron diffraction in a transmission electron microscope.²⁰⁵ Broken lines indicate the diffracted electron beam and solid lines correspond to the transmitted electron beam. The ‘lens’ in the figure is actually a magnetic field.

Figure 28 shows the possibilities of either focusing transmitted electrons on the optical axis for a bright field image or off-axis imaging for a dark-field diffraction image. In both cases, a single focus point on the objective lens back focal plane is used to form an image. Another possibility exists where a much larger part of the back focal plane information is utilized. Through manipulation of the magnetic lens settings and Fourier transform processing of back focal plane information it is possible to greatly increase the resolution of the magnified image. High resolution transmission electron microscopy images extend magnification of the specimen to the extent that the patterns of order on the atomic scale can be discerned. These patterns are actually interference patterns between the microscope electron beam and the electron density of the specimen’s atomic structure. With high-resolution imaging techniques, detail such as lattice defects and crystal plane orientations are observable.

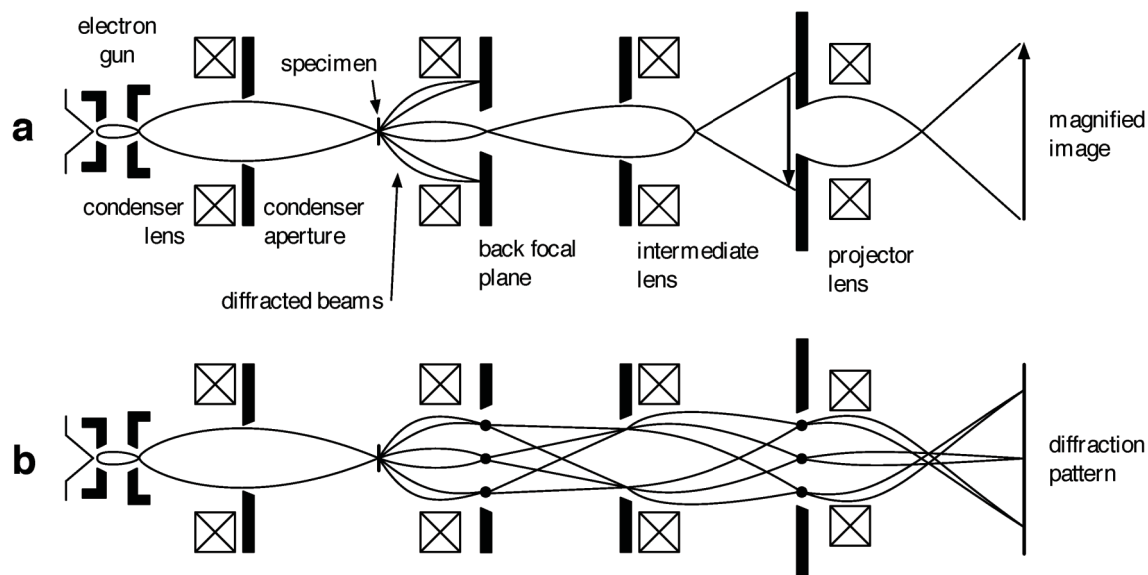


Figure 29: Diagram for electron optics of a transmission electron microscope operated in (a) magnification, and (b) electron diffraction modes. Note that the magnetic lenses are indicated by cross-hatched boxes.²⁰²

2.3.3 Nanoparticle Preparation for Electron Microscopy

My transmission electron microscopy work on titanium dioxide nanoparticles encompassed all of the imaging techniques described above. I utilized the Zeiss Model 10CA located at the Virginia-Maryland Regional College of Veterinary Medicine for diameter measurement of nanoparticles and observation of aggregation and particle morphology. The Philips EM 420 microscope presently located at the Institute for Critical Technology and Applied Science (ICTAS) was briefly used to observe electron diffraction patterns for some selected samples. Also at ICTAS, the FEI Titan 300 microscope was used for high resolution imaging of some selected nanoparticle preparations. The data collected from both the Philips EM 420 and the FEI Titan 300 were used to observe the crystallinity of the nanoparticle preparations examined.

The most common electron microscopy performed was size measurement imaging on the Zeiss 10CA microscope. Samples that were examined on this instrument were placed on electron microscopy grids. The grids that I used were a #150 copper mesh coated with a varnish support film layer, the Electron Microscopy Science's model FCF150-Cu grid.

Sample preparation for transmission electron microscopy was accomplished by dispersion of a small quantity of nanoparticles (< 0.001 g) into reagent grade 100% ethyl alcohol. The dispersions were prepared in unused 7 mL screw-cap shell vials that were rinsed with two aliquots of the dispersion solvent immediately prior to use.

Following their solvent rinses, the sample dispersion vials were completely filled with additional dispersion solvent and immediately capped pending sample introduction. Nanoparticle samples were transferred to the alcohol filled shell vials with unused, disposable glass Pasteur pipettes that had been alcohol rinsed immediately prior to use. The rinsed pipette was immediately dried with a stream of ultra high purity nitrogen and the pipette tip was then used to pick up a small quantity of nanoparticles. The particle loaded pipette tip loaded was then immediately immersed into a dispersion solvent filled shell vial, at which time the nanoparticles were rinsed from the pipette into the solvent. Following withdrawal of the glass pipette, the shell vial was capped and agitated in an ultrasonic bath for approximately thirty minutes to disperse the transferred nanoparticles.

Following ultrasonic dispersal of the nanoparticles into the ethanol, a miniature disposable polyethylene transfer pipette was used to place one drop of the alcohol nanoparticle dispersion onto an unused microscopy sample grid. The dispersion alcohol was evaporated from the sample grid within a covered Petri dish at room temperature. Following complete evaporation of dispersal solvent, the prepared microscopy grids were transferred to a storage box pending examination at one of the aforementioned electron microscopes.

2.4 X-ray Diffraction

2.4.1 The Bragg Condition

The diffraction of x-rays by crystalline material was discovered by Max von Laue in 1912 and applied to structure determination by W.H. and W.L. Bragg (father and son) in 1913.²⁰⁶ The relationship between radiation wavelength, angle of incidence to the surface of a crystal, and the spacing of atomic planes within the lattice is given by Bragg's law:

$$n\lambda = 2d \sin\theta \quad (71)$$

The parameter n is the order of reflection, or the path difference in number of wavelengths of radiation scattered by adjacent planes of lattice atoms. The scattered radiation wavelength is λ , and the distance between adjacent planes of radiation scattering lattice atoms is the parameter d . The angle θ , or the Bragg angle, describes the angle of refraction where radiation interacting with adjacent planes of lattice atoms, constructively interferes. Collectively, these parameters are referred to as the ‘Bragg condition’. The interrelation of these parameters is illustrated in Figure 30. The superficial appearance of the relationship between incident and diffracted radiation in Figure 30 strongly suggests that this phenomenon is similar to the reflection of light, although that depiction is an oversimplification. However, the similarity of Bragg diffraction to radiation reflection has become part of the terminology of this discipline and diffraction maxima are still referred to as ‘reflections’ in the literature.

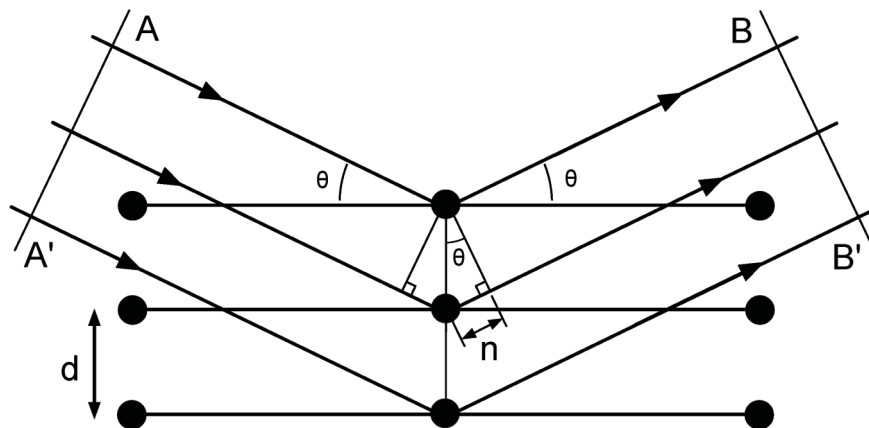


Figure 30: Bragg refraction from a crystal lattice.²⁰⁶

2.4.2 Production of X-rays

The radiation used to perform x-ray diffraction is generated by high energy electron bombardment of a metal target under vacuum conditions. Thermionic emission from a filament within the x-ray tube generates free electrons. Biasing of the filament potential with respect to the target anode to a voltage potential of approximately 10^4 volts accelerates the electrons to high

kinetic energies. These electron energies are sufficient to remove core (inner shell) electrons from within the atoms of the target metal. Transitions of electrons falling into the newly formed electron vacancies define the radiation wavelength. Figure 31 shows some of the commonly encountered transitions used in the description of x-ray radiation wavelengths.

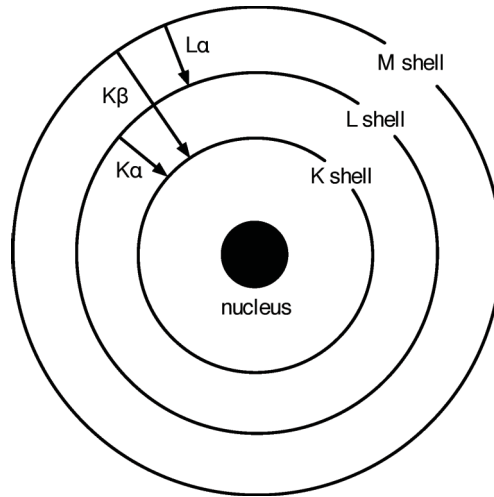


Figure 31: Electron transitions associated with some x-ray radiation sources.²⁰⁶

The presence of subshells in atomic structure leads to multiplicities of the electron transitions shown in Figure 31. For example, there might simultaneously exist a $K\alpha_1$, $K\alpha_2$, and $K\beta$ transition for a given metal. The wavelengths given for most x-ray sources used in diffraction work are usually weighted averages.

2.4.3 Powder Diffraction

The technique used for x-ray characterization of nanoparticles is powder diffraction. The x-ray beam is diffracted from multiple crystals at random orientations within the sample mount. The diffracted beams strike a detector plane, either photographic film or the path of a moving electronic detector. The random orientation of diffracting crystals causes not one diffraction spot for a characteristic set of Bragg conditions, but many. The multiplicity of diffraction spots for a unique set of conditions causes the formation of a Debye-Scherrer diffraction ring, as shown in

Figure 32. A plot of the diffraction ring intensities against their associated 2θ values produces a powder x-ray diffraction pattern.

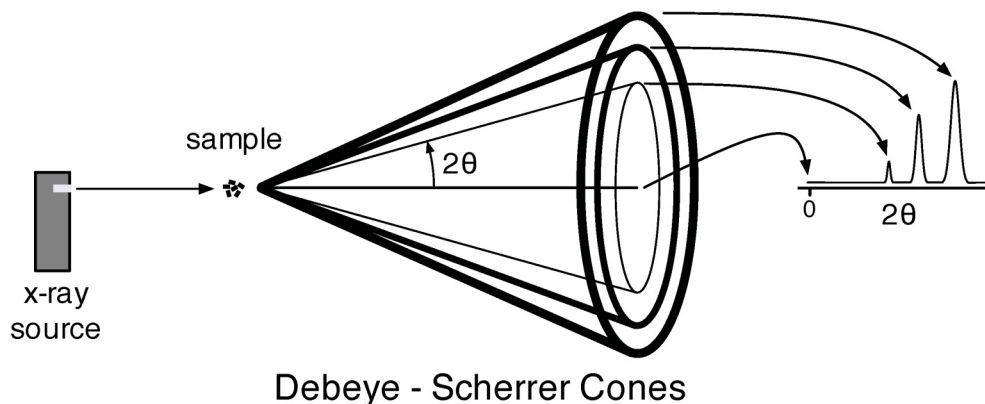


Figure 32: Powder x-ray diffraction.

2.4.4 Sample Preparation and Diffraction Pattern Collection

My x-ray diffraction characterization of titanium dioxide nanoparticles was conducted upon the Oxford Diffraction, Gemini diffractometer located in the Virginia Tech crystallography laboratory. Powder diffraction are not commonly performed on this instrument, as its main work is performed by single crystal diffraction techniques. With the small quantities of nanoparticle material available for x-ray analysis, my work had to be performed on a micro-scale.

The nanoparticle samples were packed into x-ray diffraction capillary tubes sold by the Charles Supper Company. These tubes are manufactured from silica glass in an assortment of sized ranging from 0.3 to 0.7 mm inside diameter. The procedure for loading a sample tube was to crush a small (~5 mg) portion of the nanoparticle sample with a blunt plastic probe inside a clean shell vial. This treatment was necessary to break up nanoparticle agglomerates and facilitate easier packing of the nanoparticles into the glass capillary tube. Following this treatment, the nanoparticle sample was scooped into the broad, open end of the capillary tube and packed into the opposing closed end of the tube by ultrasonic vibration. Once a column of approximately 1.5 cm of nanoparticles had been packed into the closed ent of the tube, the excess

portion of the sample tube was removed with a glass cutting tool. The open end of the tube was sealed with a small portion of bee's wax. The closed end of the packed sample tube was then fixed into a brass mounting collet sized for mounting on the Gemini diffractometer goniometer sample stage.

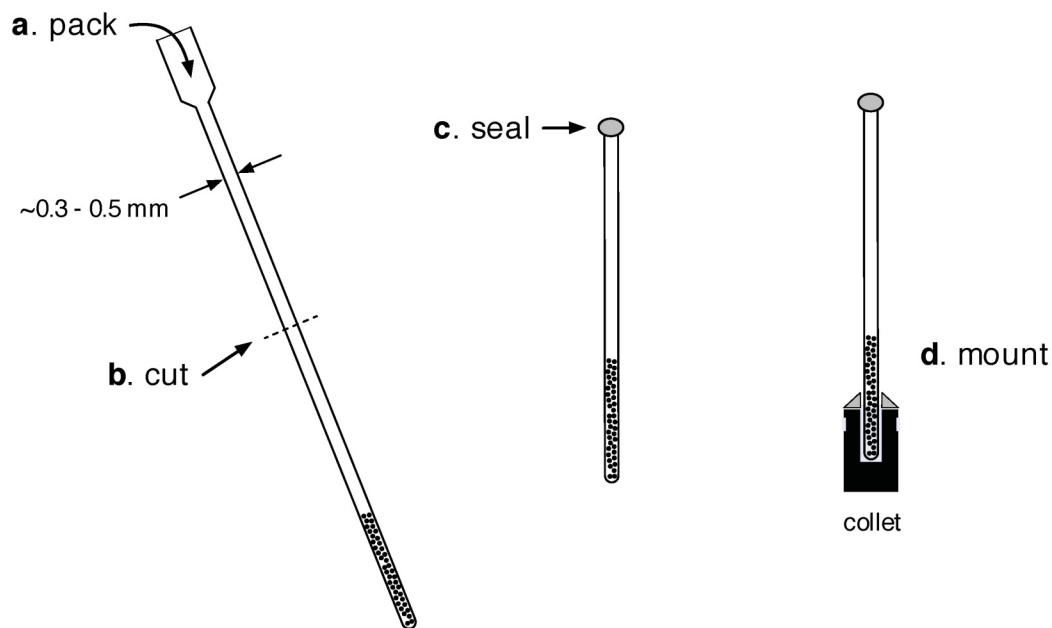


Figure 33: Gemini x-ray diffractometer powder sample tube preparation steps.

The nanoparticle diffraction patterns were collected for a range of 2θ angles from five to sixty degrees. The radiation wavelength was set to the copper $K\alpha$ emission line. Diffractometer control and data acquisition was managed through Oxford Diffraction's CrysAlis Professional software. The diffraction data files generated were written in an ASCII text format, and the diffraction data they contained were examined with data plotting software.

2.5 Infrared Observation of Electron Transitions

2.5.1 Fourier Transform IR Spectroscopy

Mid-infrared spectroscopy over the region of wavelengths spanning 2.5 to $25 \mu\text{m}$ ($2.5 \sim 25 \times 10^{-6} \text{ m}$) is most commonly used for the identification of chemical bonds. For a bond to

absorb energy in this region of the electromagnetic spectrum, it must have a dipole moment. The absorbance of infrared radiation results in an oscillatory change in the bond geometry as its dipole moment is changed. These bond geometry changes are observed as bond stretching, bending, or scissoring movements.

Infrared spectra are most commonly presented as energy absorbance over a frequency domain. Because of the large frequencies associated with micron wavelength radiation (approaching hundreds of GHz), infrared spectra have historically been presented with frequency units of wavenumbers, whose units are cm^{-1} .

Infrared spectroscopy is an energy dispersive technique. Prior to the availability of inexpensive microcomputers, infrared energy dispersion for spectroscopy was most commonly accomplished through sequential scanning of wavelengths with a ruled diffraction grating or prism based monochromator. This approach generally required the spectroscopist to make compromises between scanning speed and quality of spectral resolution. Faster scanning of wavelengths was accomplished by loss of fine spectral detail. The time requirements of this sequential scanning approach also made it impractical for applications such as reaction intermediate observation or kinetic studies.

The replacement of a grating based monochromator in the spectrometer with an interferometer accomplishes a significant improvement in spectrum acquisition speed. An example of one common design, the 1891 Michelson interferometer, is shown in Figure 34.

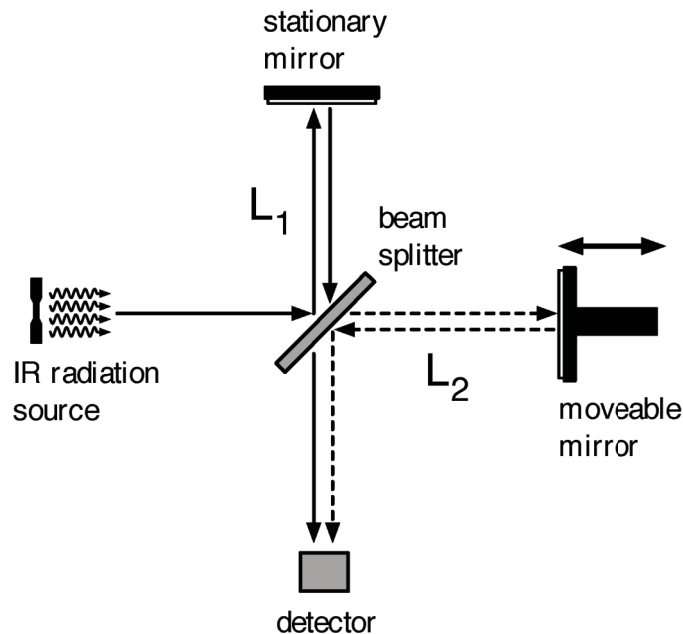


Figure 34: The Michelson interferometer. Note that the compensating plate has been omitted from the stationary mirror path L_1 for clarity. The location of a sample for spectrometry would be in the recombined beam prior to the detector.¹⁸⁴

The interferometer operates by splitting light from a common source into two beams of approximately equal intensity. This optical division is accomplished through the use of a partially reflective mirror, known as a beam splitter. Each of the two beams is directed over a separate optical path and then recombined immediately prior to detection. In Figure 34 those separate paths are designated L_1 and L_2 . By alteration of one optical path's length (L_2) through the use of a moving mirror, constructive and destructive interferences are caused within the recombined L_1 and L_2 beams. For a monochromatic, i.e. single wavelength, radiation source the output of the interferometer detector is modulated by the varying extent and type of L_1 and L_2 interference in the recombined beam, as the mobile mirror is linearly translated. The resultant detector output is an oscillating cosine waveform of single frequency.

Spectroscopy usually requires a continuous broadband radiation source and the result of scanning the interferometer mirror displacement in this case is a superposition of many cosine waves, each waveform having a different frequency. This superposition results in secondary interferences and the creation of beat frequency overtones. Consequently, the interferometer

detector output for a broadband source is a complex signal whose intensity varies as a function of mirror spatial displacement. This pattern is known as an interferogram. The general equation for the spatial domain interferogram is:

$$I(\delta) = \int_0^{\infty} B(\tilde{\nu}) \cos 2\pi\tilde{\nu}\delta d\tilde{\nu} \quad (72)$$

where $I(\delta)$ is the signal intensity as a function of mirror displacement δ , and $B(\tilde{\nu})$ is the spectral absorbance as a function of wavenumber frequency $\tilde{\nu}$.¹⁸⁴ The $I(\delta)$ term is the interferogram and the $B(\tilde{\nu})$ term is the frequency domain spectrum contained within it.

In order to extract a frequency domain spectrum from an interferogram, Fourier transform techniques are applied to Equation (72). The result of this transformation is the equation:

$$B(\tilde{\nu}) = 2 \int_0^{\infty} I(\delta) \cos 2\pi\tilde{\nu}\delta d\delta \quad (73)$$

This equation represents the frequency domain spectrum that was acquired through interferometry. Obviously, a physical instrument cannot make infinite mirror translations so a compromise is necessary. Scanning of the mobile mirror in a spectrometer is typically limited to several hundred to a few thousand translations, and a numerical approximation (i.e. fast Fourier transform or similar techniques) of Equation (73) is applied through software. Execution of these actions result in an absorbance infrared spectrum of comparable quality to a sequential scan, but only requiring a fraction of the time required for the latter.

Irradiation of a sample with a broadband infrared radiation signal and application of interferometry techniques gives Fourier transform infrared (FTIR) spectroscopy the multiplex, or Fellgett advantage over monochromator scanning. The entire spectrum is acquired in a parallel fashion where all radiation frequencies and their associated sample absorbances are acquired simultaneously. This efficiency gain is the basis for the FTIR scan speed advantage over monochromator based designs.

The benefits of high speed in spectroscopy include avoidance of changing conditions in the instrument or sample altering the spectrum during its acquisition. Rapid acquisition of spectra also open the opportunity to accumulate multiple spectra which can be averaged or added to increase the signal-to-noise ratio of the data. Fast spectroscopy also makes possible the observation of transient chemical species over time in a changing reaction environment, making transition state intermediate species and kinetic studies possible.

2.5.2 The Vacuum FTIR Cell

The high surface area of titanium dioxide nanoparticles, ranging from 10 to 100 m² • g⁻¹, add significant difficulty to spectroscopic studies. Nanoparticles rapidly adsorb materials from the air, even at low concentration. This capacity for gas adsorption is one of the strongest incentives for interest in their application to heterogeneous catalysis. Hydrocarbon adsorbates will oxidize on the surface of the particles, possibly removing oxygen from the nanoparticle crystalline lattice and reducing the titanium cations remaining. The electronegativity of oxygen in water adsorbates will depress electron population in the conduction band, as will molecular oxygen adsorbates. Clearly, any attempt at spectroscopic observation of electron behavior within titanium dioxide nanoparticles requires a controlled, adsorbate free nanoparticle environment. The vacuum FTIR cell provides that control.

The vacuum cell apparatus we use for nanoparticle FTIR studies was designed and built at the University of Pittsburgh for the research group of Professor John Yates. A schematic of the cell, in cut away profile, is given in Figure 35. The FTIR high vacuum cell is built upon a cubical stainless steel box, equipped with vacuum flange openings. On opposing sides of the cell are potassium bromide IR windows and on the front face of the cell is a third optical port (not shown in Figure 35) equipped with a sapphire window. This third port is used as a light injection window for conducting ultraviolet irradiation experiments. The top of the cell is extended approximately 25 cm with a pair of stainless steel flange/pipe assemblies. Within this cylindrical extension are electrical vacuum pass-through seals for supplying power and thermocouple connections to the nanoparticle stage inside the cell.

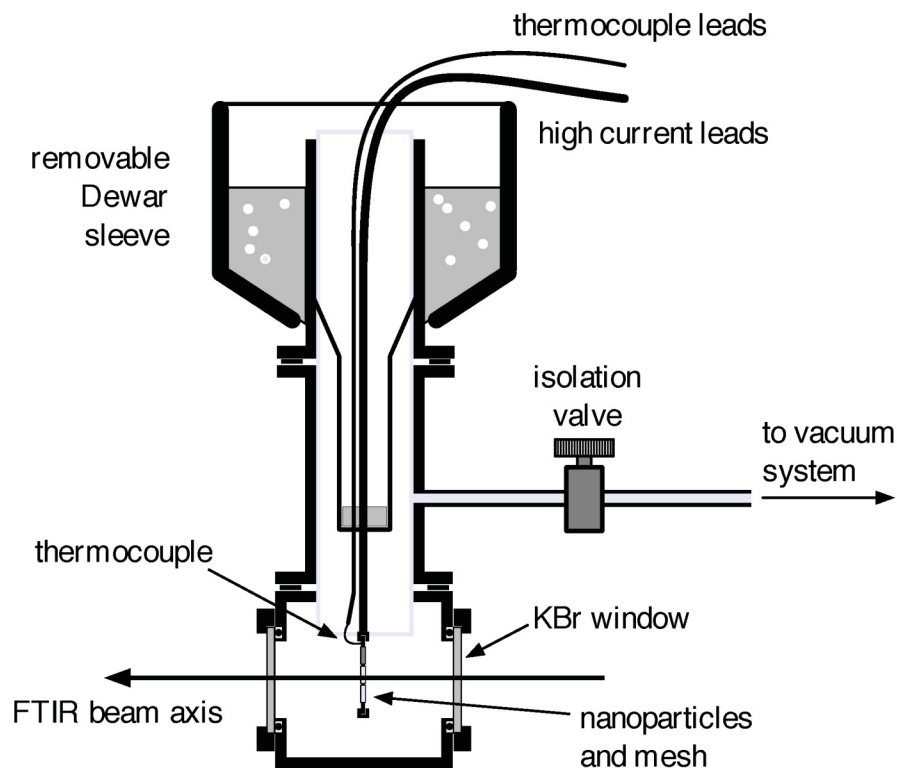


Figure 35: FTIR high vacuum cell. Front port for ultraviolet irradiation omitted for clarity.

The FTIR vacuum cell can accept a Dewar sleeve on the upper cylindrical extension for liquid nitrogen cryogenic cooling. This procedure is performed for trapping of trace water onto the upper walls of the cell during nanoparticle cleaning and conditioning procedures, in advance of making experimental observations under dehydroxylated conditions.

The vacuum cell is attached with a flexible metal line to a gas manifold that is used for evacuating the cell, monitoring its pressure, and allowing the controlled introduction of gases at low partial pressure for surface adsorption studies. Vacuum pumping is accomplished with a Pfeiffer Vacuum $60 \text{ L}\cdot\text{s}^{-1}$ turbomolecular pump and a Varian $20 \text{ L}\cdot\text{s}^{-1}$ ion pump in tandem. Normal operating pressure for the FTIR vacuum cell is 1×10^{-8} Torr.

The FTIR vacuum cell is mounted in the beam path of a Mattson Instruments, Inc. Model RS-10000 Fourier transform infrared spectrometer, as shown in Figure 36. This spectrometer is equipped with a cryogenically cooled mercury-cadmium-tellurium (MCT) infrared detector.

FTIR control and data acquisition is managed through a serial interface connection to a desktop computer running Mattson WinFirst[®] spectroscopy software. The vacuum cell is attached to the spectrometer sample compartment with two electromechanical, stepping motor actuators for vertical and horizontal positioning. The spectrometer optics windows within its sample compartment are adapted with polymer rings that are used to secure a nitrile sleeve, gas-tight connection between the FTIR and the vacuum cell windows (indicated as **a** and **b** in Figure 36). Both polymer rings are equipped with side tubing connections for a dry nitrogen gas purge. These flexible nitrile purged tunnels minimize or eliminate atmospheric moisture contributions to the IR spectrum background without interfering with cell translation.

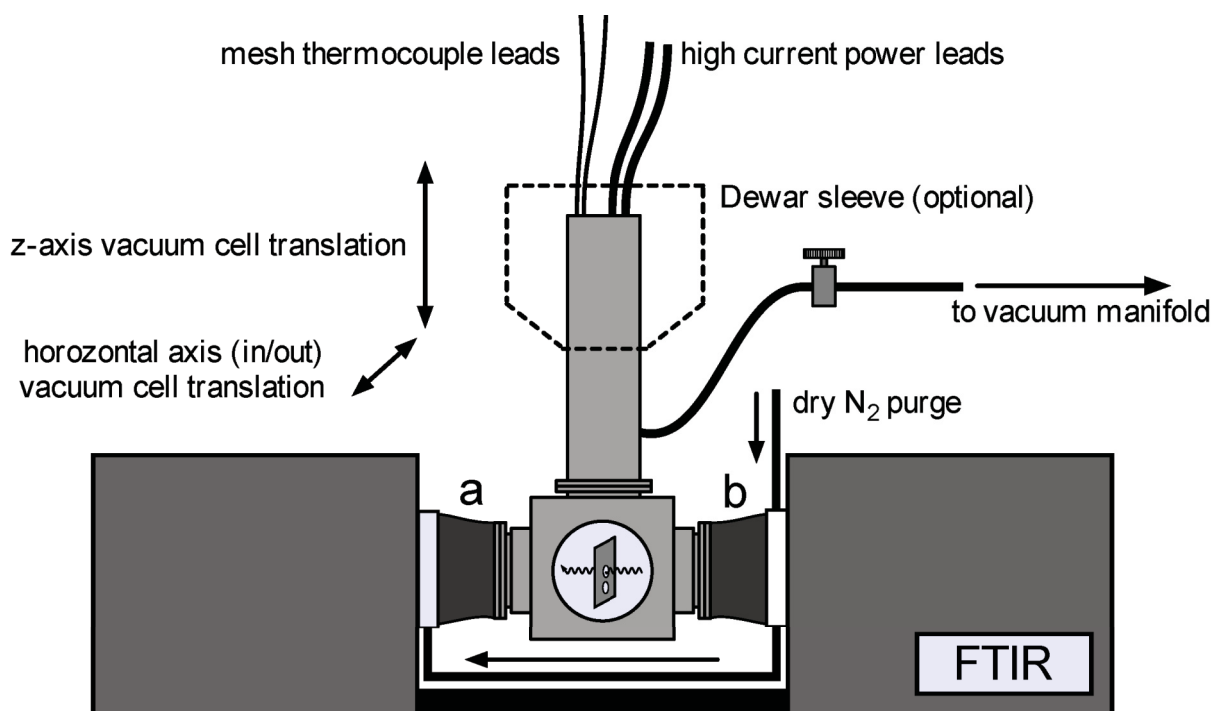


Figure 36: Vacuum cell installed onto Mattson RS-10000 FTIR spectrometer.

The fixture for mounting of nanoparticle samples, positioned within the vacuum cell, consists of two nickel clamps that are attached by large diameter wiring to an external high-current power supply. These clamps are used to hold a piece of electrochemically etched tungsten mesh in the optical path of the FTIR and provide electrical connection of opposing

edges of the mesh to the power supply circuit. This tungsten mesh, purchased from the Bukbee-Meyers Co., is formed by etching a repeating pattern of square holes (0.3 mm x 0.3 mm) into a thin sheet of rolled tungsten. Under magnification the resulting etched mesh resembles window screen material and the mesh is approximately 80% transparent to light. Details of the clamp assembly are shown in Figure 37.

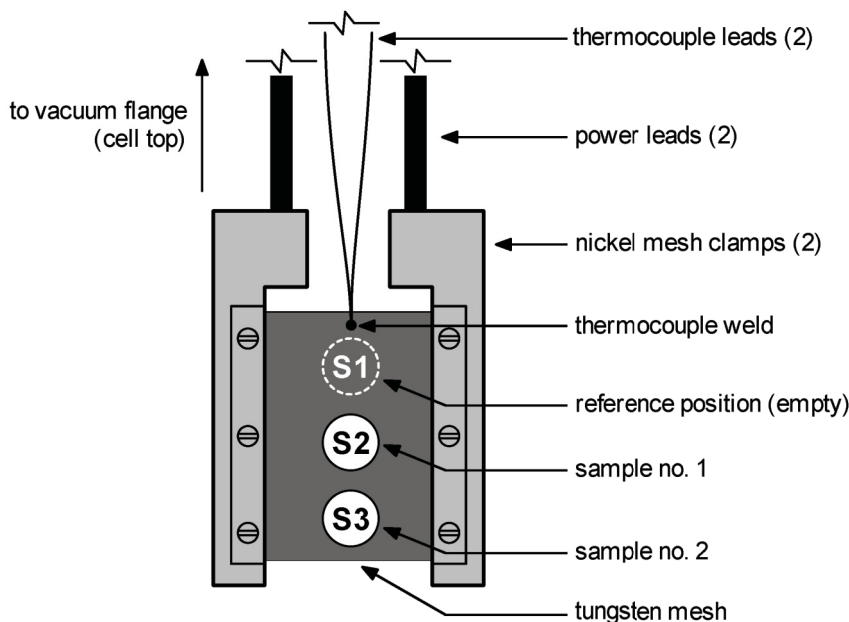


Figure 37: Tungsten mesh nanoparticle stage assembly.

In addition to its optical transparency, tungsten mesh is utilized as a mounting media for nanoparticles in the IR cell because of its electrical qualities. Tungsten is more resistive than copper (5.39×10^{-8} versus $1.71 \times 10^{-8} \Omega \cdot \text{m}$ at 298 K)³ which causes the mesh to resistively heat during the passage of electrical current. By varying the current applied to the mesh, the temperature of the tungsten mesh and the nanoparticle samples pressed into its orifices can be controlled to within $\pm 1\text{K}$.

The temperature of the heated tungsten mesh and the nanoparticles pressed into it is monitored and controlled through the use of a type K thermocouple welded onto the mesh. The

thermocouple junction is prepared by welding an approximately six inch length of 0.002 inch O.D. alumel wire to a six inch length of 0.002 inch O.D. chromel wire at a single location. The junction is then spot welded directly to a position on the tungsten mesh above the S1 reference position as indicated in Figure 37. The thermocouple signal is passed out of the cell through vacuum tight electrical feed-through connections. The temperature signal is read on a proportion-integral-derivative (PID) controller which regulates the supply of heating current to the tungsten mesh and maintains the mesh at a setpoint temperature. The temperature setpoint is ramped by either a manual control setting or use of a programmable voltage ramp generator.

The tungsten mesh fixture within vacuum FTIR cell has three sample positions. The top location, indicated in Figure 37 by a broken line circle, is typically left empty. An infrared spectrum of this bare tungsten mesh location is recorded at the beginning of an experiment and used to background correct the nanoparticle spectra. When a new mesh-nanoparticle assembly is loaded into the vacuum cell, the electromechanical actuators for the cell mount are slewed through a range of horizontal and vertical positions for each nanoparticle sample location on the tungsten mesh while the peak-to-peak voltage of the FTIR interferogram is monitored for a maximum reading. The nanoparticle sample location on the mesh where the interferogram voltage difference maximizes is the location of maximum optical density for that sample. These optical density maxima for both samples S1 and S2 in Figure 37 are the locations where infrared spectra are taken during experimental observations, as these are the sites where sample path length is assumed to be greatest. Through entry of the numerical coordinates for both of these absorbance maxima into the actuator control computer, the vacuum cell can be quickly repositioned to either sample location during an experiment.

2.5.3 Sample Preparation and Conditioning

A new piece of tungsten mesh is cut to size with fine scissors using either a paper template or a previously used mesh as a guide. Holes are located and punched into the mesh for mounting on the vacuum cell nickel clamps. Once the mesh is cut to size, it is cleaned by ultrasonic agitation in a beaker of reagent grade methyl alcohol for thirty minutes, followed by

another thirty minutes in a beaker of reagent grade acetone. Following the second solvent cleaning, the mesh is allowed to air dry while loosely wrapped in laboratory tissue wipes.

Prior to loading nanoparticle samples onto the mesh, a temperature monitoring thermocouple must be fabricated and attached directly to the mesh. Two pieces, each approximately six inches in length, of 0.002 inch O.D. chromel and alumel wire are joined with a resistance spot weld, leaving a one-half inch length of each wire extending beyond the weld joint. These short extensions of thermocouple wires are threaded into two adjacent holes in the tungsten mesh at a location just below the point of attachment for the thermocouple to the mesh surface. The electrodes of the resistance welding tool are then used to press the thermocouple junction against the tungsten mesh surface and the junction is spot welded onto the mesh. Following attachment of the thermocouple, excess wire threaded through the mesh is trimmed and the response of the thermocouple is checked with a digital multimeter. If the thermocouple shows a voltage response with temperature change, the mesh is ready for nanoparticle sample loading.

The tungsten mesh and attached thermocouple are placed within a custom press mold assembly, shown in Figure 38. With the mesh correctly positioned, the top half of the mold is secured with machine screws. A 5 mg portion of each nanoparticle sample is loaded into its position (S2 or S3 in Figure 38) and the piston is seated in the mold above the loose nanoparticles. The mold and piston are then placed on a hydraulic press and the piston is compressed at 13 kpsi ($1.3 \times 10^4 \text{ lb}\cdot\text{in}^{-2}$) for two minutes. Following nanoparticle loading of the tungsten mesh sample positions, the top half of the mold is removed and the mesh is mounted on the vacuum cell nickel clamps.

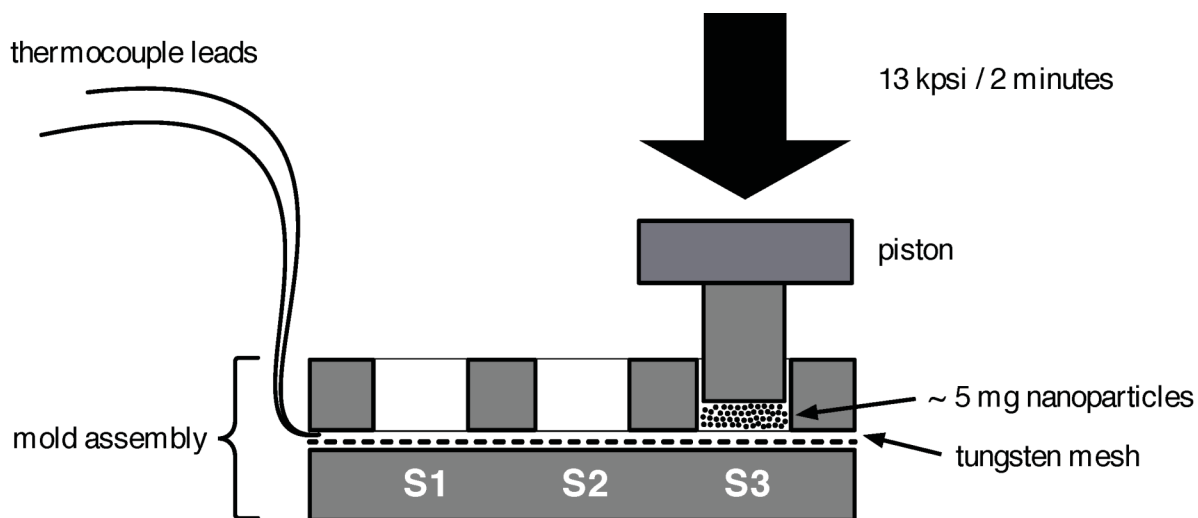


Figure 38: Nanoparticle press mold assembly.

Following placement of the tungsten mesh and nanoparticles into the vacuum cell, the cell is temporarily wrapped with laboratory resistive heating tapes and attached to the aforementioned FTIR vacuum system. The cell is heated to approximately 100 °C and evacuated with the turbomolecular pump for approximately twelve to twenty-four hours for water removal.

After the initial evacuation of the vacuum cell, the nanoparticles are subjected to oxygen treatments for the oxidative removal of adsorbed organic materials. The heat tape is removed and the vacuum cell is reinstalled into the FTIR sample compartment. Vacuum pumping of the cell is continued and the mesh is resistively heated to 675 K over four hours. The vacuum pumping is discontinued and the cell is pressurized to 20 Torr with oxygen while resistive mesh heating is continued at 675 K for an additional hour. Following the first oxygen treatment, the vacuum cell is pumped to 1×10^{-6} Torr. The cell is once again pressurized to 20 Torr with oxygen and allowed to continue heating at 675 K for an additional 30 minutes. Following this second oxygen treatment the cell is pumped back to 1×10^{-6} Torr and allowed to cool to room temperature. The effect of these treatments is to remove water and hydrocarbon adsorbates from the nanoparticles.

2.5.4 Temperature Ramp Infrared Spectra Collection

Thermal ramping of the titanium dioxide nanoparticles within the FTIR vacuum chamber is ordinarily performed to either observe the condition of the nanoparticle samples following adsorption studies or to remove water residues from the particles. The vacuum cell is not continually pumped when it is not in use, but rather an isolation valve on the line from the cell to the vacuum manifold is closed. This mode of idling the apparatus avoids the necessity of continual operation of the turbomolecular and ion pumps. However, even when the cell is under active vacuum pumping, a slow ingress of water into the system from the outside environment is unavoidable. The large surface area of the nanoparticle samples within the vacuum cell capture and accumulate water from this continual flux of low level water leakage. A technique has been developed to dehydroxylate the nanoparticle surfaces for sufficient intervals that permit spectroscopic experiments over several hours under nearly water-free conditions.

A Dewar vessel was designed (see Figure 35 and Figure 36) to fit over the cylindrical extension of the vacuum cell body. This insulated vessel seals against the stainless steel body of the cell. During its use the Dewar sleeve is filled with a coolant, usually liquid nitrogen. Once cooled to ~ 77 K by the liquid nitrogen, the upper regions of the vacuum cell become a water trapping surface. The nanoparticle samples temperature is then resistively heated to approximately 400 K while the FTIR cell is evacuated and the cryogenic water trapping Dewar sleeve is in place. The trace level of adsorbed water on the nanoparticle surfaces is thermally desorbed by resistive heating and upon contact with the cryogenically cooled vacuum cell wall, the vapor condenses and is trapped as ice. Following this treatment, the nanoparticles exist in a highly dehydroxylated state.

Temperature ramping experiments of the FTIR vacuum chamber are generally conducted under automated control. Initially a spectrum is taken of the 'bare' tungsten mesh S1 region (see Figure 37 and Figure 38) at ambient temperature (298 K). This spectrum is used for background subtraction from the subsequent spectra. This background subtraction is intended to remove spectral contributions of the tungsten and tungsten oxide from the titanium dioxide nanoparticle

spectra. The high-current power supply PID controller setpoint is then switched over to automatic ramping from an external voltage ramp circuit. As the setpoint voltage is increased by the external voltage ramp generator, the electric current passing through the tungsten mesh is increased by the PID controller and resistive heating of nanoparticle samples increases. Temperature read-back from the tungsten mesh thermocouple is displayed on the PID controller unit and is recorded manually, concurrent with spectra acquisition by the FTIR data system. Spectral data files are recorded in comma separated value (CSV) ASCII text files.

Chapter 3: Data Analysis

3.1 Electron Microscopy Particle Diameter Measurements

The chemical reactivity and physical properties of nanoparticles are size dependent. These effects make accurate measurement of nanoparticle size and morphology an important part of characterization. I chose transmission electron microscopy (TEM) for these measurements because it offered a relatively simple, inexpensive, and direct method of obtaining this data.

All nanoparticle diameter data was obtained from the Zeiss 10CA transmission electron microscope at the Virginia-Maryland Regional Veterinary School. This instrument produces a computer graphics file that the user copies and examines offline. The file format is the tagged image file format (TIFF) which can be opened and manipulated by most graphics editing programs. Each file that this microscope generates includes an image scale bar which can be used to calibrate image processing software.

Nanoparticle diameter measurements are made from the TIFF files with the ImageJ software package²⁰⁷, distributed by the National Institute of Health. Prior to making particle diameter measurements, the software is calibrated by drawing a measurement line along the length of the TEM image calibration bar. The length of the calibration bar and its measurement units are then entered into the program. Following this image scale calibration of the software, all measurements made for that TIFF file produce calibrated results.

Particle diameter measurements are accomplished in ImageJ by drawing a line with a computer mouse cursor across the particle followed by execution of the 'Measure' command. This command causes the software to calculate the particle diameter in the units previously calibrated from the TIFF image calibration bar, and append the result to an ANSII text file of measurement results. Because the TEM images commonly contain hundreds to thousands of nanoparticle features, I wrote a macro in ImageJ that executed the 'measure' command from a keystroke, and then uniquely labeled the measured particle diameter to avoid double

measurements of particles within an image. At the conclusion of diameter measurements for a TIFF file, the file was saved with an appended file name for archival purposes and the diameter measurements text file was saved for subsequent processing.

While TEM was likely the most accurate method of obtaining nanoparticle diameters, the images were usually not completely accessible for diameter measurements. Particle agglomeration, particularly for smaller diameter nanoparticles, lead to opaque aggregates of material with largely obscured particle boundaries. In these cases, diameter measurements were made for particles on the periphery of the aggregates, where particle boundaries were more clearly defined. In spite of this limitation of some images, it was still common to obtain 50~200 measurements from a single TIFF file. A summary table of particle diameter measurements and particle synthesis conditions is included in Appendix 5, Table 6 on page 127.

Control of nanoparticle size and size distribution is a concern common to most researchers working with these materials. The laser vaporization technique that I used offered two possible approaches to particle diameter control.

The first method of diameter control attempted was control of the linear distance from the precursor material pellet undergoing vaporization to the nanoparticle collector surface. Following some initial experimentation with sheet stainless steel collector surfaces that were arranged in a semi-cylindrical geometry, a hemispherical geometry was selected for collector surfaces. A hemisphere provides a symmetrical geometry and an equal path length from the precursor pellet located at its center to the collector surface.

Two experiments were performed with stainless steel collector hemispheres of different radii (2.3 and 6.3 cm). Nanoparticles were prepared with both hemispheres under identical vaporization conditions (37 Torr O₂, 100% laser power, 1 hour vaporization time). The results of these experiments are summarized in Appendix 5, Table 6 for the SPB014 and SPB015 nanoparticle batches. Although the larger collector radius (6.3 cm) produced a 1 nm larger mean particle diameter, the $\pm 3 \sim 4$ nm error in the diameter measurements for these batches makes any conclusion that path distance significantly influenced their size questionable.

The second approach to influencing nanoparticle size was vaporization chamber pressure control. For these experiments, also summarized in Table 6, a hemispherical stainless steel collector surface of 4.4 cm radius was used. Following three cycles of evacuation and ultra high-purity (UHP) oxygen flushing, the vaporization chamber was backfilled with UHP oxygen and held at pressures varying from 1 to 500 Torr for each experiment. In all experiments, the laser was operated at 100% power output (60 Watts) and vaporization was performed for one hour. The data from these experiments are plotted in Figure 39.

While no strongly correlated statistical trend is demonstrated from the plot in Figure 39, the data does appear to support the generalization that higher chamber pressures lead to larger nanoparticle diameters. Another effect that appears to increase with chamber pressure is the distribution of particle diameters produced. Higher pressure (500 Torr) growth appears to nearly approximate a bimodal particle size distribution, as is demonstrated by the error bars and TEM micrograph insets of Figure 39. Nanoparticles produced at low pressure (5 Torr) appear, in comparison, to approach monodisperse characteristics.

These pressure-size effects can be explained by a decrease in mean free path for particles of material vaporized from the precursor pellet, as chamber pressure is increased. As the chamber pressure is increased the frequency of particle-particle and particle-oxygen molecule collisions are also increased. This higher collision frequency causes an increasingly Boltzmann-like distribution of nanoparticle velocities. The slower particles experience more collisions and grow to larger sizes before they impact the collector surface. Also, a stationary large diameter particle on the collector surface continues to offer a larger target for collisions with gaseous material, so some extent of size-skewed particle growth might continue.

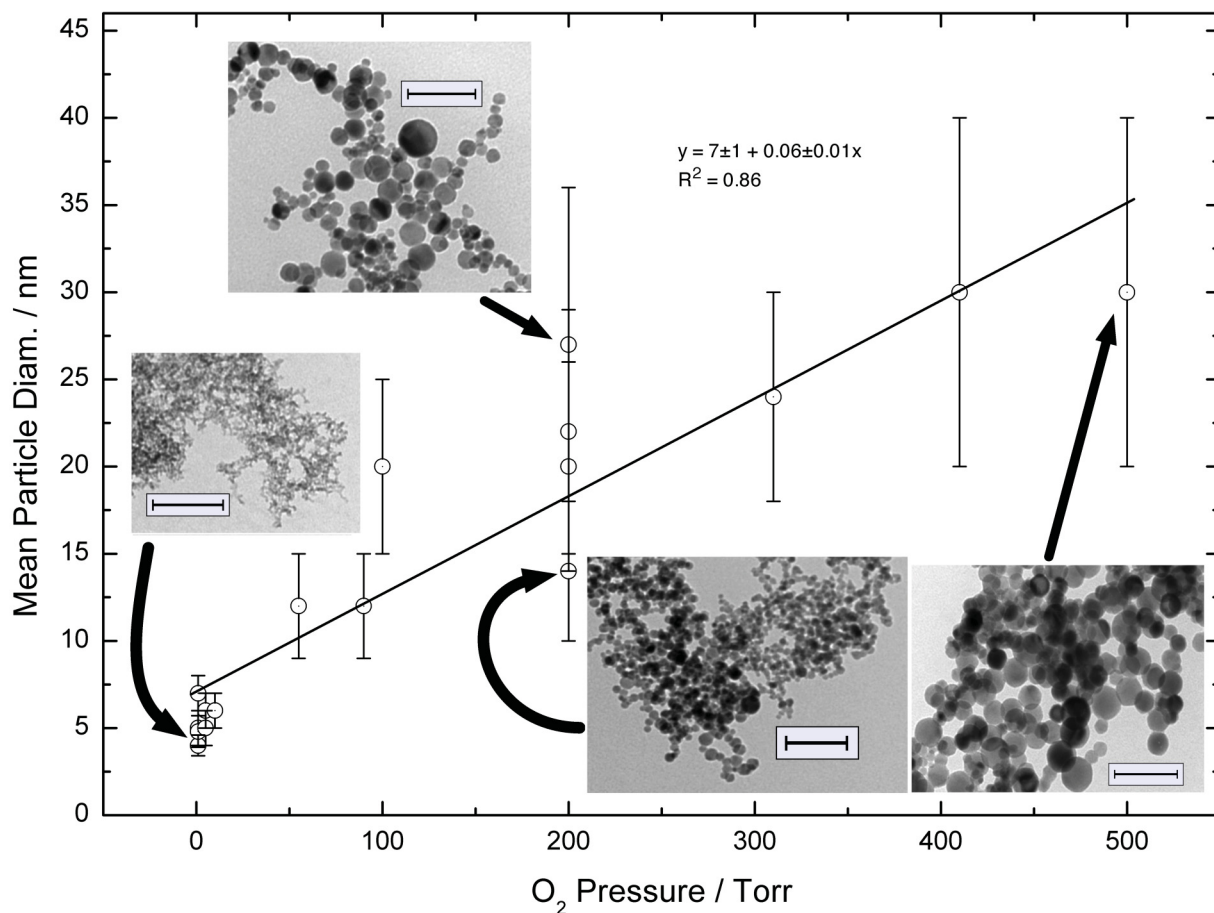


Figure 39 : Nanoparticle mean diameter as a function of laser vaporization chamber O₂ pressure. Data given in Appendix 5, Table 6. The scale bars on the inset micrographs all indicate a 100 nm dimension.

My calculations of titanium dioxide nanoparticle shallow trap state energies were obtained from two nanoparticle synthesis batches, SPB018 (4.0 ± 0.6 nm mean diameter) and SPB020 (30 ± 10 nm mean diameter). The diameter measurements data for these batches are included in Appendix 5, Table 6. TEM micrographs and particle size histograms are presented in Appendices 7 and 8 on pages 128 and 129. A high resolution TEM image from the Titan 300 microscope at the Virginia Tech Institute for Critical Technology and Applied Science (ICTAS) is presented in Appendix 8 on page 130.

3.2 Powder X-ray Diffraction

Powder x-ray diffraction (XRD) patterns of nanoparticles are used for identification of phase composition within the particles, i.e. confirmation of the presence of the rutile and/or anatase polymorphs and their relative amounts. Nanoparticle mean diameter can be indirectly obtained from XRD through the use of the Scherrer equation:

$$PW_{\frac{1}{2}} = \frac{0.94\lambda}{L\cos\theta} \quad (74)$$

where $PW_{1/2}$ is the reflection peak width at half height, λ is the x-ray radiation wavelength, and θ is the Bragg angle of incidence.^{208, 209} The particle diameter is the variable L .

Another motive for collection of XRD patterns for nanoparticles is confirmation of nanoparticle crystallinity. Crystallinity is less of a concern for laser vaporization particle synthesis as it is for sol-gel precipitation techniques, as the former technique provides its own heat treatment to crystallize condensed material.

My powder XRD analyses were performed on particles held within glass capillary tubes. Although glass is an amorphous material, it still contributes a broad x-ray diffraction peak and all of my XRD patterns are superimposed upon this background contribution. Figure 40 is an XRD pattern from an empty 0.3 mm I.D. sample capillary.

The use of pattern subtraction was attempted for removal of the sample tube background contribution to the XRD pattern. Differences in tube orientation with respect to the x-ray beam and variations in tube diameter made subtraction of a ‘blank’ from an empty capillary from a diffraction pattern lead to negative peak deflections. The chance of inducing artificial features to the XRD pattern or removing useful information led to my decision to refrain from using this type of background subtraction.

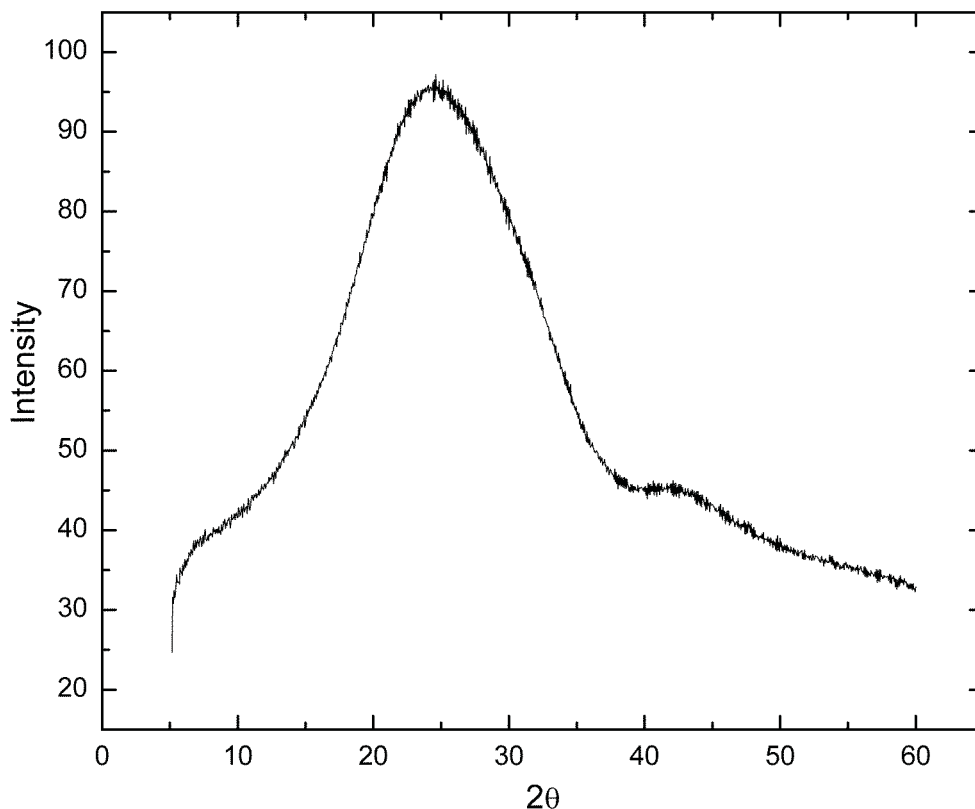


Figure 40: X-ray diffraction pattern for an empty, 0.3 mm ID sample capillary.

Another intriguing approach to removal of the silica background was a data processing treatment based on the work of Sonneveld and Visser.²¹⁰ I wrote a computer program that applied their baseline isolation algorithm for subtraction of silica contributions to the XRD patterns. The algorithm (and my program) required a user input for the number of baseline smoothing cycles applied to the extracted background. My work with this program showed that the excessive use of this baseline smoothing could potentially remove some useful XRD pattern information, but an example of the results of Sonneveld-Visser baseline correction is included in Figure 41.

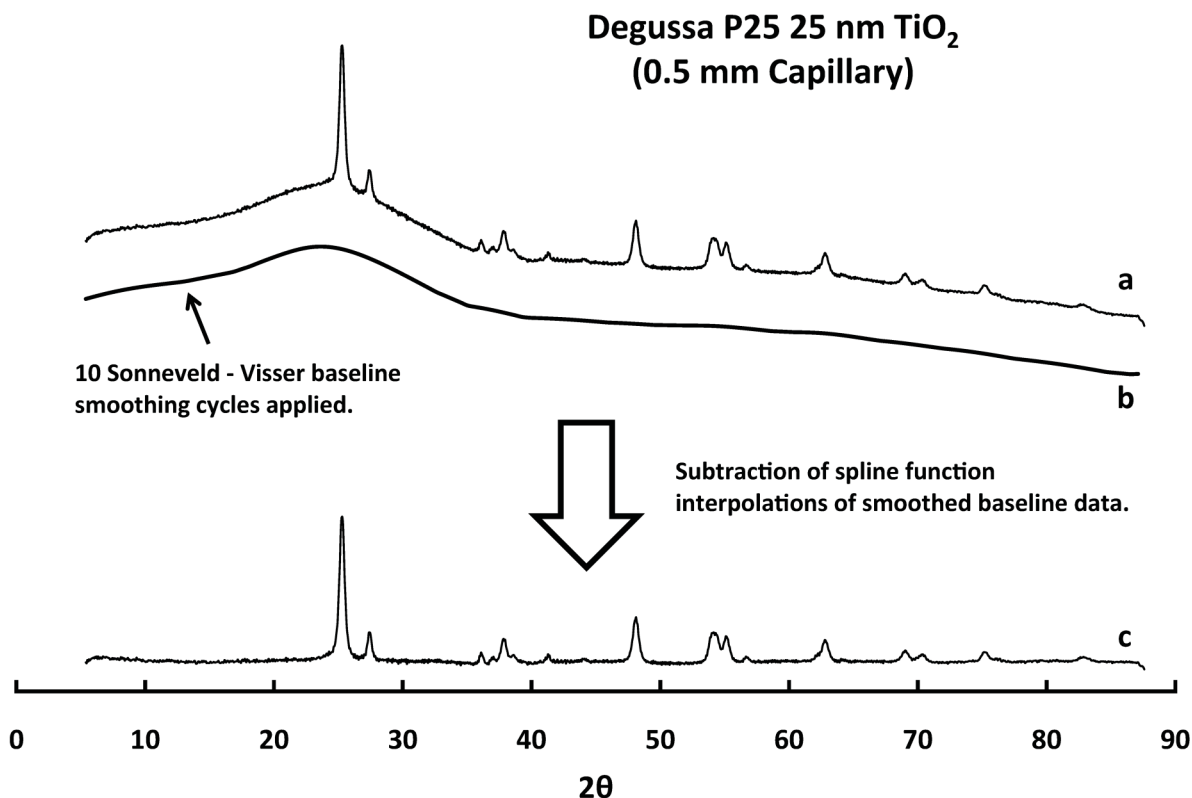


Figure 41: Degussa P25 titanium dioxide nanoparticle XRD pattern with Sonneveld - Visser baseline correction. Pattern (a) is the uncorrected data, (b) is the extracted and smoothed baseline, and (c) is the baseline corrected XRD pattern.

XRD characterization of nanoparticles was limited to the Degussa P25 titanium dioxide, SPB018 (4.0 ± 0.6 nm mean diameter) and the SPB041 nanoparticle synthesis batches. In the case of SPB041 electron microscopy characterization has not yet been performed, but its synthesis conditions (100 Torr O₂, 4.4 cm collector radius) are consistent with nanoparticles in the 10 ~ 20 nm diameter range. The Figure 42b XRD pattern for SPB041 is consistent with a mean particle diameter at the upper end of the 10 ~ 20 nm range, as is apparent when comparing the pattern to Figure 42a for Degussa P25 which has a mean particle diameter of 25 nm.

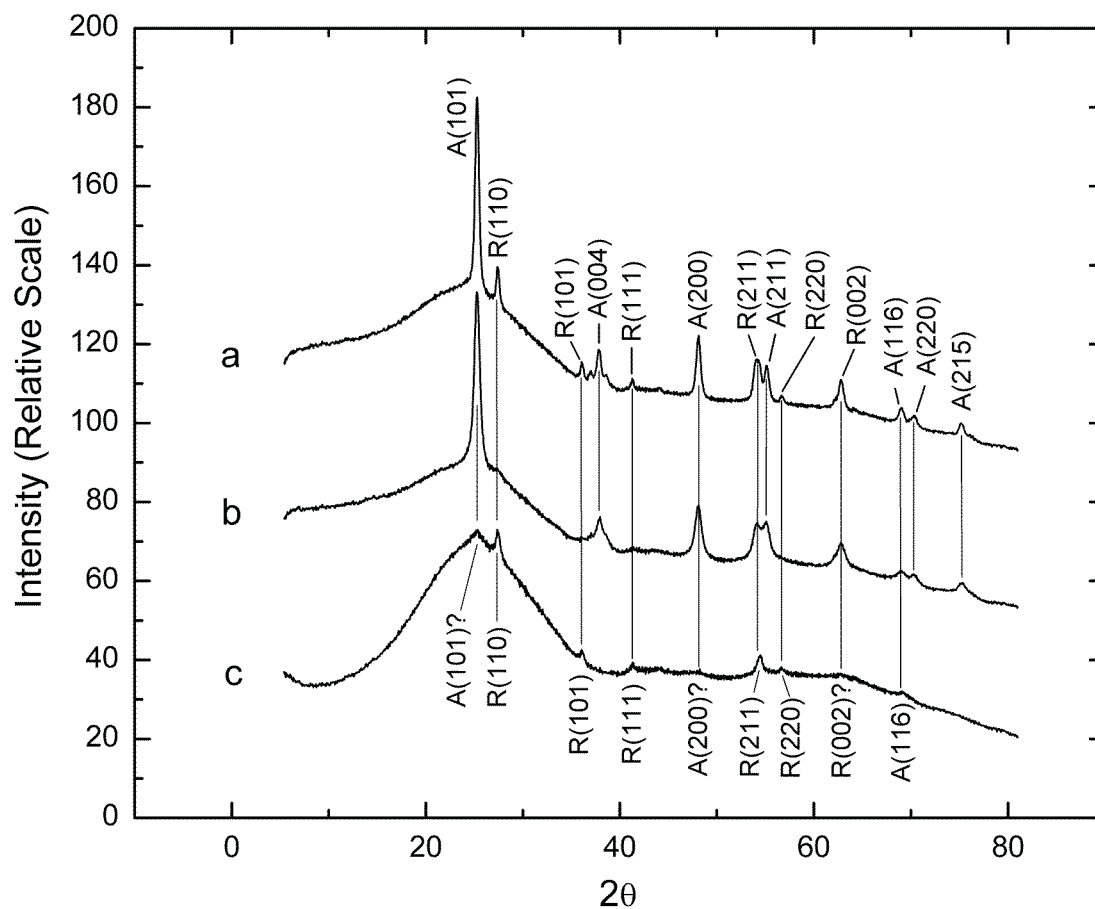


Figure 42: X-ray diffraction nanoparticle characterization. Patterns are for (a) Degussa P25, (b) SPB041, and (c) SPB018 titanium dioxide. Reflections identified with '?' are tentative.

The XRD pattern reflection assignments are based on the work of Zhou et al.²¹¹, where Degussa P25 was characterized. The patterns in Figure 42 were offset from each other for clarity in the pattern plot, but no other modification of the data has been performed. It is interesting to note that for Figure 42c, from the 4.0 ± 0.6 nm diameter particles, the dominant titanium dioxide polymorph appears to be rutile, with very little or no anatase present in the pattern. This outcome would seem to be in conflict with the earlier observation that anatase is the thermodynamically favored polymorph for particle diameters below 14 nm.⁸¹⁻⁸³ This phenomena might be a characteristic of particles made by laser vaporization synthesis, and it merits further investigation.

3.3 FTIR Data Processing and Shallow Trap Energy Calculation

My calculation of titanium dioxide nanoparticle shallow trap state energy is based upon a mathematical treatment of infrared spectra. Conduction band electron population effects on the infrared spectrum baseline are observed over all infrared frequencies between 4000 to 1000 cm^{-1} . Although the temperature ramp spectra were recorded under vacuum, spectral absorbances from residual water on the nanoparticles in the vacuum cell is still observed. For this reason I decided to use a region of the infrared spectrum from 2600 to 1900 cm^{-1} for my calculations. This region is isolated from hydrogen bonded OH absorbance over 3700 to 2600 cm^{-1} and water H-O-H bending modes at 1650 cm^{-1} .

The Mattson WinFirst spectroscopy software saves infrared spectra as space-delimited ASCII text files. Each file contains several hundred data points, and collectively there were approximately one hundred or more files to examine. My approach was to write a computer program in G77 FORTRAN (WaveShave.f, Appendix 3) which used a text file list of data files to direct sequential processing of spectra. Each data file on the list was opened and read by WaveShave.f and rewritten as a second text file which only contained spectral data points between my predefined range of infrared frequencies, 2600 to 1900 cm^{-1} . When the file processing run was complete, a new set of truncated infrared spectrum data files had been created.

The association of infrared spectrum baseline area given in Equations (63) to (66) with the Fermi-Dirac behavior of conduction band electrons requires an integrated area under the spectrum baseline for each truncated spectrum file produced by data processing with WaveShave.f. I wrote a second G77 FORTRAN program (TrapInt2.f, Appendix 4) which was adopted from a program given in Nyhoff and Leestma's *FORTRAN 77 for Engineers and Scientists*.²¹² My program applied trapezoidal numerical integration to the truncated spectra baselines previously generated by WaveShave.f. Trapezoidal integration is based upon the approximation:

$$\int_a^b f(x) dx \approx \frac{\Delta x}{2} [f(x_0) + 2f(x_1) + 2f(x_2) + \dots + 2f(x_{n-1}) + f(x_n)] \quad (75)$$

where $\Delta x = (b - a) / n$ and $x_i = a + i\Delta x$.²¹³ The variables a and b were the starting and ending frequencies of the truncated spectrum, n was the number of data points contained within the data file, and Δx was the spacing between absorbance data points within the file. Like WaveShave.f, the program TrapInt2.f uses an ASCII text file containing a list of data files (those previously generated by WaveShave.f) to direct processing. The integration results from the batch processing are written to a single ASCII text file as a summary of data file names and their associated integration result.

Following integration of the truncated FTIR spectra, a curve fit to the Fermi-Dirac relation previously given in Equation (64) was necessary (see page 61). The baseline integration areas were matched to their associated sample temperatures and these data were fit to the Fermi-Dirac relation using a non-linear least squares technique described by Brown.^{214, 215} This curve fit technique is performed with a spreadsheet constructed in Microsoft Excel[®]. Reiterative processing of the data set within the spreadsheet is accomplished with the Solver[®] application that is included with the spreadsheet program. The variables of the regression are the integrated baseline area Z and the nanoparticle temperature T . The regression parameters are the proportionality constant D and the shallow trap energy state E_{state} . An example of my spreadsheet constructions is shown in Figure 43.

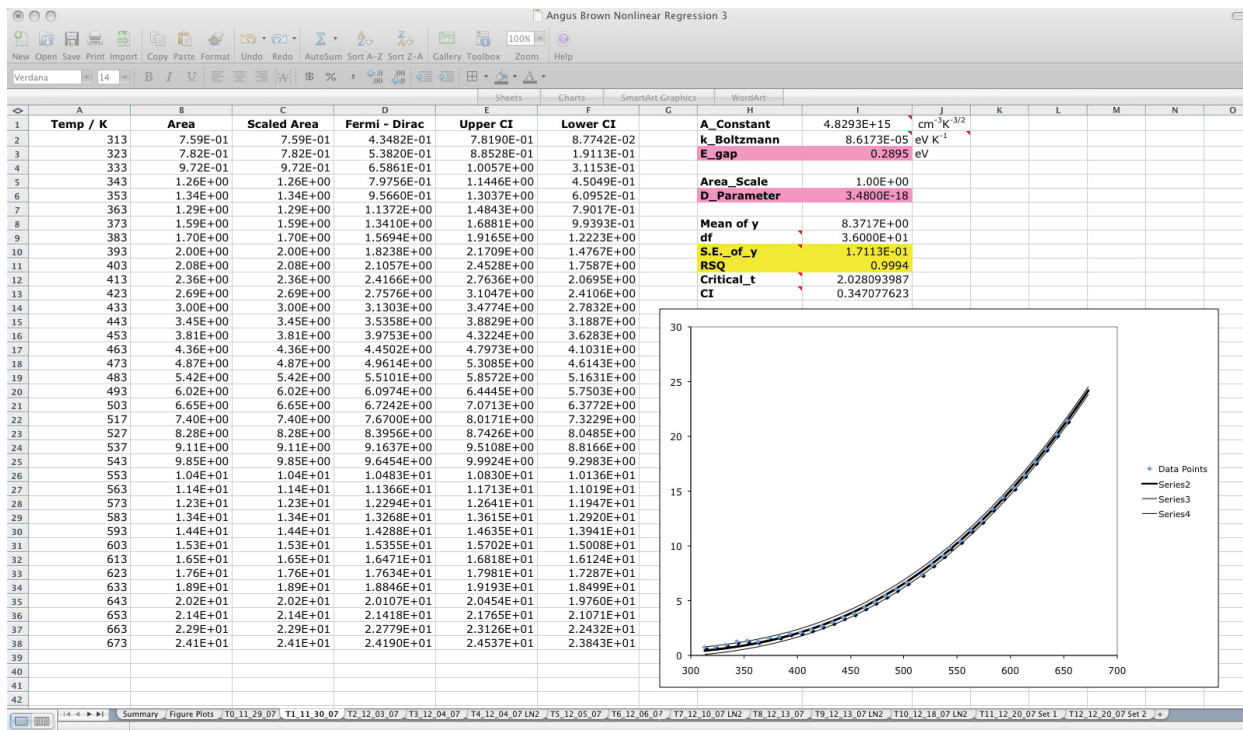


Figure 43: Nonlinear regression curve fit spreadsheet for the Fermi-Dirac relationship.

Brown’s approach is to use Solver[®] to iteratively adjust the fit parameters specified by the user while simultaneously seeking to maximize coefficient of determination, RSQ in Figure 43. For perfect correlation of the independent and dependent variables (T and Z in my work) RSQ would be one. A summary of the regression results for the SPB018 (4.0 ± 0.6 nm) nanoparticles is given in Table 3 and for the SPB020 (30 ± 10 nm) nanoparticles in Table 4. Plots of the regression data sets and their fitted Fermi – Dirac trend lines are provided in Figure 44.

<i>Regression Parameters</i>			
<i>Data Set</i>	<i>D</i> (A.U. • cm ² • n _e)	<i>E_{STATE}</i> (eV)	<i>RSQ</i>
11/30/07	3.48 × 10 ⁻¹⁸	0.290	0.999
12/03/07	3.10 × 10 ⁻¹⁸	0.277	0.996
12/04/07	1.22 × 10 ⁻¹⁷	0.457	0.993
12/10/07	5.01 × 10 ⁻¹⁸	0.302	0.992
12/20/07	7.14 × 10 ⁻¹⁸	0.377	0.997
<i>Mean (eV):</i>		0.34	
<i>Standard Deviation (eV):</i>		0.08	

Table 3: Fermi - Dirac regression results for SPB018 (4.0 ± 0.6 nm) TiO₂ nanoparticles.

<i>Regression Parameters</i>			
<i>Data Set</i>	<i>D</i> (A.U. • cm ² • n _e)	<i>E_{STATE}</i> (eV)	<i>RSQ</i>
12/05/07	9.84 × 10 ⁻¹⁸	0.398	0.992
12/06/07	2.98 × 10 ⁻¹⁸	0.259	0.976
12/18/07	2.65 × 10 ⁻¹⁸	0.207	0.998
<i>Mean (eV):</i>		0.3	
<i>Standard Deviation (eV):</i>		0.1	

Table 4: Fermi - Dirac regression results for SPB020 (30 ± 10 nm) TiO₂ nanoparticles.

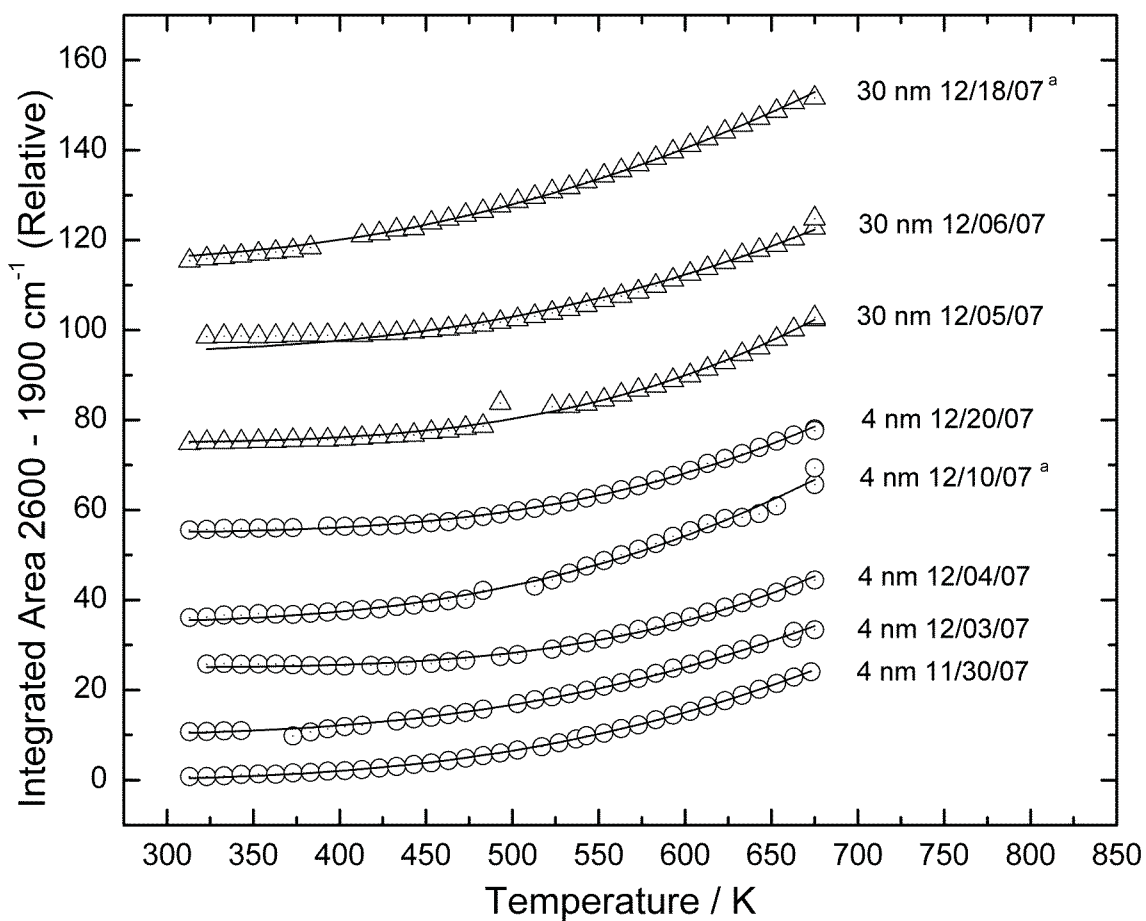


Figure 44: Integrated area vs. temperature plots for 4 nm (circle symbols) and 30 nm (triangle symbols) TiO₂. Trend lines are fitted Fermi – Dirac relation. Data sets designated with (a) were collected with cryogenic water trapping.

Chapter 4: Discussion of Results and Conclusions

4.1 Review of Research Objectives

Titanium dioxide nanoparticles catalyze oxidation-reduction chemistry by using external energy inputs (heat or electromagnetic radiation) to promote electron transport between the particle surface and adsorbates. This catalytic cycle is initiated by excitation of electrons to the titania conduction band, causing the migration of both electrons and electron vacancies (i.e. ‘holes’) to the particle surface. Thermal excitation of electrons provides an alternative to high-intensity ultraviolet irradiation of nanoparticles for promotion of adsorbate reaction catalysis. The electrons entering the titania conduction band as the result of thermal excitation originate from structural defects in the titanium dioxide crystal lattice structure that are collectively named shallow trap states. Characterization of the energy requirements for thermal excitation of electrons from these shallow trap states is important to understanding and optimizing titanium dioxide nanoparticle catalysis. My work sought to determine the shallow trap state energies for titanium dioxide nanoparticles that were formed through laser vaporization-condensation synthesis techniques. My measurement of shallow trap state energies was accomplished through collection of transmission infrared spectra of the nanoparticles over temperatures spanning 298 to 675 K, followed by evaluation of the spectroscopic data with an expression derived from Fermi-Dirac electron theory.

4.2 Nanoparticle Sizes and Size Distributions

One early idea for directing the size of titanium dioxide nanoparticles produced from laser vaporization was to vary the radial distance from the precursor material pellet to the collector surface. By increasing the volume in which accreting particles could undergo collisions with gaseous titanium dioxide species, it was hoped that larger particles could be generated.

Two hemispherical steel collector surfaces were prepared with radii of 2.3 and 6.3 cm. The 4.0 cm difference in radii correspond to a volume difference of approximately 500 cm³. Nanoparticle batches were prepared with each collector at a chamber pressure of 37 Torr. The

particle diameter data for these batches, SPB014 and SPB015 in Table 6 on page 127, suggests that reducing the collector volume by approximately one-half liter had negligible effect on the nanoparticle mean diameter. The difference in diameters between these batches was approximately 8%. Electron micrographs for both batches are presented in Figure 45.

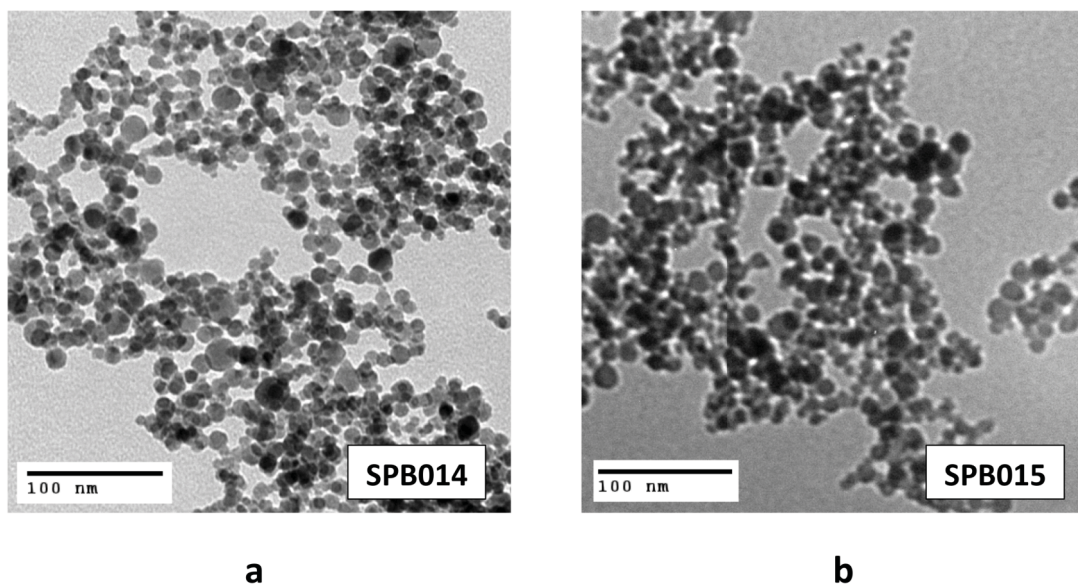


Figure 45: Transmission electron micrographs for SPB014 and SPB015 titanium dioxide nanoparticle batches. The precursor pellet to collector surface distance was (a) 6.3 cm and (b) 2.3 cm. Both syntheses conducted at 37 Torr O₂ chamber pressure.

The effect of pressure manipulation on nanoparticle mean diameter is much easier to discern. While the data in Table 6 for nanoparticle syntheses with the 4.4 cm radius collector at different pressures is not well correlated ($R^2 = 0.86$ in Figure 39), there is a monotonic increase in particle diameter with increasing vaporization chamber pressure. There also is a trend of increasing particle size distribution (note the increasing standard deviations with pressure in Table 6).

As the chamber pressure increases, the mean free path of the gaseous species within the chamber reduces. Atkins and de Paula note that mean free path reduces by one-half for each doubling of pressure.⁹⁰ For the Table 6 data vaporization experiments were performed at pressures between 1 and 500 Torr O₂. The difference in these pressures represents

approximately nine doublings of pressure. The corresponding nine reductions of the mean free path by factors of one-half would have a cumulative effect of a 2×10^{-3} reduction. This magnitude of mean free path reduction translates into greatly increased collision frequency between accreting nanoparticles and gaseous material from the liquefied precursor pellet.

Increased collisions in the gas phase from increased chamber pressure also provide a greater opportunity for Maxwell-Boltzmann statistics to broaden the distribution of particle diameters. The gaseous species within the vaporization chamber partitions in a Boltzmann distribution at any of the pressures used for nanoparticle synthesis. At higher pressures, with increased collision frequency, that distribution of energies is imparted upon the accreting particles. The result is that the particles acquire a Boltzmann distribution of energies which affects their number of collisions. For example, a particle impacted by more high kinetic energy particles will itself acquire a higher kinetic energy than an identical particle that experienced fewer high energy impacts. The distribution of nanoparticle speeds leads to a distribution of growth rates that broaden the nanoparticle size distribution. This effect appears to be directly proportional to the vaporization chamber pressure.

4.3 Shallow Trap State Energy Measurements

The Fermi-Dirac regression results for 4 nm and 30 nm particles were considered separately in Table 3 and Table 4 respectively, on page 101. Chestnoy et al.²¹⁶ observed that when the diameter of 3 nm cadmium sulfide nanoparticles approached the diameter of their shallow trap states, strong mixing of the trap state and the conduction band wavefunctions occur. This mixing suggests that there may be a size effect on the shallow trap state energies observed for particles of greatly different size. My observations do not indicate a size effect on shallow trap state energies. The mean E_{STATE} values in Table 3 and Table 4 are essentially the same (0.34 ± 0.08 and 0.3 ± 0.1 eV respectively). However, it may be inappropriate to consider this comparison as a test of size effects on shallow trap state energies, as the larger particles represented in Table 4 had a much larger distribution of diameters than the particles in Table 3.

Shallow trap state energies reported by different researchers for titanium dioxide span the range of 0.1 to 1.1 eV.^{99, 100, 217-221} The techniques used to make these measurements included thermoluminescence and diffuse reflectance spectroscopy, as well as electrochemistry and purely theoretical, computer simulation. My 0.3 ~ 0.34 eV range of values from infrared spectroscopy compare favorably with some of these literature values that are presented in Table 5.

<i>Researcher</i>	<i>Shallow Trap State Gap,-s (eV)</i>
Ghosh et al. ⁹⁹	0.27, 0.28, 0.32, 0.39, 0.48, 0.56, 0.60, 0.62, 0.76, 0.87
Frindell et al. ²¹⁷	0.1 ~ 0.6
Lagemaat et al. ¹⁰⁰	0.4 ^a
Szczepankiewicz et al. ²¹⁸	0.42
Valentin et al. ²¹⁹	0.9, 1.1
Warren et al. ²²⁰	0.1
Peter et al. ²²¹	0.1 ~ 0.25

Table 5: Survey of reported values for titanium dioxide shallow trap state energy gap, relative to bottom edge of conduction band. (a) indicates a calculated value.

The placement of the shallow trap state energy within the context of other features of the titanium dioxide energy band diagram is shown in Figure 46. As previously noted in Table 1 on page 30, the gap separating the bottom of the conduction band and the top of the valence band is approximately 3.0 eV. The Fermi-Dirac expression presented in Equation (64) that relates the integrated infrared baseline area to conduction band electron density was derived with an assumption that the E variable in the exponential term represents the electron trap energy closest to the conduction band, i.e. a shallow trap state. The energy difference between the conduction band and this shallow trap state is also indicated in Figure 46. Other features noted in this figure

are the vacuum energy level energy (E_{vacuum}) for titania, i.e. the energy at which an electron is completely removed from the semiconductor, and the Fermi energy (E_{Fermi}).

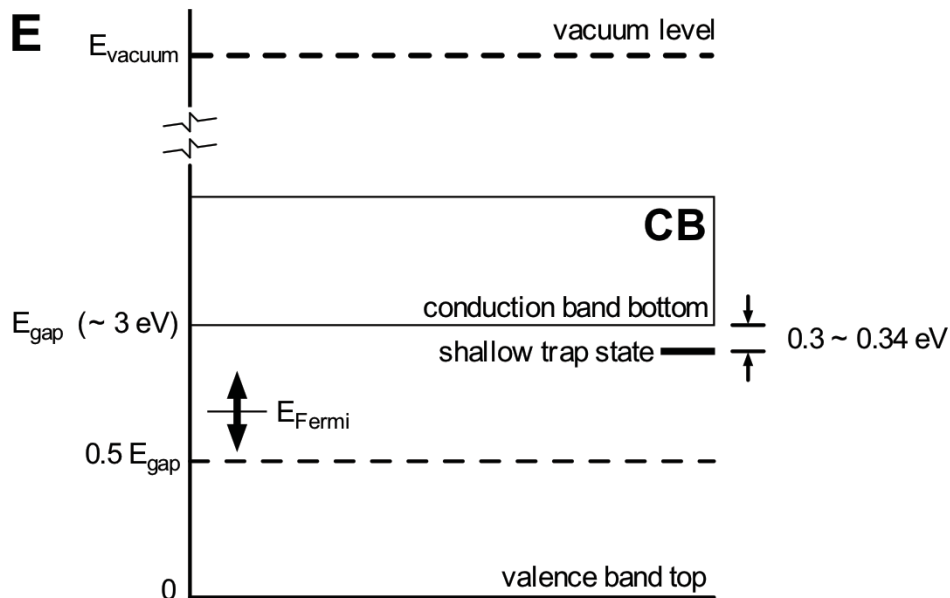


Figure 46: The shallow trap state energy difference of titanium dioxide relative to the band structure.

Accurate placement of the Fermi energy for a semiconductor nanoparticle such as titanium dioxide is difficult. Experimental approaches to measuring Fermi energy have included electron spectroscopy techniques⁹⁸ and observation of electric current–voltage behavior at a junction between semiconductors of known and unknown Fermi energies.²²² Hayes and Stoneham noted that for a pure, undoped semiconductor the Fermi energy is located in the middle of the band gap, but when dopants are introduced the Fermi level is increased above the midpoint of the gap.²²³ Göpel et al. placed the Fermi level less than 1 eV below the conduction band.⁹⁸ Given that electron trap state populations within the band gap are variable, location of the Fermi energy for a nanoparticle without direct measurement is limited to estimates.

4.4 Estimation of Electron Shallow Traps Population

Titanium cations are the most likely locale of titanium dioxide nanoparticle shallow electron traps. While electron micrographs such as Figure 45 on page 104, Appendix 6 Figure

50 on page 128, and Appendix 7 Figure 51 on page 129 give the appearance that nanoparticles are smooth spheres, at the atomic scale the surface of the particle contains numerous steps and corners where titanium cations are incompletely coordinated with oxygen anions. This particle surface atomic ‘roughness’ is discernable in the high resolution transmission electron micrograph shown in Appendix 8 Figure 52. Larger particles containing multiple titania polymorph phases may have grain boundaries that also can contribute irregularities in cation coordination leading to electron trapping.²²⁴ Coordinate unsaturated cations at the particle surface are particularly susceptible to capture of electrons from adsorbates, with a reduction of oxidation state from Ti^{4+} to Ti^{3+} . Loss of oxygen from titanium dioxide with an accompanying formation of Ti^{3+} as shown in Figure 15 on page 35 is also more likely to occur at the particle surface. Also, Lagemaat et al. noted that lattice defect electron trap sites are presumed to be located on the surfaces of nanoparticles because of their high surface-to-volume ratio.¹⁰⁰

An attempt to estimate the number of shallow trap sites could begin with the Equation (64) Fermi-Dirac expression. While this expression gave estimates of the shallow trap energy level that were in reasonable agreement with the work of other researchers, as shown in Table 5, closer examination of Equation (64) does not offer a means to mathematically estimate the total number of trap sites present on a titania nanoparticle particle.

Consider the example of a 4 nm diameter titania particle that is composed entirely of the rutile polymorph (density = $0.235 \text{ g} \cdot \text{cm}^{-3}$)⁸⁴. Evaluation of Equation (61) for $E_{\text{state}} = 0.3 \text{ eV}$ at a temperature of 298 K indicates that approximately 1.69×10^{16} electrons are excited into the conduction band for one gram of nanoparticles (See Appendix 9 on page 131). Implicit in this example is the assumption that the number of electrons entering the conduction band equals the number of electron-donor shallow trap sites. The Fermi-Dirac trends in Figure 44 demonstrate a correlation between nanoparticle temperature and FTIR integrated baseline area. This increase in integrated FTIR baseline area is an indication of increased conduction band electron population. If evaluation of Equation (61) is repeated under similar constraints, with the nanoparticle temperature changed to 675 K, the new conduction band electron population is

approximately 1.51×10^{18} electrons per gram of rutile nanoparticles.. If the number of electrons in the conduction band is equal or proportional to the number of shallow trap sites, there should exist a temperature for Equation (61) where a maximum conduction band electron population occurs. The number of conduction band electrons at this temperature could serve as an estimate of the number of electron trap states. This maxima should be accessible through evaluation of the roots of a first-order derivative of Equation (61).

The first-order derivative of Equation (61) with respect to the independent temperature variable is:

$$\frac{dN_{CB}(T)}{dT} = \left(\frac{B}{2T^{1/2}} \right) (2CE_{State} + 3T) \text{Exp} \left(-\frac{CE_{State}}{T} \right) \quad (76)$$

where B and C are aggregate constants, E_{state} is the shallow trap state energy, and T is the thermodynamic temperature. The first multiplied term of Equation (76) and the right-most exponential term can only reach a zero value at an infinite temperature, as shown in Equations (77) and (78). The remaining middle term of Equation (76) achieves a zero value at a negative thermodynamic temperature value, which has no physical meaning, as shown in Equation (80). These results exclude a purely analytical solution to estimation of shallow trap population from the Equation (61) Fermi-Dirac expression.

$$\frac{B}{2T^{1/2}} \rightarrow 0 \Big|_{T \rightarrow \infty} \quad (77)$$

$$\text{Exp} \left(-\frac{CE_{State}}{T} \right) \rightarrow 0 \Big|_{T \rightarrow \infty} \quad (78)$$

$$2CE_{State} + 3T = 0 \quad (79)$$

$$T = -\frac{2}{3}CE_{State} \quad (80)$$

It is intuitive that a nanoparticle has a finite number of shallow state trapped electrons. An experimental determination of the number of trap states from recording additional infrared spectra at temperatures above 675 K may not succeed at determination of an electron thermal excitation maximum. Excessive heating of titania nanoparticles will lead to the creation of additional oxygen vacancies with creation of new trap sites. Annealing of titanium dioxide will alter the polymorph composition of mixed phase nanoparticles, obscuring the trap state population of the starting material.

4.5 FTIR Surface Chemistry Observation and Electron Monitoring

Infrared spectroscopy is an indispensable tool for the study of nanoparticle surfaces. FTIR techniques provide a fast, nondestructive method for identification of surface adsorbates. Shifts of characteristic infrared absorbance frequencies also provide information about the surface of adsorption in addition to qualitative identification of the adsorbates. For example, a red-shifted infrared absorbance frequency (i.e. shifted to lower value, corresponding to a longer wavelength) is an indication of weakened bonding in the adsorbate. This condition could arise from withdrawal of adsorbate electron density through bonding to a surface Lewis acid site. Alternately, population of adsorbate antibonding molecular orbitals with electrons from the adsorption surface could weaken the adsorbate bond and lead to a red-shifted absorbance frequency. The complementary utility of using the same infrared spectroscopy to simultaneously monitor electron population transitions is that it provides information to discern which of these cases might be applicable.

Infrared monitoring of electron population offers further information, beyond correlation of adsorbate IR frequency shifts. A common reaction mechanism step for catalytic adsorbate oxidation on reducible oxide surfaces (in the absence of gaseous oxygen) is lattice oxygen extraction through the Mars and van Krevelen mechanism.²²⁵⁻²²⁹ For titanium dioxide, this lattice oxygen extraction is accompanied by the formation of additional, populated shallow

trapped electrons (see Figure 15 on page 35) which are thermally excited to the conduction band. Through IR monitoring of electron populations, a lattice oxygen extraction mechanism could be identified for adsorbate oxidation. Similar scenarios can be described where nanoparticle electron population can be used to monitor surface coverage by electron withdrawing adsorbates (e.g. molecular O₂ or H₂O) or their displacement from the particle surface by reactive adsorbates.

4.6 Future Work

The FTIR vacuum cell offers a highly controlled environment to observe nanoparticle surface chemistry. This control of experimental variables comes at a cost of time. The procedures necessary to place new samples into the cell and condition them can require days to weeks before the cell and the samples within it are ready for experimental work. In addition to slow throughput, observation of nanoparticle catalysts under high vacuum is not representative of typical catalyst applications .

Dr. Dimitar Panayotov has designed and had fabricated a quartz flow cell for FTIR nanoparticle observation at nearly atmospheric pressure. This spectrometer cell is designed to contain a square tungsten mesh, identical to the material used as a nanoparticle carrier in the FTIR vacuum cell. With resistive heating, the FTIR flow cell is capable of conducting nanoparticle catalysis studies that parallel the vacuum cell studies with a continually replenished supply of reactant.

The geometry of the flow cell is arranged in a diamond orientation, with gas flow into and out of the cell occurring at opposite corners of the gas cavity, as shown in Figure 47. The gas expansion zone, located at the widest part of the gas cavity, falls directly above the location of the nanoparticle sample mounted within the cell. At this region of gas expansion, the linear velocity of the gas decreases, affording greater time for gas – nanoparticle interaction.

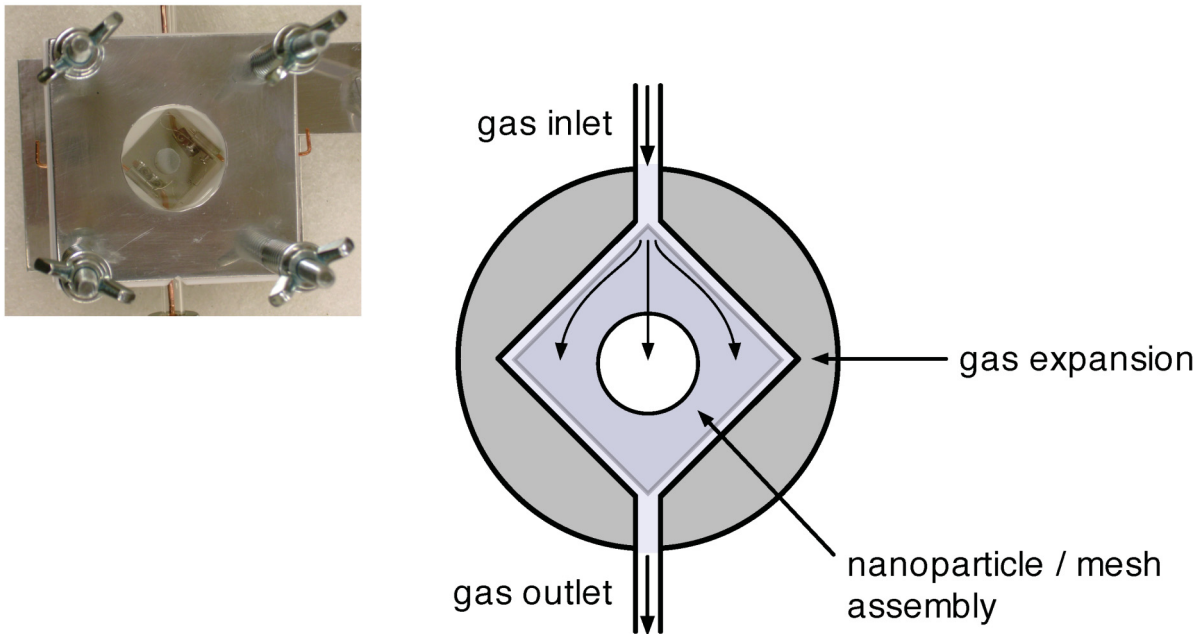


Figure 47: Nanoparticle FTIR flow cell. The photographic inset in the upper left corner is the prototype flow cell and flow cell mounting bracket. The circular region in the photograph is a sample of Degussa P25 titanium dioxide nanoparticles.

The FTIR flow cell is attached to an external gas routing system that allows for insertion of gaseous compounds or vaporized liquids into the carrier gas stream flowing through the cell. We hope to use this apparatus to examine chemical warfare agents interaction with nanoparticle system under conditions more accurately representative of applied usage of the catalysts.

Another advantage of the gas flow cell approach is quick sample through put. Because the flow cell operates at approximately atmospheric pressure, its gas seals can be less robust than those of a high vacuum chamber. With less stringent gas seal requirements, the flow cell can be rapidly set up or disassembled. It is hoped that when the flow cell apparatus is fully operational, several nanoparticle samples per week can be examined as opposed to one or two sets of nanoparticles per month for the FTIR vacuum cell. With this level of sample through put, the flow cell can serve as screening tool to identify nanoparticle samples that show promising characteristics which merit more detailed examination under high vacuum conditions.

Other interests include improvement of the laser vaporization procedure for nanoparticle synthesis. I would like to explore application of filter trapping of nanoparticles , electrostatic nanoparticle capture, and size segregation of particles to obtain more monodisperse samples of particles for particle size effect studies.

Appendix A: Density of States Derivation

Blakemore²³⁰ presented this derivation for calculating the density of electron states within a crystal lattice. Several assumptions are implicit in this derivation:

- Motions of electrons are restricted to the volume of the crystal.
- There are a finite number of electron states for the specified range of energies and momenta.
- The crystal lattice is much larger than the sizes of its component atoms.
- The electron ‘sees’ a homogeneous environment (uniform potential field) within the lattice.
- The electron potential energy V is zero within the lattice and infinite outside the lattice.
- The effects of the crystal surfaces are negligible.
- The electron wave function Ψ is periodic along each Cartesian axis of the lattice.

An electron delocalized from its original atom within a crystal lattice is free to move within the confines of that lattice space. Such an electron has momentum, represented by the vector $\vec{\rho}$. Quantum mechanics govern the actions of delocalized electrons and electrons possess wave-particle duality. The de Broglie wavelength of an electron is:

$$\lambda = \frac{h}{\rho} = \frac{h}{m_e v} \quad (81)$$

where ρ is the magnitude of the vector $\vec{\rho}$, m_e is the effective electron mass, and h is Planck’s constant. Each electron can also be represented by a wave-vector:

$$\vec{k} = \frac{\rho}{\hbar} \quad \text{where} \quad \hbar = \frac{h}{2\pi} \quad (82)$$

The wave-vector \vec{k} with scalar components k_x , k_y , and k_z , exists in a Cartesian coordinate vector space that is constructed by drawing a vector \vec{k} from the origin to a point k . The spherical surface formed by all wave-vectors \vec{k} for a given electron represents the degenerate energy states for that electron. Figure 48 shows \vec{k} -vector space for an electron:

Appendix A: Density of States Derivation (Continued)

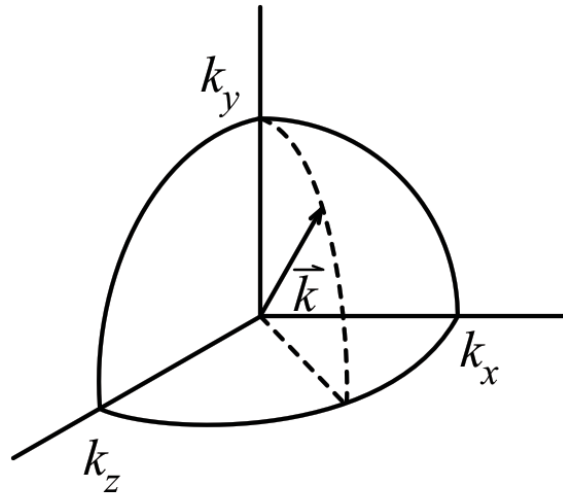


Figure 48: \vec{k} vector space for an electron.

For an electron represented by a \vec{k} wave-vector the following conditions must be true for the vector components:

$$\rho_x = \hbar k_x \quad \rho_y = \hbar k_y \quad \rho_z = \hbar k_z \quad (83)$$

The kinetic energy of the electron is:

$$E = \frac{\hbar^2}{2m_e} (k_x^2 + k_y^2 + k_z^2) = \frac{\hbar^2 k^2}{2m_e} \quad (84)$$

The time independent Schrödinger equation for the electron within the crystal lattice is:

$$-\frac{\hbar^2}{2m_e} \nabla^2 \Psi = E \Psi \quad (85)$$

An acceptable solution for the wave function Ψ is

$$\Psi = C \exp(i\vec{k} \cdot \vec{r}) \quad (86)$$

Appendix A: Density of States Derivation (Continued)

where \vec{r} is the radial displacement vector for \vec{k} . The wave function Ψ is defined such that the probability of finding an electron within a volume element τ is given by $|\Psi|^2 d\tau$. The periodicity of the wave function Ψ is L . Acceptable solutions for the wave function Ψ correspond to electron states within the lattice, if the following conditions are true:

$$k_x = n_x \frac{2\pi}{L}, \quad k_y = n_y \frac{2\pi}{L}, \quad k_z = n_z \frac{2\pi}{L} \quad (87)$$

where $n_x, n_y,$ and n_z are integers and can assume the values $0, \pm 1, \pm 2, \pm 3, \dots, \pm n$.

The Heisenberg uncertainty principle requires that if an electron position is determinate in L the electron must be indeterminate in momentum and wave-vector:

$$\Delta\rho = \frac{h}{L} \quad \text{and} \quad \Delta k = \frac{2\pi}{L} \quad (88)$$

Only specific positions in \vec{k} -space correspond to acceptable wave functions and each acceptable position is within a cell of volume $(2\pi/L)^3$. Figure 49 shows a range of such positions in the x-y plane and an example of a cell:

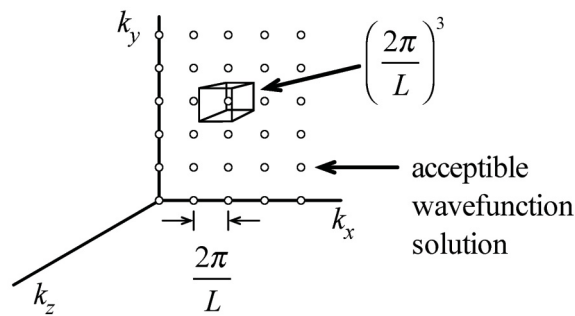


Figure 49: Acceptable wave function positions in the x-y plane.

The number of electron states within a sphere of radius k is found by dividing the volume of the sphere by the volume of a single wave function cell:

Appendix A: Density of States Derivation (Continued)

$$N = \left(\frac{4}{3} \pi k^3 \right) \left(\frac{L^3}{8\pi^3} \right) = \frac{k^3 L^3}{6\pi^2} \quad (89)$$

The change in the number of states for a change in sphere radius k is:

$$dN = \frac{k^2 L^3}{2\pi^2} dk \quad (90)$$

The change in the density of electron states per unit volume is:

$$\frac{dN}{L^3} = \frac{k^2}{2\pi^2} dk \quad (91)$$

Electrons are fermions and can assume two possible spin states of $+\frac{1}{2}$ and $-\frac{1}{2}$. This property doubles the density change of allowable electron states:

$$\frac{dN}{L^3} = \left(\frac{k}{\pi} \right)^2 dk \quad (92)$$

The density of states function g is defined for an infinitesimal change in energy or wave-vector as:

$$g(E)dE = g(k)dk = \left(\frac{k}{\pi} \right)^2 dk \quad (93)$$

The vector magnitude k can be solved for in Equation (84) to give:

$$k = \left(\frac{2m_e E}{\hbar^2} \right)^{\frac{1}{2}} \quad (94)$$

$$dk = \frac{1}{2} \left(\frac{2m_e}{\hbar^2} \right)^{\frac{1}{2}} E^{-\frac{1}{2}} dE \quad (95)$$

Appendix A: Density of States Derivation (Continued)

$$g(E)d(E) = \frac{1}{2\pi^2} \left(\frac{2m_e E}{\hbar^2} \right) \left(\frac{2m_e}{\hbar^2} \right)^{\frac{1}{2}} E^{-\frac{1}{2}} dE \quad (96)$$

$$g(E) = 4\pi \left(\frac{2m_e}{\hbar^2} \right)^{\frac{3}{2}} E^{\frac{1}{2}} \quad (97)$$

$$g(E) = \frac{2^{\frac{7}{2}} \pi m_e^{\frac{3}{2}}}{h^3} E^{\frac{1}{2}} \quad (98)$$

Q.E.D.

Appendix B: Fermi – Dirac Distribution Derivation

Blakemore²³⁰ presented this derivation for the Fermi-Dirac distribution Law. This derivation requires several assumptions:

- A very large number of electrons exist.
- The electrons at a given energy are indistinguishable.
- The number of electrons in the system and the total energy of all electrons is fixed.
- The system is in thermal equilibrium.

For g_i electron states with E_i energies, n_i represents the number of occupied electron states and $g_i - n_i$ represents the number of unoccupied states. The number of distinguishable distributions is:

$$w_i = \frac{g_i!}{n_i!(g_i - n_i)} \quad (99)$$

In addition to the g_i occupied electron states at energies E_i , there are other states at higher and lower energies. The combination of the w_i electron states and these other states comprises the system. The total number of distinguishable system distributions w is:

$$w = \prod_r w_r = \prod_r \frac{g_r!}{n_r!(g_r - n_r)} \quad (100)$$

The transitions of electrons between states are subject to these conditions:

$$n = \sum_r n_r \quad (101)$$

$$nE = \sum_r n_r E_r \quad (102)$$

The most probable distribution of electrons in states at thermal equilibrium:

Appendix B: Fermi – Dirac Distribution Derivation (Continued)

$$\frac{\delta w}{\delta n_r} = 0 \quad (103)$$

The factorials of very large numbers in the probability Equations (99) and (100) can be estimated with Stirling's approximation:

$$\ln y! = y \ln y - y \text{ for } y \gg 1 \quad (104)$$

Equation (100) becomes:

$$\ln w = \sum_r \left[g_r \ln g_r - n_r \ln n_r - (g_r - n_r) \ln (g_r - n_r) \right] \quad (105)$$

Rewrite conditions (101) and (102) as:

$$n - \sum_r n_r = 0 \quad (106)$$

$$nE - \sum_r n_r E_r = 0 \quad (107)$$

The maximum value of $\ln w$, subject to conditions (106) and (107) is found by the method of Lagrange undetermined multipliers. At a maximum for $\ln w$:

$$\frac{\delta}{\delta n_r} \left[\ln w + \alpha \left(n - \sum_r n_r \right) + \beta \left(nE - \sum_r n_r E_r \right) \right] = 0 \quad (108)$$

Differentiation of each term in (108) equation reference goes here gives:

$$\frac{\delta}{\delta n_r} \ln w = \ln \left(\frac{g_r - n_r}{n_r} \right) \quad (109)$$

Appendix B: Fermi – Dirac Distribution Derivation (Continued)

$$\frac{\delta}{\delta n_r} \left[\alpha \left(n - \sum_r n_r \right) \right] = -\alpha \quad (110)$$

$$\frac{\delta}{\delta n_r} \left[\beta \left(nE - \sum_r n_r E_r \right) \right] = -\beta E_r \quad (111)$$

Equation (108) becomes:

$$\ln \left(\frac{g_r - n_r}{n_r} \right) = \alpha + \beta E_r \quad (112)$$

$$\frac{n_r}{g_r} = \frac{1}{1 + \exp(\alpha + \beta E_r)} \quad (113)$$

For any of the states g_r within the system, the probability that an n_r particle at energy E_r occupies that state is:

$$f(E_r) = \frac{1}{1 + \exp(\alpha + \beta E_r)} \quad (114)$$

If we allow $\alpha = E_F/k_B T$ where E_F is defined as the Fermi energy and k_B is the Boltzmann constant, the energy of the highest occupied state at $T = 0\text{K}$ and $\beta = 1/(k_B T)$:

$$f(E_r) = \frac{1}{1 + \exp \left(\frac{E_r - E_F}{k_B T} \right)} \quad (115)$$

Q.E.D.

Appendix C: FORTRAN Program WaveShave.f

```

PROGRAM WaveShave
  INTEGER NumPoints, N, EOF1, EOF2
  REAL ReadFreq, ReadAbs, LowFreq, HighFreq
  CHARACTER*12 IRFileIn, IRFileOut, Spacer
  Spacer = ' '
*
* Frequency Filter Values
* *****
  LowFreq = 1.9E3
  HighFreq = 2.6E3
  OPEN (Unit=1, File='FILELIST.TXT', Status='OLD')
*
* Read in the data files to integrate
  EOF1 = 0
  DO WHILE (EOF1 .EQ. 0)
    READ (1, FMT = '(A12)', IOSTAT=EOF1) IRFileIn
*
* Check for EOF
* IF (EOF1 .EQ. -1) THEN
*   GO TO 700
*
* END IF
  PRINT *, ''
  PRINT *, IRFileIn
  PRINT *, '*****'
*
* Open the input file
  OPEN (Unit=2, File=IRFileIn, Status='OLD')
*
* Open the output file as a TXT type.
  IRFileOut = IRFileIn(1:10) // 'XT'
  EOF2 = 0
  OPEN (Unit=3, File=IRFileOut, Status='NEW')
  DO WHILE (EOF2 .EQ. 0)
    ReadFreq = 0
    ReadAbs = 0
500    READ (2, *, IOSTAT=EOF2) ReadFreq, ReadAbs
*
* Check for EOF
  IF (EOF2 .EQ. -1) THEN
    GO TO 550
  END IF
*
* Check for data points under the low wavenumber
  IF (ReadFreq .LT. LowFreq) THEN
    GO TO 500
  END IF
*
* Check for data points under the high wavenumber
  IF (ReadFreq .GT. HighFreq) THEN
    GO TO 500
  END IF
  PRINT *, ReadFreq, Spacer, ReadAbs
  WRITE (3, *) ReadFreq, ReadAbs
550  CLOSE (2)

```

Appendix C: FORTRAN Program WaveShave.f (Continued)

```
        CLOSE (3)
600    END DO
700    CLOSE (1)
        CLOSE (3)
        END
```

Appendix D: FORTRAN Program Trapint2.f

```

PROGRAM Trapint2
INTEGER NumPoints, N, EOF1, EOF2, Count1, Count2, NumDeltaFreq
REAL Freq, Freq0, Freq1, DeltaFreq, SumDeltaFreq, Abs, LeftAbs, RightAbs, IntArea
REAL ReadFreq, ReadAbs
CHARACTER*12 IRFile, Spacer
Count1 = 0
Count2 = 0
Spacer = ' '
*   Open the results output file
OPEN (Unit=3, File='INTRESULT.TXT', Status='NEW')
OPEN (Unit=1, File='FILELIST.TXT', Status='OLD')
*   Read in the data files to integrate
EOF1 = 0
DO WHILE (EOF1 .EQ. 0)
    READ (1, FMT = '(A12)', IOSTAT=EOF1) IRFile
    PRINT *, ''
    PRINT *, IRFile
    PRINT *, '*****'
    Count1 = Count1 + 1
*   Count the number of data points in file
    EOF2 = 0
    Count2 = 0
    OPEN (Unit=2, File=IRFile, Status='OLD')
    DO WHILE (EOF2 .EQ. 0)
        Count2 = Count2 + 1
        ReadFreq = 0
        ReadAbs = 0
        READ (2, *, IOSTAT=EOF2) ReadFreq, ReadAbs
        IF (EOF2 .EQ. -1) THEN
            GO TO 1000
        ENDIF
    END DO
1000 NumPoints = Count2
CLOSE (2)
*   Compute average DeltaFreq
EOF2 = 0
Count2 = 0
Freq0 = 0
Freq1 = 1
DeltaFreq = 0
SumDeltaFreq = 0
NumDeltaFreq = 0
OPEN (Unit=2, File=IRFile, Status='OLD')
DO WHILE (EOF2 .EQ. 0)

```

Appendix D: FORTRAN Program Trapint2.f (Continued)

```

1100  ReadFreq = 0
      ReadAbs = 0
      READ (2, *, IOSTAT=EOF2) ReadFreq, ReadAbs
      Count2 = Count2 + 1
*     First wavenumber
      IF (Count2 .EQ. 1) THEN
          Freq1 = ReadFreq
          GO TO 1100
      END IF
*     Last wavenumber
      IF (Count2 .EQ. NumPoints) THEN
          GO TO 1500
      END IF
      Freq0 = Freq1
      Freq1 = ReadFreq
      DeltaFreq = Freq1 - Freq0
      NumDeltaFreq = NumDeltaFreq + 1
      SumDeltaFreq = SumDeltaFreq + DeltaFreq
    END DO
1500  DeltaFreq = SumDeltaFreq / NumDeltaFreq
      CLOSE (2)
*     Integrate the data file
      EOF2 = 0
      Count2 = 0
      IntArea = 0
      OPEN (Unit=2, File=IRFile, Status='OLD')
      DO WHILE (EOF2 .EQ. 0)
1550  Count2 = Count2 + 1
          ReadFreq = 0
          ReadAbs = 0
          READ (2, *, IOSTAT=EOF2) ReadFreq, ReadAbs
          IF (Count2 .EQ. 1) THEN
              IntArea = IntArea + ReadAbs
              GO TO 1550
          END IF
          IF (Count2 .EQ. NumPoints) THEN
              IntArea = IntArea + ReadAbs
              GO TO 1600
          END IF
          IntArea = IntArea + (2*ReadAbs)
          PRINT '(I5.4, A2, E15.7, A2, E15.7, A2, E25.10, A2, E15.7)', Count2,
Spacer, DeltaFreq, Spacer, IntArea, Spacer, ReadFreq, Spacer, ReadAbs
      END DO
*     Compute the trapezoidal integral
1600  IntArea = (IntArea/2)*DeltaFreq
      PRINT *, '====='
```

Appendix D: FORTRAN Program Trapint2.f (Continued)

```
      PRINT '(E20.10)', IntArea
      WRITE (3, '(A12, E20.10)') IRFile, IntArea
      CLOSE (2)
      IF (EOF1 .EQ. -1) THEN
         GO TO 2000
      END IF
1800  END DO
2000  CLOSE (1)
      CLOSE (3)
      END
```

Appendix E: Nanoparticle Size Measurement Data Summary

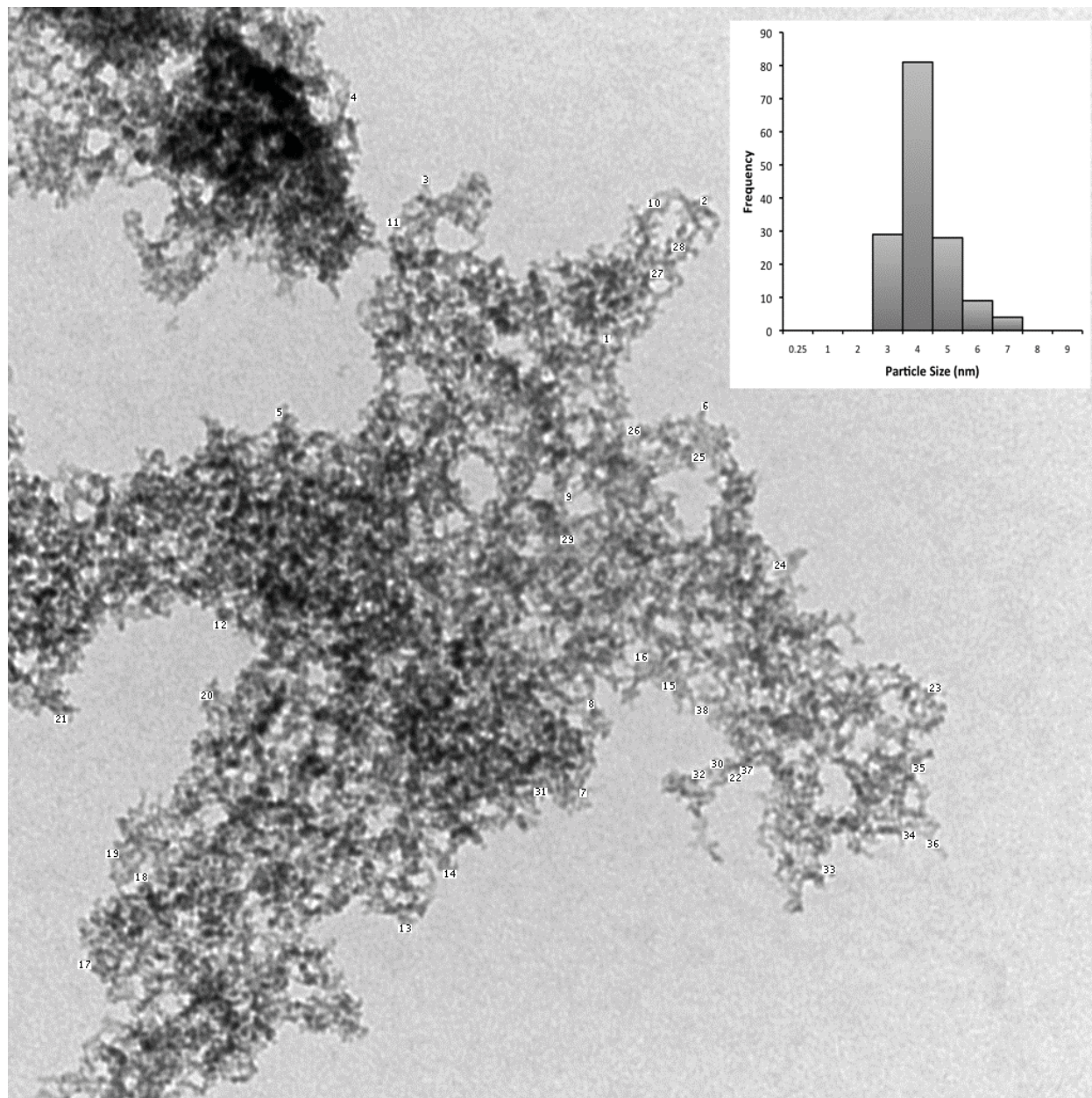
<i>Nanoparticles</i>	<i>Pellet to Collector (cm)</i>	<i>O₂ Press. (Torr)</i>	<i>Number of Measurements</i>	<i>Mean Diam. (nm)</i>	<i>Standard Deviation (nm)</i>
SPB013	4.4	1	235	7	1
SPB016	4.4	1	105	5	1
SPB017	4.4	1	172	4.8	0.9
SPB018 ^a	4.4	1	88	4.0	0.6
SPB024	4.4	5	111	5	1
SPB029	4.4	5	97	6	1
SPB022	4.4	10	97	6	1
SPB023	4.4	55	120	12	3
SPB025	4.4	90	62	12	3
SPB011	4.4	100	334	20	5
SPB019	4.4	200	147	22	7
SPB026	4.4	200	156	14	4
SPB037	4.4	200	296	27	9
SPB040	4.4	200	226	20	6
SPB027	4.4	310	49	24	6
SPB028	4.4	410	183	30	10
SPB020 ^b	4.4	500	192	30	10
SPB014	6.3	37	369	13	3
SPB015	2.3	37	247	12	4

^a Used for Fermi – Dirac regressions, vacuum cell sample S1

^b Used for Fermi – Dirac regressions, vacuum cell sample S1

Table 6: TiO₂ nanoparticle size measurement data.

Appendix F: SPB018 Transmission Electron Micrograph



spb.tem.32.tif

TiO₂ Nanoparticles

Print Mag: 290000x @ 8. in

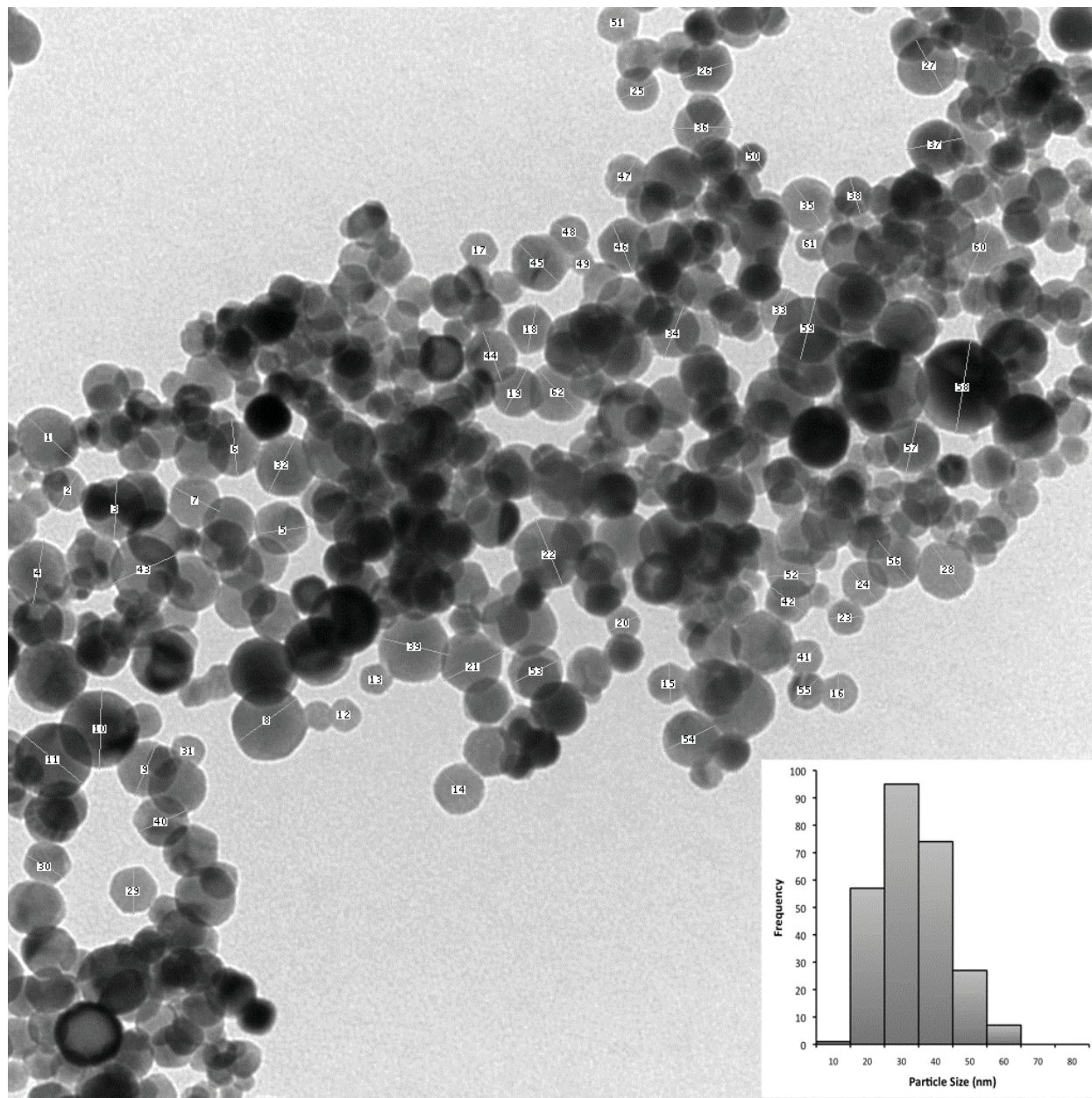
15:28 09/25/07

100 nm

Direct Mag: 160000x

Figure 50: TEM micrograph for SPB018 4.0 ± 0.6 nm titanium dioxide nanoparticles. Inset is a histogram of manual particle diameter measurements. Labels on particles are diameter measurement flags.

Appendix G: SPB020 Transmission Electron Micrograph



spb.tem.45.tif
TiO₂ Nanoparticles
Print Mag: 290000x @ 8. in
15:46 09/25/07

100 nm
Direct Mag: 160000x

Figure 51: TEM micrograph for SPB020 30 ± 10 nm titanium dioxide nanoparticles. Inset is a histogram of manual particle diameter measurements. Labels on particles are diameter measurement flags.

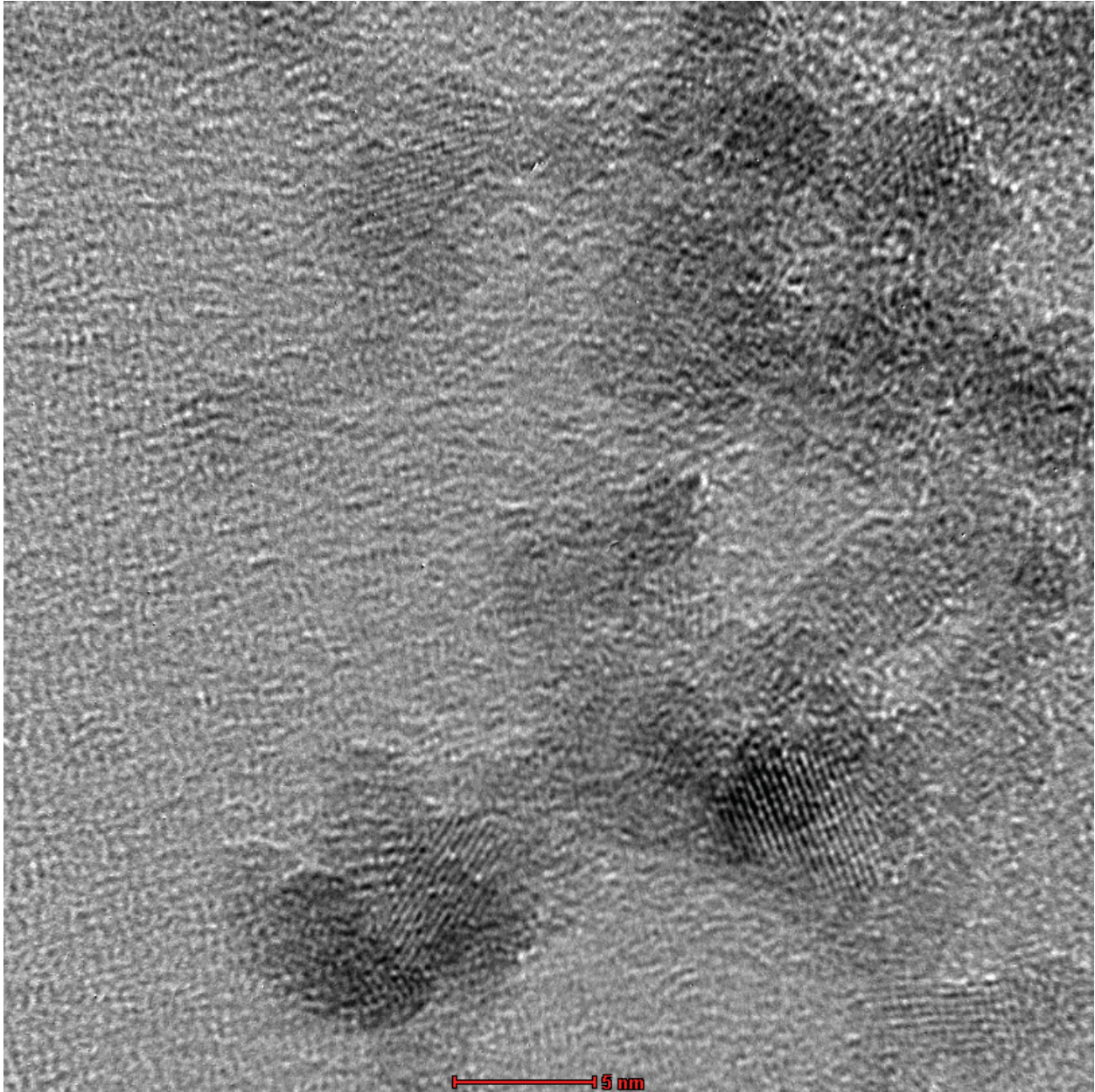


Figure 52: High resolution micrograph of SPB018 titanium dioxide nanoparticles.

Appendix I: Conduction Band Electron Population Calculation

This appendix outlines the details of the calculation for the number of electrons excited into the conduction band for a 4 nm (4×10^{-9} m) diameter titanium dioxide nanoparticle composed of the rutile polymorph (density = $0.235 \text{ g} \cdot \text{cm}^{-3}$)⁸⁴ with $E_{\text{state}} = 0.3 \text{ eV}$. The density of conduction band electrons is determined from Equation (61):

$$N_{CB}(E) = BT^{3/2} \text{Exp}\left(\frac{-CE_{\text{State}}}{T}\right) \quad \text{where} \quad B = \frac{2^{5/2}(m_e \pi k_B)}{h^3} \quad \text{and} \quad C = \frac{1}{2k_B}$$

The aggregate constants B and C are evaluated:

$$B = \frac{2^{5/2} (9.1094 \times 10^{-31} \text{ kg}) (3.1416) (1.3807 \times 10^{-23} \text{ J} \cdot \text{K}^{-1})}{(6.6261 \times 10^{-34} \text{ J} \cdot \text{s})^3}$$

$$1\text{J} = 1\text{N} \cdot \text{m} = 1(\text{kg} \cdot \text{m} \cdot \text{s}^{-2}) \cdot \text{m} = 1\text{kg} \cdot \text{m}^2 \cdot \text{s}^{-2}$$

$$B = \left(4.8296 \times 10^{21} \text{ K}^{-\frac{2}{3}} \cdot \text{m}^{-3}\right) \left(\frac{1\text{m}}{100\text{cm}}\right)^3$$

$$\boxed{B = 4.8296 \times 10^{15} \text{ K}^{-\frac{2}{3}} \cdot \text{cm}^{-3}}$$

$$C = \frac{1}{2(1.3807 \times 10^{-23} \text{ kg} \cdot \text{m}^2 \cdot \text{s}^{-2} \cdot \text{K}^{-1})}$$

$$1\text{eV} = 1.6022 \times 10^{-19} \text{ J}$$

$$C = \left[\frac{1}{2(1.3807 \times 10^{-23} \text{ J} \cdot \text{K}^{-1})} \right] \left(\frac{1.6022 \times 10^{-19} \text{ J}}{1\text{eV}} \right)$$

$$\boxed{C = 5.8021 \times 10^3 \text{ K} \cdot \text{eV}^{-1}}$$

For temperature $T = 298 \text{ K}$, Equation (61) is evaluated:

Appendix I: Conduction Band Electron Population Calculation (Continued)

$$N_{CB}(E) = \left(4.8296 \times 10^{15} K^{-\frac{3}{2}} \bullet cm^{-3}\right) (298 K)^{3/2} \text{Exp} \left(\frac{-(5.8021 \times 10^3 K \bullet eV^{-1})(0.3 eV)}{298 K} \right)$$

$$N_{CB}(E) = 7.22 \times 10^{16} cm^{-3}$$

The number of conduction band electrons for one gram of rutile at T = 298 K:

$$\frac{electrons}{gram} = \left(7.22 \times 10^{16} cm^{-3}\right) \left(\frac{1 cm^3}{4.26 g}\right) = \boxed{1.69 \times 10^{16} g^{-1}}$$

For T = 695 K, the number of conduction band electrons for one gram of rutile:

$$N_{CB}(E) = \left(4.8296 \times 10^{15} K^{-\frac{3}{2}} \bullet cm^{-3}\right) (675 K)^{3/2} \text{Exp} \left(\frac{-(5.8021 \times 10^3 K \bullet eV^{-1})(0.3 eV)}{675 K} \right)$$

$$N_{CB}(E) = 6.43 \times 10^{18} cm^{-3}$$

$$\frac{electrons}{gram} = \left(6.43 \times 10^{18} cm^{-3}\right) \left(\frac{1 cm^3}{4.26 g}\right) = \boxed{1.51 \times 10^{18} g^{-1}}$$

Constants and Conversion Factors⁹⁰

Boltzmann Constant:	$k = 1.3807 \times 10^{-23} J \bullet K^{-1}$
Plank Constant:	$h = 6.6261 \times 10^{-34} J \bullet s$
Electron Rest Mass:	$m_e = 9.1094 \times 10^{-31} kg$
eV to J Conversion:	$1 eV = 1.6022 \times 10^{-19} J$

References

1. Hammer, B.; Nørskov, J. K., Why gold is the noblest of all the metals? *Nature* **1995**, *376*, 238-240.
2. Ionization Energies of Atoms and Atomic Ions. In *CRC Handbook of Chemistry and Physics 88th Edition (Internet Version 2008)*, Lide, D. R., Ed. CRC Press/Taylor and Francis: Boca Raton, FL, 2008.
3. Electrical Resistivity of Pure Metals. In *CRC Handbook of Chemistry and Physics 88th Edition (Internet Version 2008)*, Lide, D. R., Ed. CRC Press/Taylor and Francis: Boca Raton, FL, 2008.
4. Bond, G. C., Catalysis by Gold. *Cat. Rev. - Sci. Eng.* **1999**, *41* (3&4), 319-388.
5. Haruta, M., When gold is not noble: Catalysis by nanoparticles. *Chemical Record* **2003**, *3* (2), 75-87.
6. Panayotov, D. A.; Yates, J. T., Spectroscopic detection of hydrogen atom spillover from Au nanoparticles supported on TiO₂: Use of conduction band electrons. *Journal of Physical Chemistry C* **2007**, *111* (7), 2959-2964.
7. Sakurai, H.; Haruta, M., Carbon-Dioxide and Carbon-Monoxide Hydrogenation over Gold Supported on Titanium, Iron, and Zinc-Oxides. *Applied Catalysis a-General* **1995**, *127* (1-2), 93-105.
8. Newman, J. D. S.; Roberts, J. M.; Blanchard, G. J., Optical organophosphate/phosphonate sensor based upon gold nanoparticle functionalized quartz. *Anal. Chim. Acta* **2007**, *602* (1), 101-107.
9. Newman, J. D. S.; Roberts, J. M.; Blanchard, G. J., Optical organophosphate sensor based upon gold nanoparticle functionalized fumed silica gel. *Anal. Chem.* **2007**, *79* (9), 3448-3454.
10. Simonian, A. L.; Good, T. A.; Wang, S. S.; Wild, J. R., Nanoparticle-based optical biosensors for the direct detection of organophosphate chemical warfare agents and pesticides. *Anal. Chim. Acta* **2005**, *534* (1), 69-77.
11. Panayotov, D. A.; Morris, J. R., Thermal Decomposition of a Chemical Warfare Agent Simulant (DMMP) on TiO₂: Production of Trapped Electrons during Reactions with Lattice Oxygen Virginia Tech: Blacksburg, VA, 2009.
12. Panayotov, D. A.; Morris, J. R., Catalytic Degradation of a Chemical Warfare Agent Simulant: Reaction Mechanisms on TiO₂-Supported Au Nanoparticles. *J. Phys. Chem. C* **2008**, (112), 7496-7502.
13. Sagatelian, Y.; Sharabi, D.; Paz, Y., Enhanced photodegradation of diisopropyl methyl phosphonate by the "Adsorb & Shuttle" approach. *Journal of Photochemistry and Photobiology A: Chemistry* **2005**, (174), 253-260.

References

14. Obee, T. N.; Satyapal, S., Photocatalytic decomposition of DMMP on titania. *Journal of Photochemistry and Photobiology a-Chemistry* **1998**, *118* (1), 45-51.
15. Daoud, W. A.; Turner, M. L., Effect of interfacial properties and film thickness on device performance of bilayer TiO₂-poly(1,4-phenylenevinylene) solar cells prepared by spin coating. *Reactive & Functional Polymers* **2006**, *66* (1), 13-20.
16. Ravirajan, P.; Bradley, D. D. C.; Nelson, J.; Haque, S. A.; Durrant, J. R.; Smit, H. J. P.; Kroon, J. M., Efficient charge collection in hybrid polymer/TiO₂ solar cells using poly(ethylenedioxythiophene) polystyrene sulphonate as hole collector. *Appl. Phys. Lett.* **2005**, *86* (14), 1-3.
17. Kal, S. H.; Joseph, J.; Lee, J.; Kim, K. J., Enhancement in performance of dye-sensitized solar cells modified with in situ photopolymerized PDEA in TiO₂ films. *J. Electrochem. Soc.* **2005**, *152* (7), A1378-A1381.
18. Usami, A., Theoretical simulations of optical confinement in dye-sensitized nanocrystalline solar cells. *Sol. Energy Mater. Sol. Cells* **2000**, *64* (1), 73-83.
19. Usami, A.; Ozaki, H., Computer simulations of charge transport in dye-sensitized nanocrystalline photovoltaic cells. *J. Phys. Chem. B* **2001**, *105* (20), 4577-4583.
20. Hagfeldt, A.; Grätzel, M., Molecular Photovoltaics. *Acc. Chem. Res.* **2000**, (33), 269-277.
21. Nelson, J.; Haque, S. A.; Klug, D. R.; Durrant, J. R., Trap-limited recombination in dye-sensitized nanocrystalline metal oxide electrodes. *Physical Review B* **2001**, *63*, 1-9.
22. Bamwenda, G. R.; Tsubota, S.; Kobayashi, T.; Haruta, M., Photoinduced Hydrogen-Production from an Aqueous-Solution of Ethylene-Glycol over Ultrafine Gold Supported on Tio₂. *Journal of Photochemistry and Photobiology a-Chemistry* **1994**, *77* (1), 59-67.
23. Bamwenda, G. R.; Tsubota, S.; Nakamura, T.; Haruta, M., Photoassisted Hydrogen-Production from a Water-Ethanol Solution - a Comparison of Activities of Au-Tio₂ and Pt-Tio₂. *Journal of Photochemistry and Photobiology a-Chemistry* **1995**, *89* (2), 177-189.
24. Ni, M.; Leung, M. K. H.; Leung, D. Y. C.; Sumathy, K., A review and recent developments in photocatalytic water-splitting using TiO₂ for hydrogen production. *Renewable and Sustainable Energy Reviews* **2007**, (11), 401-425.
25. Nowotny, J.; Bak, T.; Nowotny, M. K.; Sheppard, L. R., Titanium dioxide for solar-hydrogen I. Functional properties. *Int. J. Hydrogen Energy* **2007**, *32*, 2609-2629.
26. Nowotny, J.; Bak, T.; Nowotny, M. K.; Sheppard, L. R., Titanium dioxide for solar-hydrogen II. Defect chemistry. *Int. J. Hydrogen Energy* **2007**, *32* (14), 2630-2643.

References

27. Nowotny, J.; Bak, T.; Nowotny, M. K.; Sheppard, L. R., Titanium dioxide for solar-hydrogen IV. Collective and local factors in photoreactivity. *Int. J. Hydrogen Energy* **2007**, *32* (14), 2651-2659.
28. Dobosz, A.; Sobczynski, A., Water detoxification: Photocatalytic decomposition of phenol on Au/TiO₂. *Monatsh. Chem.* **2001**, *132* (9), 1037-1045.
29. Anpo, M., Utilization of TiO₂ photocatalysts in green chemistry. *Pure Appl. Chem.* **2000**, *72* (7), 1265–1270.
30. Evgenidou, E.; Konstantinou, I.; Fytianos, K.; Poulios, I., Oxidation of two organophosphorous insecticides by the photo-assisted Fenton reaction. *Water Res.* **2007**, *41* (9), 2015-2027.
31. Evgenidou, E.; Konstantinou, I.; Fytianos, K.; Poulios, I.; Albanis, T., Photocatalytic oxidation of methyl parathion over TiO₂ and ZnO suspensions. *Catal. Today* **2007**, *124* (3-4), 156-162.
32. Kim, T. S.; Kim, J. K.; Choi, K.; Stenstrom, M. K.; Zoh, K. D., Degradation mechanism and the toxicity assessment in TiO₂ photocatalysis and photolysis of parathion. *Chemosphere* **2006**, *62* (6), 926-933.
33. Kaneco, S.; Li, N.; Itoh, K. K.; Katsumata, H.; Suzuki, K.; Ohta, K., Titanium dioxide mediated solar photocatalytic degradation of thiram in aqueous solution: Kinetics and mineralization. *Chem. Eng. J.* **2009**, *148* (1), 50-56.
34. Beydoun, D.; Amal, R.; Low, G.; McEvoy, S., Role of nanoparticles in photocatalysis. *J. Nanopart. Res.* **1999**, (1), 439–458.
35. Pauling, L.; Pauling, P., *Chemistry*. W.H. Freeman and Company: San Francisco, 1975; p 767.
36. Lindley, D., -, *Boltzmann's atom : the great debate that launched a revolution in physics*. Free Press: New York :, 2001; Vol. xi, p 260.
37. Castellan, G. W., *Physical Chemistry*. Third ed.; Benjamin / Cummings Publishing Company, Inc.: Menlo Park, California, 1983.
38. Murr, L. E.; Kinard, W. H., Effects of Low Earth Orbit. *American Scientist* **1993**, *81* (2), 152-165.
39. Collins, F. G., Recent advances to enhance low Earth orbit space simulation. *Journal of Vacuum Science & Technology A* **2008**, *26* (4), 1042-1049.
40. Halliday, D.; Resnick, R., *Fundamentals of Physics*. 2 ed.; John Wiley & Sons: New York, 1981.
41. Cropper, W. H., *Great Physicists*. Oxford University Press, Inc.: New York, 2001.

References

42. Blakemore, J. S., *Solid State Physics*. W. B. Saunders Company: Philadelphia, 1969; p 391.
43. Blakemore, J. S., *Solid State Physics*. Cambridge University Press: Cambridge, UK, 1985.
44. Bloch, F., Memories of Electrons in Crystals. *Proceedings of the Royal Society of London Series a-Mathematical Physical and Engineering Sciences* **1980**, 371 (1744), 24-27.
45. Kronig, R. d. L.; Penney, W. G., Quantum Mechanics of Electrons in Crystal Lattices. *Proc. R. Soc. London, Ser. A* **1931**, 130, 499-513.
46. McQuarrie, D. A., The Kronig-Penney Model: A Single Lecture Illustrating the Band Structure of Solids. *The Chemical Educator* **1996**, 1 (1), 1-10.
47. Yoffe, A. D., Low-Dimensional Systems - Quantum-Size Effects and Electronic-Properties of Semiconductor Microcrystallites (Zero-Dimensional Systems) and Some Quasi-2-Dimensional Systems. *Advances in Physics* **1993**, 42 (2), 173-266.
48. Bube, R. H., *Electrons in Solids: An Introductory Survey*. Third ed.; Academic Press, Inc.: New York, 1992.
49. Shriver, D.; Atkins, P., *Inorganic Chemistry*. 3rd ed.; W. H. Freeman and Company: New York, 1999; p 763.
50. Pankove, J. I., *Optical Processes in Semiconductors*. Dover Publications, Inc.: Mineola, N.Y., 1975.
51. Hammond, C. R., The Elements. In *CRC Handbook of Chemistry and Physics 88th Edition (Internet Version 2008)*, Lide, D. R., Ed. CRC Press/Taylor and Francis: Boca Raton, FL, 2008.
52. Emsley, J., *Nature's Building Blocks: An A-Z Guide to the Elements*. Oxford University Press, Inc.: 2001; Vol. New York, p 538.
53. Zhou, Y. L.; Niinomi, M.; Akahori, T.; Fukui, H.; Toda, H., Corrosion resistance and biocompatibility of Ti-Ta alloys for biomedical applications. *Materials Science and Engineering a-Structural Materials Properties Microstructure and Processing* **2005**, 398 (1-2), 28-36.
54. Shtansky, D. V.; Gloushankova, N. A.; Bashkova, I. A.; Petrzhik, M. I.; Sheveiko, A. N.; Kiryukhantsev-Korneev, F. V.; Reshetov, I. V.; Grigoryan, A. S.; Levashov, E. A., Multifunctional biocompatible nanostructured coatings for load-bearing implants. *Surface & Coatings Technology* **2006**, 201 (7), 4111-4118.
55. Production and Stocks of Titanium Dioxide: December 2003. Commerce, U. S. D. o., Ed. Washington D.C., 2003.

References

56. Nohynek, G. J.; Lademann, J.; Ribaud, C.; Roberts, M. S., Grey goo on the skin? Nanotechnology, cosmetic and sunscreen safety. *Crit. Rev. Toxicol.* **2007**, *37* (3), 251-277.
57. Nevin, R., Trends in preschool lead exposure, mental retardation, and scholastic achievement: Association or causation? *Environ. Res.* **2009**, *109* (3), 301-310.
58. Vaidyanathan, A.; Staley, F.; Shire, J.; Muthukumar, S.; Kennedy, C.; Meyer, P. A.; Brown, M. J., Screening for Lead Poisoning: A Geospatial Approach to Determine Testing of Children in At-Risk Neighborhoods. *Journal of Pediatrics* **2009**, *154* (3), 409-414.
59. Warheit, D. B.; Sayes, C. M.; Reed, K. L.; Swain, K. A., Health effects related to nanoparticle exposures: Environmental, health and safety considerations for assessing hazards and risks. *Pharmacology & Therapeutics* **2008**, *120* (1), 35-42.
60. Warheit, D. B.; Webb, T. R.; Reed, K. L.; Frerichs, S.; Sayes, C. M., Pulmonary toxicity study in rats with three forms of ultrafine-TiO₂ particles: Differential responses related to surface properties. *Toxicology* **2007**, *230* (1), 90-104.
61. Warheit, D. B.; Webb, T. R.; Sayes, C. M.; Colvin, V. L.; Reed, K. L., Pulmonary instillation studies with nanoscale TiO₂ rods and dots in rats: Toxicity is not dependent upon particle size and surface area. *Toxicol. Sci.* **2006**, *91* (1), 227-236.
62. Sayes, C. M.; Wahi, R.; Kurian, P. A.; Liu, Y. P.; West, J. L.; Ausman, K. D.; Warheit, D. B.; Colvin, V. L., Correlating nanoscale titania structure with toxicity: A cytotoxicity and inflammatory response study with human dermal fibroblasts and human lung epithelial cells. *Toxicol. Sci.* **2006**, *92* (1), 174-185.
63. Liu, R.; Yin, L. H.; Pu, Y. P.; Liang, G. Y.; Zhang, J.; Su, Y. Y.; Xiao, Z. P.; Ye, B., Pulmonary toxicity induced by three forms of titanium dioxide nanoparticles via intra-tracheal instillation in rats. *Progress in Natural Science* **2009**, *19* (5), 573-579.
64. Gurr, J. R.; Wang, A. S. S.; Chen, C. H.; Jan, K. Y., Ultrafine titanium dioxide particles in the absence of photoactivation can induce oxidative damage to human bronchial epithelial cells. *Toxicology* **2005**, *213* (1-2), 66-73.
65. Chen, H. W.; Su, S. F.; Chien, C. T.; Lin, W. H.; Yu, S. L.; Chou, C. C.; Chen, J. J. W.; Yang, P. C., Titanium dioxide nanoparticles induce emphysema-like lung injury in mice. *FASEB J.* **2006**, *20* (13), E1732-E1741.
66. Chen, Z.; Meng, H.; Xing, G. M.; Yuan, H.; Zhao, F.; Liu, R.; Chang, X. L.; Gao, X. Y.; Wang, T. C.; Jia, G.; Ye, C.; Chai, Z. F.; Zhao, Y. L., Age-Related Differences in Pulmonary and Cardiovascular Responses to SiO₂ Nanoparticle Inhalation: Nanotoxicity Has Susceptible Population. *Environmental Science & Technology* **2008**, *42* (23), 8985-8992.
67. Bermudez, E.; Mangum, J. B.; Wong, B. A.; Asgharian, B.; Hext, P. M.; Warheit, D. B.; Everitt, J. I., Pulmonary responses of mice, rats, and hamsters to subchronic inhalation of ultrafine titanium dioxide particles. *Toxicol. Sci.* **2004**, *77* (2), 347-357.

References

68. Fujishima, A.; Zhang, X.; Tryk, D. A., TiO₂ photocatalysis and related surface phenomena. *Surf. Sci. Rep.* **2008**, (63), 515-582.
69. Renz, C., Lichtreaktionen der Oxyde des Titans, Cers, und der Erdsäuren. *Helv. Chim. Acta* **1921**, 4, 961-968.
70. Henrich, V. E.; Cox, P. A., *The Surface Science of Metal Oxides*. Cambridge University press: Cambridge, 1994.
71. Muscat, J.; Swamy, V.; Harrison, N. M., First-principles calculations of the phase stability of TiO₂. *Physical Review B* **2002**, 65 (22), 1-15.
72. Dewhurst, J. K.; Lowther, J. E., High-pressure structural phases of titanium dioxide. *Physical Review B* **1996**, 54 (6), R3673-R3675.
73. El Goresy, A.; Chen, M.; Dubrovinsky, L.; Gillet, P.; Graup, G., An ultradense polymorph of rutile with seven-coordinated titanium from the Ries crater. *Science* **2001**, 293 (5534), 1467-1470.
74. El Goresy, A.; Chen, M.; Gillet, P.; Dubrovinsky, L.; Graup, G.; Ahuja, R., A natural shock-induced dense polymorph of rutile with alpha-PbO₂ structure in the suevite from the Ries crater in Germany. *Earth. Planet. Sci. Lett.* **2001**, 192 (4), 485-495.
75. Sekiya, T.; Okumura, M.; Kurita, S.; Hamaya, N., Pressure-induced phase transformation within anatase titanium dioxide. *High Pressure Research* **2003**, 23 (3), 333-338.
76. Ghosh, T. B.; Dhabal, S.; Datta, A. K., On crystallite size dependence of phase stability of nanocrystalline TiO₂. *J. Appl. Phys.* **2003**, 94 (7), 4577-4582.
77. Barnard, A. S.; Zapol, P., Effects of particle morphology and surface hydrogenation on the phase stability of TiO₂. *Physical Review B* **2004**, 70 (23), 235403 1-13.
78. Hengerer, R.; Bolliger, B.; Erbudak, M.; Gratzel, M., Structure and stability of the anatase TiO₂ (101) and (001) surfaces. *Surf. Sci.* **2000**, 460 (1-3), 162-169.
79. Gribb, A. A.; Banfield, J. F., Particle size effects on transformation kinetics and phase stability in nanocrystalline TiO₂. *Am. Mineral.* **1997**, 82 (7-8), 717-728.
80. Lu, H. M.; Zhang, W. X.; Jiang, Q., Phase stability of nanoanatase. *Adv. Eng. Mater.* **2003**, 5 (11), 787-788.
81. Zhang, H. Z.; Banfield, J. F., Phase stability in the nanocrystalline TiO₂ system. *Phase Transformations and Systems Driven Far from Equilibrium* **1998**, 481, 619-624.
82. Olson, C. L.; Nelson, J.; Islam, M. S., Defect Chemistry, Surface Structures, and Lithium Insertion in Anatase TiO₂. *J. Phys. Chem. B* **2006**, A - G.

References

83. Naicker, P. K.; Cummings, P. T.; Zhang, H. Z.; Banfield, J. F., Characterization of titanium dioxide nanoparticles using molecular dynamics simulations. *J. Phys. Chem. B* **2005**, *109* (32), 15243-15249.
84. Diebold, U., The surface science of titanium dioxide. *Surf. Sci. Rep.* **2003**, (48), 53-229.
85. Kavan, L.; Grätzel, M.; Gilbert, S. E.; Klemenz, C.; Scheel, H. J., Electrochemical and Photoelectrochemical Investigation of Single-Crystal Anatase. *J. Am. Chem. Soc.* **1996**, (118), 6716-6723.
86. Kim, Y. I.; Atherton, S. J.; Brigham, E. S.; Mallouk, T. E., Sensitized Layered Metal-Oxide-Semiconductor Particles for Photochemical Hydrogen Evolution from Nonsacrificial Electron-Donors. *J. Phys. Chem.* **1993**, *97* (45), 11802-11810.
87. Shibata, T.; Irie, H.; Ohmori, M.; Nakajima, A.; Watanabe, T.; Hashimoto, K., Comparison of photochemical properties of brookite and anatase TiO₂ films. *PCCP* **2004**, *6* (6), 1359-1362.
88. Koelsch, M.; Cassaignon, S.; Guillemoles, J. F.; Jolivet, J. R., Comparison of optical and electrochemical properties of anatase and brookite TiO₂ synthesized by the sol-gel method. *Thin Solid Films* **2002**, *403*, 312-319.
89. Tang, H.; Berger, H.; Schmid, P. E.; Levy, F.; Burri, G., Photoluminescence in TiO₂ Anatase Single-Crystals. *Solid State Commun.* **1993**, *87* (9), 847-850.
90. Atkins, P.; Paula, J. d., *Physical Chemistry, Seventh Edition*. W.H. Freeman and Company: New York, 2002.
91. Roduner, E., *Nanoscopic Materials: Size-dependent Phenomena*. Royal Society of Chemistry: 2006; p 285.
92. Kormann, C.; Bahnemann, D. W.; Hoffmann, M. R., Preparation and Characterization of Quantum-Size Titanium Dioxide. *J. Phys. Chem.* **1988**, (92), 5196-5201.
93. Wang, Y.; Herron, N., Quantum Size Effects on the Exciton Energy of Cds Clusters. *Physical Review B* **1990**, *42* (11), 7253-7255.
94. Lockwood, D. J., Optical-Properties of Porous Silicon. *Solid State Commun.* **1994**, *92* (1-2), 101-112.
95. Lockwood, D. J.; Wang, A.; Bryskiewicz, B., Optical-Absorption Evidence for Quantum Confinement Effects in Porous Silicon. *Solid State Commun.* **1994**, *89* (7), 587-589.
96. King, D. M.; Du, X. H.; Cavanagh, A. S.; Weimer, A., Quantum confinement in amorphous TiO₂ films studied via atomic layer deposition. *Nanotechnology* **2008**, *19* (44), 1-6.
97. Mott, N. F., *Elementary Quantum Mechanics*. Springer - Verlag New York, Inc.: New York, 1972.

References

98. Göpel, W.; Anderson, J. A.; Frankel, D.; Jaehnig, M.; Phillips, K.; Schäfer, J. A.; Rucker, G., Surface Defects of TiO₂(110): A Combined XPS, XAES and ELS Study. *Surf. Sci.* **1984**, (139), 333-346.
99. Ghosh, A. K.; Wakim, F. G.; R.R. Addiss, J., Photoelectric Processes in Rutile. *Physical Review* **1969**, *184* (3), 979-988.
100. Lagemaat, J. v. d.; Frank, A. J., Nonthermalized Electron Transport in Dye-Sensitized Nanocrystalline TiO₂ Films: Transient Photocurrent and Random-Walk Modeling Studies. *J. Phys. Chem. B* **2001**, (105), 11194-11205.
101. Mora-Seró, I.; Bisquert, J., Fermi Level of Surface States in TiO₂ Nanoparticles. *Nano Lett.* **2003**, *3* (7), 945-949.
102. Lyon, L. A.; Hupp, J. T., Energetics of the nanocrystalline titanium dioxide aqueous solution interface: Approximate conduction band edge variations between H₀=-10 and H_∞=+26. *J. Phys. Chem. B* **1999**, *103* (22), 4623-4628.
103. Wang, H. L.; He, J. J.; Boschloo, G.; Lindstrom, H.; Hagfeldt, A.; Lindquist, S. E., Electrochemical investigation of traps in a nanostructured TiO₂ film. *J. Phys. Chem. B* **2001**, *105* (13), 2529-2533.
104. Cao, F.; Oskam, G.; Searson, P. C.; Stipkala, J. M.; Heimer, T. A.; Farzad, F.; Meyer, G. J., Electrical and Optical-Properties of Porous Nanocrystalline TiO₂ Films. *J. Phys. Chem.* **1995**, *99* (31), 11974-11980.
105. Muscat, J.; Harrison, N. M.; Thornton, G., First-principles study of potassium adsorption on TiO₂ surfaces. *Physical Review B* **1999**, *59* (23), 15457-15463.
106. Zanden, B. v. d.; Goossens, A., The Nature of Electron Migration in Dye-Sensitized Nanostructured TiO₂. *J. Phys. Chem. B* **2000**, (104), 7171-7178.
107. Shinde, P. S.; Bhosale, C. H., Properties of chemical vapour deposited nanocrystalline TiO₂ thin films and their use in dye-sensitized solar cells. *J. Anal. Appl. Pyrolysis* **2008**, *82* (1), 83-88.
108. Zhang, X. T.; Udagawa, K.; Liu, Z. Y.; Nishimoto, S.; Xu, C. S.; Liu, Y. C.; Sakai, H.; Abe, M.; Murakami, T.; Fujishima, A., Photocatalytic and photoelectrochemical studies on N-doped TiO₂ photocatalyst. *Journal of Photochemistry and Photobiology a-Chemistry* **2009**, *202* (1), 39-47.
109. Xue, J. B.; Li, Q.; Liang, W.; Shang, J. K., Electronic Band Structures of TiO₂ with Heavy Nitrogen Doping. *Journal of Wuhan University of Technology-Materials Science Edition* **2008**, *23* (6), 799-803.
110. Mitoraj, D.; Kisch, H., The Nature of Nitrogen-Modified Titanium Dioxide Photocatalysts Active in Visible Light. *Angewandte Chemie-International Edition* **2008**, *47* (51), 9975-9978.

References

111. Mahalingam, S.; Edirisinghe, M. J., Novel preparation of nitrogen-doped titanium dioxide films. *Journal of Physics D-Applied Physics* **2008**, *41* (21), -.
112. Liu, G.; Wang, X. W.; Wang, L. Z.; Chen, Z. G.; Li, F.; Lu, G. Q.; Cheng, H. M., Drastically enhanced photocatalytic activity in nitrogen doped mesoporous TiO₂ with abundant surface states. *J. Colloid Interface Sci.* **2009**, *334* (2), 171-175.
113. Liu, G.; Wang, X. W.; Chen, Z. G.; Cheng, H. M.; Lu, G. Q., The role of crystal phase in determining photocatalytic activity of nitrogen doped TiO₂. *J. Colloid Interface Sci.* **2009**, *329* (2), 331-338.
114. Jagadale, T. C.; Takale, S. P.; Sonawane, R. S.; Joshi, H. M.; Patil, S. I.; Kale, B. B.; Ogale, S. B., N-doped TiO₂ nanoparticle based visible light photocatalyst by modified peroxide sol-gel method. *Journal of Physical Chemistry C* **2008**, *112* (37), 14595-14602.
115. Ohno, T.; Akiyoshi, M.; Umebayashi, T.; Asai, K.; Mitsui, T.; Matsumura, M., Preparation of S-doped TiO₂ photocatalysts and their photocatalytic activities under visible light. *Applied Catalysis a-General* **2004**, *265* (1), 115-121.
116. Tang, X. H.; Li, D. Y., Sulfur-doped highly ordered TiO₂ nanotubular arrays with visible light response. *Journal of Physical Chemistry C* **2008**, *112* (14), 5405-5409.
117. Umebayashi, T.; Yamaki, T.; Itoh, H.; Asai, K., Band gap narrowing of titanium dioxide by sulfur doping. *Appl. Phys. Lett.* **2002**, *81* (3), 454-456.
118. Umebayashi, T.; Yamaki, T.; Yamamoto, S.; Miyashita, A.; Tanaka, S.; Sumita, T.; Asai, K., Sulfur-doping of rutile-titanium dioxide by ion implantation: Photocurrent spectroscopy and first-principles band calculation studies. *J. Appl. Phys.* **2003**, *93* (9), 5156-5160.
119. Zhou, Z. Q.; Zhang, X. Y.; Wu, Z.; Dong, L. M., Mechanochemical preparation of sulfur-doped nanosized TiO₂ and its photocatalytic activity under visible light. *Chin. Sci. Bull.* **2005**, *50* (23), 2691-2695.
120. Giannakopoulou, T.; Todorova, N.; Vaimakis, T.; Ladas, S.; Trapalis, C., Study of fluorine-doped TiO₂ sol-gel thin coatings. *Journal of Solar Energy Engineering-Transactions of the Asme* **2008**, *130* (4), 1-5.
121. Todorova, N.; Giannakopoulou, T.; Romanos, G.; Vaimakis, T.; Yu, J. G.; Trapalis, C., Preparation of fluorine-doped TiO₂ photocatalysts with controlled crystalline structure. *International Journal of Photoenergy* **2008**, 1-9.
122. Todorova, N.; Giannakopoulou, T.; Vaimakis, T.; Trapalis, C., Structure tailoring of fluorine-doped TiO₂ nanostructured powders. *Materials Science and Engineering B-Advanced Functional Solid-State Materials* **2008**, *152* (1-3), 50-54.
123. Xu, J. J.; Ao, Y. H.; Fu, D. G.; Yuan, C. W., Low-temperature preparation of F-doped TiO₂ film and its photocatalytic activity under solar light. *Appl. Surf. Sci.* **2008**, *254* (10), 3033-3038.

References

124. Yamaki, T.; Umebayashi, T.; Sumita, T.; Yamamoto, S.; Maekawa, M.; Kawasuso, A.; Itoh, H., Fluorine-doping in titanium dioxide by ion implantation technique. *Nuclear Instruments & Methods in Physics Research Section B-Beam Interactions with Materials and Atoms* **2003**, *206*, 254-258.
125. Kolasinski, K. W., *Surface Science*. John Wiley & Sons, Inc.: New York, 2002.
126. Thompson, T. L.; John T. Yates, J., Monitoring Hole Trapping in Photoexcited TiO₂(110) Using a Surface Photoreaction. *J. Phys. Chem. B* **2005**, (109), 18230-18236.
127. Matthiesen, J.; Wendt, S.; Hansen, J. Ø.; Madsen, G. K. H.; Lira, E.; Patrick Galliker; Vestergaard, E. K.; Schaub, R.; Lægsgaard, E.; Hammer, B.; Besenbacher, F., Observation of All the Intermediate Steps of a Chemical Reaction on an Oxide Surface by Scanning Tunneling Microscopy. *Acs Nano* **2009**, A - J.
128. Szczepankiewicz, S. H.; Moss, J. A.; Hoffmann, M. R., Electron Traps and the Stark Effect on Hydroxylated Titania Photocatalysts. *J. Phys. Chem. B* **2002**, *106*, 7654-7658.
129. R.R. Addiss, J.; Ghosh, A. K.; Wakim, F. G., Thermally Stimulated Currents and Luminescence in Rutile (TiO₂). *Appl. Phys. Lett.* **1968**, *12* (11), 397-400.
130. Matijević, E.; Sapiieszko, R. S., Forced Hydrolysis in Homogeneous Solutions. In *Fine Particles: Synthesis, Characterization, and Mechanisms of Growth*, Sugimoto, T., Ed. Marcel Dekker, Inc.: 2000; pp 2-34.
131. Matijevic, E.; Budnik, M.; Meites, L., Preparation and Mechanism of Formation of Titanium-Dioxide Hydrosols of Narrow Size Distribution. *J. Colloid Interface Sci.* **1977**, *61* (2), 302-311.
132. Matijević, E.; Bell, A.; Brace, R.; McFadyen, P., Formation and Surface Characteristics of Hydrous Metal Oxide Sols. *J. Electrochem. Soc.* **1973**, *129* (7), 893-899.
133. Kim, S.-J.; Park, S.-D.; Jeong, Y. H., Homogeneous Precipitation of TiO₂ Ultrafine Powders from Aqueous TiOCl₂ Solution. *Journal of the American Ceramics Society* **1999**, (4), 927-932.
134. Pottier, A.; Chaneac, C.; Tronc, E.; Mazerolles, L.; Jolivet, J. P., Synthesis of brookite TiO₂ nanoparticles by thermolysis of TiCl₄ in strongly acidic aqueous media. *J. Mater. Chem.* **2001**, *11* (4), 1116-1121.
135. Li, Y.; Fan, Y.; Chena, Y., A novel method for preparation of nanocrystalline rutile TiO₂ powders by liquid hydrolysis of TiCl₄. *J. Mater. Chem.* **2002**, (12), 1387-1390.
136. Nolph, C. A.; Sievers, D. E.; Kaewgun, S.; Kucera, C. J.; McKinney, D. H.; Rientjes, J. P.; White, J. L.; Bhave, R.; Lee, B. I., Photocatalytic study of polymorphic titania synthesized by ambient condition sol process. *Catal. Lett.* **2007**, *117* (3-4), 102-106.

References

137. Bhave, R. C.; Lee, B. I., Experimental variables in the synthesis of brookite phase TiO₂ nanoparticles. *Materials Science and Engineering a-Structural Materials Properties Microstructure and Processing* **2007**, *467* (1-2), 146-149.
138. Junin, C.; Thanachayanont, C.; Euvananont, C.; Inpor, K.; Limthongkul, P., Effects of precipitation, sol-gel-synthesis conditions, and drying methods on the properties of nano-TiO₂ for photocatalysis applications. *Eur. J. Inorg. Chem.* **2008**, (6), 974-979.
139. Addamo, M.; Bellardita, M.; Carriazo, D.; Di Paola, A.; Milioto, S.; Palmisano, L.; Rives, V., Inorganic gels as precursors of TiO₂ photocatalysts prepared by low temperature microwave or thermal treatment. *Applied Catalysis B-Environmental* **2008**, *84* (3-4), 742-748.
140. Zheng, W.; Liu, X.; Yan, Z.; Zhu, L., Ionic Liquid-Assisted Synthesis of Large-Scale TiO₂ Nanoparticles with Controllable Phase by Hydrolysis of TiCl₄. *ACS Nano* **2009**, *3* (1), 115-122.
141. Cheng, H. M.; Ma, J. M.; Zhao, Z. G.; Qi, L. M., Hydrothermal Preparation of Uniform Nanosize Rutile and Anatase Particles. *Chem. Mater.* **1995**, *7* (4), 663-671.
142. Chen, Z. Q.; Li, W. K.; Zeng, W. J.; Li, M. S.; Xiang, J. H.; Zho, Z. H.; Huang, J. L., Microwave hydrothermal synthesis of nanocrystalline rutile. *Mater. Lett.* **2008**, *62* (28), 4343-4344.
143. Ogihara, T., Hydrolysis of Metal Alkoxides in Homogeneous Solutions. In *Fine Particles: Synthesis, Characterization, and Mechanisms of Growth*, Sugimoto, T., Ed. Marcel Dekker, Inc.: 2000; pp 35-57.
144. Barringer, E. A.; Bowen, H. K., High-Purity, Monodisperse TiO₂ Powders by Hydrolysis of Titanium Tetraethoxide. 1. Synthesis and Physical Properties. *Langmuir* **1985**, (1), 414-420.
145. Djaoued, Y.; Bruning, R.; Bersani, D.; Lottici, P. P.; Badilescu, S., Sol-gel nanocrystalline brookite-rich titania films. *Mater. Lett.* **2004**, *58* (21), 2618-2622.
146. Kominami, H.; Kato, J.; Murakami, S.; Ishii, Y.; Kohno, M.; Yabutani, K.; Yamamoto, T.; Kera, Y.; Inoue, M.; Inui, T.; Ohtani, B., Solvothermal syntheses of semiconductor photocatalysts of ultra-high activities. *Catal. Today* **2003**, *84* (3-4), 181-189.
147. Li, Y.; White, T. J.; Lim, S. H., Low-temperature synthesis and microstructural control of titania nano-particles. *J. Solid State Chem.* **2004**, *177* (4-5), 1372-1381.
148. Watson, S.; Beydoun, D.; Scott, J.; Amal, R., Preparation of nanosized crystalline TiO₂ particles at low temperature for photocatalysis. *J. Nanopart. Res.* **2004**, *6* (2-3), 193-207.
149. Deshpande, S. B.; Potdar, H. S.; Kholam, Y. B.; Patil, K. R.; Pasricha, R.; Jacob, N. E., Room temperature synthesis of mesoporous aggregates of anatase TiO₂ nanoparticles. *Mater. Chem. Phys.* **2006**, (97), 207-212.

References

150. Wang, G., Hydrothermal synthesis and photocatalytic activity of nanocrystalline TiO₂ powders in ethanol-water mixed solutions. *Journal of Molecular Catalysis a-Chemical* **2007**, *274* (1-2), 185-191.
151. Han, S.; Choi, S.-H.; Kim, S.-S.; Cho, M.; Jang, B.; Kim, D.-Y.; Yoon, J.; Hyeon, T., Low-Temperature Synthesis of Highly Crystalline TiO₂ Nanocrystals and their Application to Photocatalysis. *Small* **2005**, *1* (8-9), 812-816.
152. Mohammadi, M. R.; Cordero-Cabrera, M. C.; Ghorbani, M.; Fray, D. J., Synthesis of high surface area nanocrystalline anatase-TiO₂ powders derived from particulate sol-gel route by tailoring processing parameters. *J. Sol-Gel Sci. Technol.* **2006**, *40* (1), 15-23.
153. Sayilkan, F.; Erdemoglu, S.; Asiltürk, M.; Akarsu, M.; Sener, S.; Sayilkan, H.; Erdemoglu, M.; Arpac, E., Photocatalytic performance of pure anatase nanocrystallite TiO₂ synthesized under low temperature hydrothermal conditions. *Mater. Res. Bull.* **2006**, (41), 2276–2285.
154. Hidalgo, M. C.; Aguilar, M.; Maicu, M.; Navío, J. A.; Colón, G., Hydrothermal preparation of highly photoactive TiO₂ nanoparticles. *Catal. Today* **2007**, (129), 50–58.
155. Mahshid, S.; Askari, M.; Ghamsari, M. S., Synthesis of TiO₂ nanoparticles by hydrolysis and peptization of titanium isopropoxide solution. *J. Mater. Process. Technol.* **2007**, (189), 296-300.
156. Reyes-Coronado, D.; Rodriguez-Gattorno, G.; Espinosa-Pesqueira, M. E.; Cab, C.; de Coss, R.; Oskam, G., Phase-pure TiO₂ nanoparticles: anatase, brookite and rutile. *Nanotechnology* **2008**, *19* (14), 1-10.
157. Periyat, P.; McCormack, D. E.; Hinder, S. J.; Pillai, S. C., One-Pot Synthesis of Anionic (Nitrogen) and Cationic (Sulfur) Codoped High-Temperature Stable, Visible Light Active, Anatase Photocatalysts. *Journal of Physical Chemistry C* **2009**, *113* (8), 3246-3253.
158. Ahonen, P. P.; Kauppinen, E. I.; Joubert, J. C.; Deschanvres, J. L.; Van Tendeloo, G., Preparation of nanocrystalline titania powder via aerosol pyrolysis of titanium tetrabutoxide. *J. Mater. Res.* **1999**, *14* (10), 3938-3948.
159. Tandon, P.; Balakrishnan, J., Predicting heat and mass transfer to a growing, rotating preform during soot deposition in the outside vapor deposition process. *Chem. Eng. Sci.* **2005**, *60* (18), 5118-5128.
160. Wang, X. S.; Nie, Q. H.; Xu, T. F.; Liu, L. R. In *A review of the fabrication of optic fiber - art. no. 60341D*, Changchun, PEOPLES R CHINA, Aug 21-26; Breckinridge, J. W. Y. T., Ed. Changchun, PEOPLES R CHINA, 2005; pp D341-D341.
161. Chen, C. C.; Bai, H. L.; Chein, H. M.; Chen, T. M., Continuous generation of TiO₂ nanoparticles by an atmospheric pressure plasma-enhanced process. *Aerosol Sci. Technol.* **2007**, *41* (11), 1018-1028.

References

162. Yang, G. X.; Zhuang, H. R.; Biswas, P., Characterization and sinterability of nanophase titania particles processed in flame reactors. *Nanostruct. Mater.* **1996**, 7 (6), 675-689.
163. Yang, G.; Biswas, P., Study of the Sintering of Nanosized Titania Agglomerates in Flames Using In Situ Light Scattering Measurements. *Aerosol Sci. Technol.* **1997**, (27), 507-521.
164. Yang, G. X.; Biswas, P., Study of the sintering of nanosized titania agglomerates in flames using in situ light scattering measurements. *Aerosol Sci. Technol.* **1997**, 27 (4), 507-521.
165. Almquist, C. B.; Biswas, P., Role of Synthesis Method and Particle Size of Nanostructured TiO₂ on Its Photoactivity. *J. Catal.* **2002**, (212), 145-156.
166. Biswas, P.; Cho, K.; Lee, M.; Hogan, C., Synthesis of nanostructured pristine and doped titanium dioxide for oxidizing contaminants in air. *Abstracts of Papers of the American Chemical Society* **2005**, 229, U925-U925.
167. Thimsen, E.; Biswas, P., Nanostructured thin films produced in flame aerosol reactors for photosplitting of water. *Solar Hydrogen and Nanotechnology* **2006**, 6340, U95-U100 301.
168. Biswas, P.; Jiang, J.; Chen, D.-R., Synthesis of nanoparticles in a flame aerosol reactor with independent and strict control of their size, crystal phase and morphology. *Nanotechnology* **2007**, (18), 8.
169. Thimsen, E.; Biswas, P., Nanostructured Photoactive Films Synthesized by a Flame Aerosol Reactor. *AIChE J.* **2007**, 53 (7), 1727-1735.
170. Jiang, J.; Chen, D. R.; Biswas, P., Synthesis of nanoparticles in a flame aerosol reactor with independent and strict control of their size, crystal phase and morphology. *Nanotechnology* **2007**, 18 (28), 1-8.
171. Thimsen, E.; Rastgar, N.; Biswas, P., Rapid synthesis of nanostructured metal-oxide films for solar energy applications by a flame aerosol reactor (FLAR) - art. no. 66500G. *Solar Hydrogen and Nanotechnology II* **2007**, 6650, G6500-G6500 210.
172. Tiwari, V.; Jiang, J.; Sethi, V.; Biswas, P., One-step synthesis of noble metal-titanium dioxide nanocomposites in a flame aerosol reactor. *Applied Catalysis a-General* **2008**, 345 (2), 241-246.
173. Jiang, J.; Oberdorster, G.; Elder, A.; Gelein, R.; Mercer, P.; Biswas, P., Does nanoparticle activity depend upon size and crystal phase? *Nanotoxicology* **2008**, 2 (1), 33-42.
174. Thimsen, E.; Biswas, S.; Lo, C. S.; Biswas, P., Predicting the Band Structure of Mixed Transition Metal Oxides: Theory and Experiment. *Journal of Physical Chemistry C* **2009**, 113 (5), 2014-2021.

References

175. Dhumal, S. Y.; Daulton, T. L.; Jiang, J.; Khomami, B.; Biswas, P., Synthesis of visible light-active nanostructured TiO_x ($x < 2$) photocatalysts in a flame aerosol reactor. *Applied Catalysis B-Environmental* **2009**, *86* (3-4), 145-151.
176. Seders, L. A.; Biswas, P.; Fein, J. B., Experimental study of the factors that influence titanium dioxide nanoparticle adhesion to mineral surfaces. *Geochim. Cosmochim. Acta* **2009**, *73* (13), A1189-A1189.
177. Chen, D. R.; Li, W. L.; Cheng, M. D., Development of a multiple-stage differential mobility analyzer (MDMA). *Aerosol Sci. Technol.* **2007**, *41* (2), 217-230.
178. Harano, A.; Shimada, K.; Okubo, T.; Sadakata, M., Crystal phases of TiO₂ ultrafine particles prepared by laser ablation of solid rods. *J. Nanopart. Res.* **2002**, (4), 215–219.
179. Arrii, S.; Morfin, F.; Renouprez, A. J.; Rousset, J. L., Oxidation of CO on gold supported catalysts prepared by laser vaporization: Direct evidence of support contribution. *JACS* **2004**, *126* (4), 1199-1205.
180. Gyorgy, E.; Sauthier, G.; Figueras, A.; Giannoudakos, A.; Kompitsas, M.; Mihailescu, I. N., Growth of Au-TiO₂ nanocomposite thin films by a dual-laser, dual-target system. *J. Appl. Phys.* **2006**, *100* (11), -.
181. Kim, J.-H.; Lee, S.; Im, H.-S., The effect of different ambient gases, pressures, and substrate temperatures on TiO₂ thin films grown on Si(100) by laser ablation technique. *Appl. Phys. A* **1999**, (69 [Suppl.]), S629–S632.
182. Li, S.; El-Shall, M. S., Synthesis of nanoparticles by reactive laser vaporization: silicon nanocrystals in polymers and properties of gallium and tungsten oxides. *Appl. Surf. Sci.* **1998**, 330-338.
183. Moore, J. H.; Davis, C. C.; Coplan, M. A., *Building Scientific Apparatus*. Third Edition ed.; Perseus Books: Cambridge, MA, 2003; p 654.
184. Hollas, J. M., *Modern Spectroscopy*. 4th ed.; John Wiley & Sons, Ltd.: Chichester, West Sussex, England, 2004.
185. Matsubara, M.; Yamaki, T.; Itoh, H.; Abe, H.; Asai, K., Preparation of TiO₂ Nanoparticles by Pulsed Laser Ablation: Ambient Pressure Dependence of Crystallization. *Jpn. J. Appl. Phys.* **2003**, *42*, L 479–L 481.
186. Kawasaki, K.; Despres, J. F.; Kamei, S.; Ishikawa, M.; Odawara, O., Fabrication of nanometer-sized anatase particles by a pulsed laser ablation method. *J. Mater. Chem.* **1997**, *7* (10), 2117-2120.
187. Berger, L. I., Properties of the Semiconductors. In *CRC Handbook of Chemistry and Physics 88th Edition (Internet Version 2008)*, Lide, D. R., Ed. CRC Press/Taylor and Francis: Boca Raton, FL, 2008; pp 12-77 - 12-89.

References

188. Becker, M.; Fan, H. V., Optical Properties of Semiconductors, III. Infra-Red Transmission of Silicon. *Physical Review* **1949**, *76*, 1531-1532.
189. Harrick, N. J., Use of Infrared Absorption to Determine Carrier Distribution in Germanium and Surface Recombination Velocity. *Physical Review* **1956**, *101*, 491-492.
190. Thompson, T. L.; Yates, J. T., Surface science studies of the photoactivation of TiO₂-new photochemical processes. *Chem. Rev.* **2006**, *106* (10), 4428-4453.
191. Bechinger, C.; Wirth, E.; Leiderer, P., Photochromic coloration of WO₃ with visible light. *Appl. Phys. Lett.* **1996**, *68* (20), 2834-2836.
192. Ozkan, E.; Tepehan, F. Z., Optical and structural characteristics of sol-gel-deposited tungsten oxide and vanadium-doped tungsten oxide films. *Sol. Energy Mater. Sol. Cells* **2001**, *68* (3-4), 265-277.
193. Goudsmit, S. A., 50 Years of Spin - It Might as Well Be Spin. *Physics Today* **1976**, *29* (6), 40-43.
194. Simpson, R. E., *Introductory Electronics for Scientists and Engineers*. 2nd. ed.; Allyn and Bacon, Inc.: Boston, 1987.
195. Tissue, B. M., Synthesis and Luminescence of Lanthanide Ions in Nanoscale Insulating Hosts. *Chem. Mater.* **1998**, (10), 2837-2845.
196. Tissue, B. M.; Yuan, H. B., Structure, particle size, and annealing of gas phase-condensed Eu³⁺:Y₂O₃ nanophosphors. *J. Solid State Chem.* **2003**, (171), 12-18.
197. Gordon, W. O. Metal Oxide Nanoparticles: Optical Properties and Interaction with Chemical Warfare Agent Simulants. Virginia Polytechnic Institute and State University, Blacksburg, 2006.
198. Gordon, W. O.; Carter, J. A.; Tissue, B. M., Long-lifetime luminescence of lanthanide-doped gadolinium oxide nanoparticles for immunoassays. *J. Lumin.* **2004**, *108*, 339-342.
199. Gordon, W. O.; Tissue, B. M.; Morris, J. R., Adsorption and decomposition of dimethyl methylphosphonate on Y₂O₃ nanoparticles. *Journal of Physical Chemistry C* **2007**, *111* (8), 3233-3240.
200. Hell, S. W., Far-field optical nanoscopy. *Science* **2007**, *316* (5828), 1153-1158.
201. Flegler, S. L.; John W. Heckman, J.; Klomparens, K. L., *Scanning and Transmission Electron Microscopy: An Introduction*. W. H. Freeman and Company: New York, 1993.
202. Heimendahl, M. v., *Electron Microscopy of Materials: An Introduction*. Academic Press: New York, 1980.

References

203. Davisson, C.; Germer, L. H., Diffraction of Electrons by a Crystal of Nickel. *The Physical Review* **1927**, *30* (6), 705-740.
204. Davisson, C. J.; Germer, L. H., The Scattering of Electrons by a Single Crystal of Nickel. *Nature* **1927**, *119* (2998), 558-560.
205. Shindo, D.; Hiraga, K., *High-Resolution Electron Microscopy for Materials Science*. Springer - Verlag: Tokyo, 1998.
206. Suryanarayana, C.; Norton, M. G., *X-Ray Diffraction: A Practical Approach*. Plenum Press: New York, 1998.
207. Rasband, W. S. *ImageJ*, U. S. National Institutes of Health: Bethesda, Maryland, 1997-2008.
208. Guinier, A., *X-Ray Diffraction In Crystals, Imperfect Crystals, and Amorphous Bodies*. Dover Publications, Inc.: New York, 1994.
209. Warren, B. E., *X-Ray Diffraction*. Dover Publications, Inc.: New York, 1990.
210. Sonneveld, E. J.; Visser, J. W., Automatic Collection of Powder Data from Photographs. *J. Appl. Crystallogr.* **1975**, (8), 1-7.
211. Zhou, J. K.; Takeuchi, M.; Ray, A. K.; Anpo, M.; Zhao, X. S., Enhancement of photocatalytic activity of P25TiO(2) by vanadium-ion implantation under visible light irradiation. *J. Colloid Interface Sci.* **2007**, *311* (2), 497-501.
212. Nyhoff, L.; Leestma, S., *FORTRAN 77 for Engineers and Scientists*. Third ed.; Macmillan Publishing Co.: New York, 1992; p 630.
213. Stewart, J., *Calculus: Early Transcendentals*. 5 ed.; Brooks / Cole: 2003.
214. Brown, A. M., A step-by-step guide to non-linear regression analysis of experimental data using a Microsoft Excel spreadsheet. *Computer Methods and Programs in Biomedicine* **2001**, (65), 191-200.
215. Brown, A. M., A non-linear regression analysis program for describing electrophysiological data with multiple functions using Microsoft Excel. *Computer Methods and Programs in Biomedicine* **2006**, (82), 51-57.
216. Chestnoy, N.; Harris, T. D.; Hull, R.; Brus, L. E., Luminescence and Photophysics of Cds Semiconductor Clusters - the Nature of the Emitting Electronic State. *J. Phys. Chem.* **1986**, *90* (15), 3393-3399.
217. Frindell, K. L.; Tang, J.; Harreld, J. H.; Stucky, G. D., Enhanced Mesostructural Order and Changes to Optical and Electrochemical Properties Induced by the Addition of Cerium(III) to Mesoporous Titania Thin Films. *Chem. Mater.* **2004**, (16), 3524-3532.

References

218. Szczepankiewicz, S. H.; Moss, J. A.; Hoffmann, M. R., Slow Surface Charge Trapping Kinetics on Irradiated TiO₂. *J. Phys. Chem. B* **2002**, *106*, 2922-2927.
219. Di Valentin, C.; Pacchioni, G.; Selloni, A., Electronic structure of defect states in hydroxylated and reduced rutile TiO₂(110) surfaces. *Phys. Rev. Lett.* **2006**, *97* (16), 1-4.
220. Warren, D. S.; McQuillan, A. J., Influence of adsorbed water on phonon and UV-induced IR absorptions of TiO₂ photocatalytic particle films. *J. Phys. Chem. B* **2004**, *108* (50), 19373-19379.
221. Peter, L. M.; Walker, A. B.; Boschloo, G.; Hagfeldt, A., Interpretation of apparent activation energies for electron transport in dye-sensitized nanocrystalline solar cells. *J. Phys. Chem. B* **2006**, *110* (28), 13694-13699.
222. Tsukernik, A.; Slutzky, M.; Palevski, A.; Luryi, S.; Shtrikman, H., A method for Fermi energy measurements. *Appl Phys Lett* **1998**, *73* (1), 79-81.
223. Hayes, W.; Stoneham, A. M., *Defects and Defect Processes in Nonmetallic Solids*. John Wiley & Sons: New York, 1985.
224. Jie, H.; Park, H.; Chae, K. H.; Anpo, M.; Park, J. K., Suppressed recombination of electrons and holes and its role on the improvement of photoreactivity of flame-synthesized TiO₂ nanopowders. *Chem. Phys. Lett.* **2009**, *470* (4-6), 269-274.
225. *Surface and Nanomolecular Catalysts*. CRC Press: Boca Raton, 2006.
226. Gellings, P. J.; Bouwmeester, H. J. M., Solid state aspects of oxidation catalysis. *Catal. Today* **2000**, *58*, 1-53.
227. Vedrine, J. C.; Coudurier, G.; Millet, J. M. M., Molecular design of active sites in partial oxidation reactions on metallic oxides. *Catal. Today* **1997**, *33* (1-3), 3-13.
228. Doornkamp, C.; Ponc, V., The universal character of the Mars and Van Krevelen mechanism. *Journal of Molecular Catalysis a-Chemical* **2000**, *162* (1-2), 19-32.
229. Wachs, I. E.; Jehng, J. M.; Ueda, W., Determination of the chemical nature of active surface sites present on bulk mixed metal oxide catalysts. *J. Phys. Chem. B* **2005**, *109* (6), 2275-2284.
230. Blakemore, J. S., *Semiconductor Statistics*. Dover Publications, Inc.: Mineola, New York, 1987.